Short-reach Optical Communication Using Directly Modulated Lasers

Feng Yuan

Submitted in total fulfilment of the requirements of the degree of

Master of Philosophy

Department of Electrical and Electronic Engineering

THE UNIVERSITY OF MELBOURNE

Abstract

During the past decade, with the rapid development of cloud computing, smart phones and mobile Internet, there has been an increasing demand for high-capacity and high-reliable metropolitan area networks and access networks. Unlike long-haul transmission systems, where bulky and expensive optical components are normally used, the short-to-medium reach optical link which is in the range of a few kilometres to hundreds of kilometres is naturally cost-sensitive. Therefore, in recent years, instead of using the traditional $LiNbO_3$-based intensity and I/Q modulators, the compact and low-cost directly modulated laser (DML) has drawn plenty of attention and becomes an attractive candidate in such short-reach applications. DML-based optical transmission systems have been extensively explored and successfully demonstrated with various configurations, including using different modulation, detection and multiplexing methods. Among these demonstrations, DML has already shown its capability to realize optical access links for a data rate of 100 Gbps and beyond. Despite its promising performance that has been reported, not only the potential of DML has not been fully exploited, but also its limitations as an optical transmitter has not been thoroughly discussed.

It is well-known that one of the major drawbacks of ordinary DML being used as a transmitter is its intrinsic frequency chirp, which, after combining with the fibre chromatic dispersion, becomes an increasingly detrimental factor to data rate enhancement. Efforts have been made to overcome such obstacles, such as employing inverse dispersion fibre, optical injection locking, optical filters and specially designed DMLs. The effectiveness of the above approaches on extending the transmission reach and increasing the data rate has been rather limited. Additionally, they always require extra devices, adding more complexity and cost to the system, and are thus not desirable for low-cost implementations.

In this work, utilizing the digital signal processing (DSP) facilitated coherent detection (COHD), we propose a new modulation scheme on DML-based systems, which is called complex-modulated DML (or CM-DML). It has been shown that a significant optical signal-to-noise ratio (OSNR) sensitivity improvement can be achieved compared with the traditional intensity-only detection method. Besides, we also experimentally demonstrated that the CM-DML system exhibits a reasonable tolerance for reduced receiver bandwidth. In a nutshell, it is feasible to realize CM-DML systems using cost-effective receivers with narrow bandwidth.

Declaration

This is to certify that

1. the thesis comprises only my original work towards the MPhil,
2. due acknowledgement has been made in the text to all other material used,
3. the thesis is less than 40,000 words in length, exclusive of tables, maps, bibliographies and appendices.

Signature:

Date:

Acknowledgements

This thesis is conducted with the kind instruction, help and support from many people, without whom this thesis would not have been possible. I would like to express my sincere appreciations to them whether explicitly mentioned here or not.

Firstly, I would like to express my deepest gratitude of the consistent help and support from my supervisor Professor William Shieh, for his guidance and support throughout my MPhil study. I would not have been able to complete this thesis without his technical advice and generous support. It is my great pleasure to have the opportunity to study under his supervision. I would also like to thank my co-supervisor Associate Professor Ying Tan for the high quality technical supervisions and the encouragement throughout my MPhil candidature. I also would like to acknowledge my co-authors Di Che and Qian Hu who have given me great help in the research work conducted in this thesis. It was such a wonderful time to study and work in such a supporting group.

I feel grateful to the University of Melbourne that has provided me with MIFRS and MIRS scholarships to support my living and study. Many thanks go to my colleagues around me for providing a friendly and entertaining working atmosphere.

Finally, I appreciate my parents for their constant support and encouragement. It is their love that helps me overcome the obstacles encountered in life and work, and leads to the accomplishment of my MPhil study.

To my parents

Table of Contents

List of Figures

List of Tables

Chapter 1
Introduction

1.1. SHORT-REACH OPTICAL COMMUNICATION: AN INTRODUCTION

1.1.1. Overview of Optical Fibre Communication Networks

Information technology has been growing exponentially by taking advantage of modern telecommunication systems, providing us with many revolutionary applications such as the broadband Internet access, mobile Internet services through smart phones, cloud computing and storage, etc. In particular, during the past four decades, the continuously advancing optical communication technology has played a vital role in the development of high-speed and high-quality telecommunication systems. Today, optical communication represents a broad and rapidly-evolving industry, offering numerous high-quality services to sustain the ever-growing demand on delivery of more and more data with high bandwidth and fidelity. However, underneath these applications, increasingly sophisticated technologies with commercial viability have been explored and deployed in field, from the network layer to the physical layer. The fundamental limitations on the growth of the overall transmission data rate, quality and reach lie in the physical layer, which mainly consists of various optical and electrical devices, different modulation techniques, and associated digital signal processing (DSP) algorithms. The scope of the work in this thesis is constrained in developing novel technologies on such a physical layer.

Compared with electrical transmission systems employing copper cables, optical fibre communication systems possess a variety of advantages, such as low transmission loss, high capacity, immunity to electrical interference and high signal security. Based on modern fabrication technologies of single-mode fibres, the fibre attenuation coefficients are commonly below 0.2 dB/km across a bandwidth of tens of nanometres (i.e. several THz). In contrast, typical coaxial cables have tens of dB/km of losses across a bandwidth of only hundreds of MHz [1]. Moreover, with the advent of commercial viable erbium-doped fibre amplifiers (EDFAs) in the 1980s, signal amplification can be directly achieved in the optical domain, keeping the signal distortions at a relatively low level. Therefore, optical signals are able to be transmitted over thousands of kilometres with a potential data rate of many Tb/s on a single piece of fibre. In addition, optical fibres are made from silicon dioxide which is an electrical insulator so that they do not generate cross talks with nearby electromagnetic waves. As a

consequence, optical fibres are not affected by any electrical interference from radio waves, high current lightning and power cables. Furthermore, the transmitted signal inside a fibre does not radiate, which makes it difficult to tap the signal from a fibre. Thus, optical fibre communication systems can provide a much securer signal delivery than electrical transmission systems.

Due to the above benefits, since their introduction in the 1970s, optical fibres have been massively deployed in the core network of the telecommunication system [2]. After four decades of development, nowadays, optical fibre transmission systems not only have been deployed in the backbone of core networks, but also are more and more widely being deployed in access networks. As shown in Figure 1.1, with an increasing number of end-users connecting into the telecommunication networks, the backbone of core networks requires ultra-high speed transmission which has increased from 10 Gb/s to 1 Tb/s. In order to meet such a capacity need, there are already plenty of advanced solutions explored in both academia and industry, such as various multiplexing techniques, namely, polarization-division multiplexing (PDM), wavelength-division multiplexing (WDM), and space-division multiplexing (SDM). Since the overall performance is as important as the system cost in the core networks, the above off-the-shelf techniques are currently sufficient to meet today's transmission capacity and quality requirements. Therefore, in order to sustain the exponentially growing population of end-users, the bottleneck of the whole network lies in the access layer, where both performance and cost are critical.

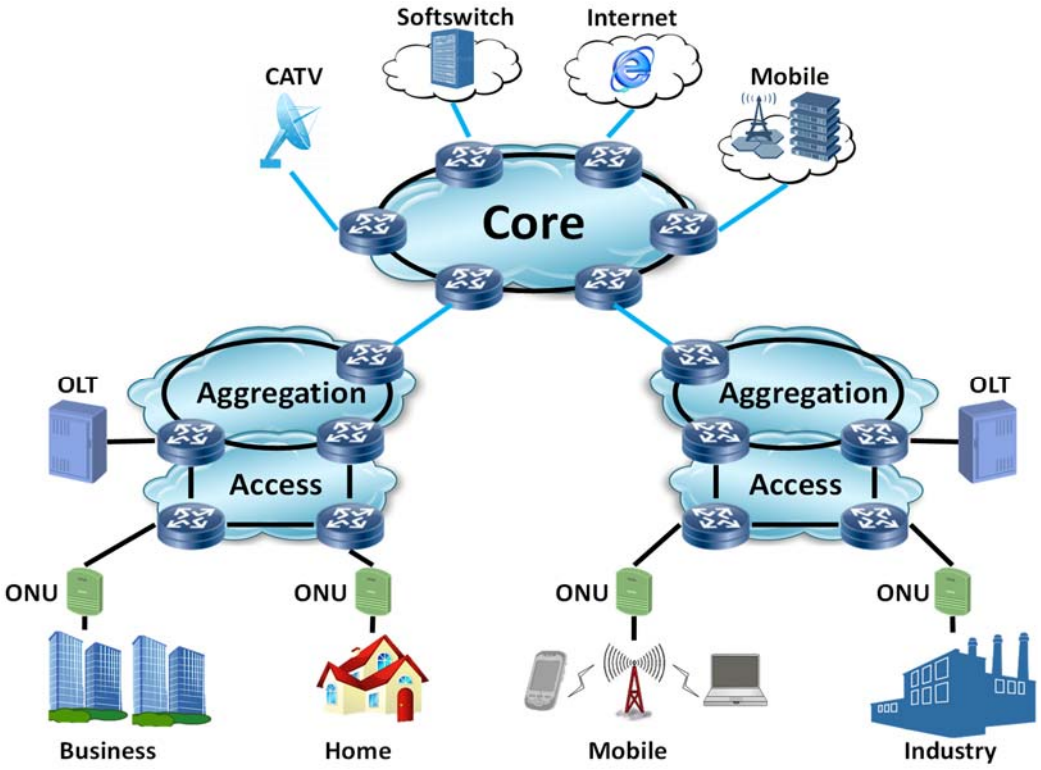

Figure 1.1. Structure of optical communication networks. CATV: Community antenna television; OLT: optical line terminals; ONU: optical network unit.

1.1.2. Introduction to Optical Access Networks

According to the transmission distance, the optical access networks can be further divided into metropolitan area networks (MAN) and the so-called "last-mile" links, which are both within the scope of discussion in this thesis. In MAN, the transmission distance is normally from tens of kilometres to a few hundreds of kilometres depending on sizes of the cities; while for the last-mile links, the reach ranges from hundreds of meters for data-centre interconnects to tens of kilometres for industry and business applications. For the implementation of optical access networks, the commercially available solutions include the active optical networks (AON) and the passive optical networks (PON). In AON, it often requires active components such as optical-electrical-optical (OEO) converters, active switches. As a result, it is generally impossible to keep both a low number of interfaces and a low level of power consumption. However, the PON does not have these problems, as it is totally based on passive components such as optical power splitters, passive (de)multiplexers. Therefore, since the first introduction of PON in the 1990s, a number of PON architectures have been investigated, standardized and commercialized. After nearly two decades of development, the PON technology has evolved from the low-speed (i.e. less than 1 Gb/s) primitives such as ATM PON (APON) and broadband PON (BPON) to the state-of-the-art next-generation PON2 (NG-PON2) which is capable to support 40 Gb/s throughput to the entire network. As IEEE has begun to discuss the standardization of 400-Gigabit Ethernet (400-GbE), higher data-rate PON technology, such as 100-Gb/s PON, will not be far away. As such, the ever-growing capacity and quality demands offer both opportunities and challenges in the field of optical access networks.

1.1.3. Transmission Links in the Optical Access Networks

As the fundamental element in the optical access networks, a particular transmission link is vital to the quality of service in the whole network. Generally speaking, an optical transmission link consists of the optical transmitter, the fibre channel and the optical receiver. An optical transmitter can be constructed either by an external modulator attached to a laser source or a directly modulated laser (DML). The fibre used here is normally standard single-mode fibre (SSMF). For the receiver, either the direct detection (DD) scheme using a single photodetector or the coherent detection approach can be applied. As the simplest solution, intensity modulation with direct detection (or IM-DD) is an attractive candidate and has been extensively explored. In addition, there are various modulation formats that can be used for modulating meaningful data onto the light pulses and transmitting them over the fibre link. It is critical to choose an appropriate modulation format when implementing a transmission link, because the capacity and transmission reach are both dependent on the employed modulation format. Each of the aforementioned subsystems has critical impact on the overall performance of the optical link and will be further investigated in chapter 2. In order to have an intuitive understanding on the influence of different subsystems, in Table 1.1, we summarize some of the short-to-medium reach transmission experiments in recent years.

Table 1.1. A brief summary of recent short-to-medium reach transmission experiments. SiP: Silicon photonics; EML: externally modulated laser; DML: directly modulated laser; VCSEL: vertical cavity surface emitting laser; OOK: on-off keying; PAM: pulse amplitude modulation; CAP: carrierless amplitude and phase modulation; DMT: discrete multitone; DD: direct detection; COHD: coherent detection.

Bit rate per wavelength	Transmitter	Modulation format	Detection Method	Distance	Waveband	Ref
112 Gb/s	SiP Intensity Modulator	PAM-8	DD	10 km	1310 nm	[3]
112 Gb/s	EML	CAP-16	DD	10 km	1310 nm	[4]
10 Gb/s	DML	CAP-128	DD	40 km	1310 nm	[5]
112 Gb/s	DML	DMT	DD	30 km	1310 nm	[6]
100 Gb/s	VCSEL	DMT	DD	4 km	1550 nm	[7]
25 Gb/s	VCSEL	OOK	DD	4.2 km	1550 nm	[8]
56 Gb/s	VCSEL	PAM-4	DD	2 km	1550 nm	[9]
100 Gb/s	VCSEL	PAM-4	DD	100 m	1550 nm	[10]
88 Gb/s	VCSEL	PAM-3	COHD	960 km	1550 nm	[11]
100 Gb/s	VCSEL	PAM-4	COHD	400 km	1550 nm	[12]

As shown in Table 1.1, despite the fact that 100-Gb/s link has already been achieved using simple direct detection, the transmission distance is largely limited by the signal distortions originated from the fibre chromatic dispersion (CD) at 1550 nm. Furthermore, the intrinsic frequency chirp of the DML gives rise to a broadening optical spectrum, which makes the high-speed signal suffer even severer impairments from CD. Therefore, either the wavelength of 1310 nm or digital coherent detection is employed to extend the reach. The phenomenon of CD and its compensation techniques will be discussed in details in chapter 2.

1.2. MOTIVATION OF THIS THESIS

As discussed in the above section, for optical access links, it is desirable to achieve a balance among system performance, transmission reach and total system cost. The standard solution to achieve the optimal system performance is employing the traditional $LiNbO_3$-based external modulators with digital coherent detection. The commercially available zero-chirp optical intensity modulators can already achieve a bandwidth of more than 65 GHz and 35-GHz optical I/Q modulators are off the shelf. Besides, these types of modulators normally need high-performance light sources. Therefore, on one hand, in order to avoid these bulky and expensive external modulators, the low-cost DML has become a preferred transmitter, which integrates the laser source and the capability of optical modulation in one device. On the other hand, current commercial DMLs are much less powerful than $LiNbO_3$-based external modulators in terms of bandwidth and chirp performance. The highest bandwidth available for off-the-shelf DMLs is only 18 GHz. Besides, as when a DML is modulated, the drive currents directly change the properties of its active region, it is inevitable to have intrinsic frequency chirp which cannot be controlled or even suppressed in an easy and cost-effective manner based on state-of-the-art

technologies. For the receiver, still with the aim to minimize the system cost, the direct detection scheme using a single square-law photodetector has been widely accepted. Such a detection approach can only recover the intensity of the received optical signal, indicating that receiver-end performance enhancement techniques, such as digital CD compensation, cannot be easily applied without inserting extra devices. Moreover, on a single photodetector, PDM technique is also difficult to be employed to double the link capacity. It is not surprising to observe that the single-photodetector receiver hits a performance ceiling under such a minimum-cost transceiver solution, as shown in Table 1.1. As a consequence, some compromises have been made to obtain a better performance. For instance, digital coherent detection was employed [11,12] and in order to cope with CD, approaches using extra devices have been applied, such as using inverse-dispersion fibre [13], optical injection locking [14], and optical filter [15].

From the above discussion, it is obvious that potential research work lies between the high-performance solution which employs $LiNbO_3$ external optical modulators with full-blown digital coherent detection and the simplest solution which utilizes low-cost DML-based IM-DD. Therefore, in this thesis, we focus our work on the exploration of appropriate transmission schemes in the short-to-medium reach optical link. In particular, we concentrate on novel modulation schemes. The motivation comes from the fact that in either commercial DML products or the aforementioned works [14,15], huge efforts have been made to reduce the DML frequency chirp instead of taking advantage of it. In addition, despite the application of digital coherent detection, the work in [11,12] only focuses on the intensity modulation (IM) of the DML, where the frequency chirp has been considered as a source of signal distortion and thus a limitation on system performance. By utilizing both the intensity and phase modulation with optical coherent detection, a new modulation scheme can be developed using DML, offering a novel solution to the short-to-medium reach optical link.

1.3. THESIS OUTLINE

The main objective of this thesis is to investigate a novel DML-based modulation scheme, known as complex-modulated DML (or CM-DML). Its theoretical feasibility is analysed, followed by experimental demonstrations. Through investigating the basic working principles of a typical DML, the theoretical foundation of CM-DML is first revealed. Then, corresponding DSP algorithms in the CM-DML system are investigated, including the proof-of-concept demonstration of their effectiveness and the implementation details. Furthermore, we carry out numerical simulations of a typical CM-DML transmission system which shows its potential to support high-order PAM format achieving a data rate of 100 Gb/s and even beyond. Finally, we provide experimental demonstrations of various CM-DML systems, from the prototype transmitting 40-Gb/s polarization-division multiplexed PAM-4 signal to the final version of a 100-Gb/s link over 1600-km SSMF.

Chapter 2 provides a literature review of different subsystems in a short-reach optical communication system. After introducing several commonly used optical transmitters and advanced modulation formats, the principle of coherent reception is presented in details. The

transmission impairments inside the SSMF are then investigated. In the last part of this chapter, typical DSP algorithms for a standard dual-polarization digital coherent receiver are discussed in details, including CD compensation, polarization demultiplexing and carrier recovery.

Chapter 3 provides a thorough analysis on the principles of a typical DML. After the derivation of the classical laser rate equation, we introduce the origin of laser frequency chirp, which leads to an analytical equation to describe such a phenomenon. The laser noises are then modelled using the Langevin force approach, which includes both the relative intensity noise and the laser phase noise. A simulation model is then built to investigate the behaviours of the DML showing its steady-state characteristics and its dynamics when being modulated. Finally, we introduce the effect of thermal frequency modulation (FM) inside the DML. Experimental characterization of the thermal FM in a 10-GHz DML is then carried out and we report the observation of a 7.5-ns time constant. The impact of such a fast time constant on the DML-based transmission systems is then theoretically analysed.

In chapter 4, the CM-DML modulation scheme is presented with both theoretical analysis and experimental demonstrations. We first explain the concepts of the CM-DML scheme, followed by a thorough analysis of the symbol decision procedure, where we propose two different dynamic programming (DP) algorithms. One of them is based on the chirp parameter estimation while the other relies on the transition probability estimation. Transmission simulations are then carried out demonstrating the signal-to-noise ratio (SNR) sensitivity advantage of the CM-DML approach over the IM-DD scheme. The capability of the CM-DML system to support high-order PAM formats is further investigated with an analysis on the optimization of laser chirp parameters. Furthermore, transmission experiments are demonstrated showing the potential of the CM-DML system to offer a data rate as high as 100 Gb/s within the distance range of 1600 km. Finally, the receiver filtering effect of the CM-DML system is discussed, indicating the feasibility of its implementation by employing cost-effective receiver subsystems without excessive increase of receiver bandwidth.

Chapter 5 provides a summary of the main findings and conclusions of the thesis, and a discussion of possible future research topics.

1.4. PUBLICATIONS

1.4.1. Journal Papers

[1] **F. Yuan**, D. Che, and W. Shieh, "Receiver bandwidth effects on complex modulation and detection using directly modulated lasers," *Optics Letters,* vol. 41, no. 9, pp. 2041-2044, 2016.

[2] D. Che, **F. Yuan**, and W. Shieh, "Towards high-order modulation using complex modulation of semiconductor lasers," *Optics Express*, vol. 24, no. 6, pp. 6644-6649, 2016.

[3] D. Che, **F. Yuan**, H. Khodakarami, and W. Shieh, "Duobinary pulse shaping for frequency chirp enabled complex modulation," *Optics Letters*, vol. 41, no. 17, pp. 3968-3971, 2016.

[4] D. Che, **F. Yuan**, Q. Hu, and W. Shieh, "Frequency chirp supported complex modulation of directly modulated lasers," *Journal of Lightwave Technology*, vol. 34, no. 8, pp. 1831-1836, 2016.

[5] D. Che, Q. Hu, **F. Yuan**, Q. Yang, and W. Shieh, "Enabling complex modulation of directly modulated signals using laser frequency chirp," *IEEE Photonics Technology Letters*, vol. 27, no. 22, pp. 2407-2410, 2015.

[6] D. Che, **F. Yuan**, and W. Shieh, "High-fidelity angle-modulated analog optical link," *Optics Express*, vol. 24, no. 15, pp. 16320-16328, 2016.

[7] Q. Hu, D. Che, Y. Wang, **F. Yuan**, Q. Yang, and W. Shieh, "Complex modulation and detection with directly modulated lasers," *Optics Express*, vol. 23, no. 25, pp. 32809-32819, 2015.

1.4.2. Conference Papers

[1] **F. Yuan**, D. Che, Q. Hu, and W. Shieh, "Characterization of thermal frequency modulation of a DFB laser using digital coherent detection," in *Proceedings Optical Fiber Communication Conference* (Anaheim, California, United States, 2016), p. W2A.25.

[2] D. Che, **F. Yuan**, and W. Shieh, "Towards high-order PAM utilizing large frequency chirp of directly modulated lasers," in *Proceedings Optical Fiber Communication Conference* (Anaheim, California, United States, 2016), p. W1A.4.

[3] D. Che, **F. Yuan**, Q. Hu, and W. Shieh, "Complex modulation of directly modulated lasers for medium reach optical communications," in *Proceedings Optical Fiber Communication Conference* (Anaheim, California, United States, 2016), p. Tu2A.5.

[4] D. Che, Q. Hu, **F. Yuan**, and W. Shieh, "Enabling complex modulation using the frequency chirp of directly modulated lasers," in *Proceedings European Conference on Optical Communication* (Valencia, Spain, 2015), pp. 1-3.

Chapter 2
Theory and Literature Review

2.1. INTRODUCTION

In optical communication networks, the short-to-medium reach transmission systems have a wide range of applications from data-centre interconnects to MAN with the transmission distance varying from a few hundred metres to more than a thousand kilometres. Therefore, in order to cope with such diverse demands, various solutions have been proposed during the past two decades. Each of these system-level solutions contains a number of subsystems. This chapter will focus on investigating the concepts and principles of these subsystems. We start from the optical transmitter setup, including the directly and externally modulated lasers that are widely used for short-to-medium reach applications and the external optical modulators for medium reach and long-haul transmission. We then explain the generation of advanced modulation formats that are commonly applied in short-to-medium reach transmission, such as the pulse amplitude modulation (PAM), the discrete multitone modulation (DMT) and carrierless amplitude and phase modulation (CAP). Besides, we also analyse pulse shaping filters to reduce the required radio frequency (RF) bandwidth. Then, we look inside the receiver setup and the details of commonly used detection approaches are described, including the intensity-only detection using a single photodetector and the standard dual-polarization optical coherent receiver. In the following section, the channel impairments caused by single-mode fibre are discussed including both linear and nonlinear fibre impairments. The linear impairments mainly consist of fibre attenuation, CD, polarization mode dispersion (PMD), phase noise and amplified spontaneous emission (ASE) noise. The major nonlinear impairments include self-phase modulation (SPM) and cross-phase modulation (XPM). Classical DSP algorithms for standard dual-polarization optical coherent receiver are then reviewed, which include receiver front-end correction, digital CD compensation methods, adaptive digital filters for polarization demultiplexing, and finally, the carrier phase estimation and local oscillator (LO) frequency offset compensation.

2.2. TRANSMITTERS IN OPTICAL FIBRE COMMUNICATION SYSTEMS

2.2.1. Directly Modulated Lasers

For short-to-medium reach optical links, the whole transmission system is naturally cost-sensitive, which is due to the demand on a great number of transmitter-receiver pairs in applications such as data-centre interconnections and passive optical networks. Needless to say, high system performance, normally in terms of bit error rate (BER), is also an indispensable requirement that is directly related to the quality of service. Therefore, taking all the considerations into account, the main challenge for designing a feasible solution to short-to-medium reach optical links is to find a balance among cost, complexity and performance. For this reason, at the transmitter side, low-cost light sources, such as DMLs [16,17], and cheap externally modulated lasers (EMLs) [3,18] have been extensively investigated in the past decade. Moreover, as a special type of DML, the vertical-cavity surface-emitting laser (VCSEL) has drawn plenty of attention recently due to its capability of achieving high data rate and its convenience of array integration [7-15,19-21]. As for an EML, it is more complicated in structure than a DML, where an electro-absorption modulator (EAM) is attached to a distributed feedback (DFB) laser. Despite the increased cost of the EML compared with that of the DML, the EML generally has the advantage of a higher output power, a smaller frequency chirp and a higher extinction ratio under modulation. Therefore, the EML is assumed by the 10G-EPON standard [22].

2.2.1.1. Introduction to DMLs and VCSELs

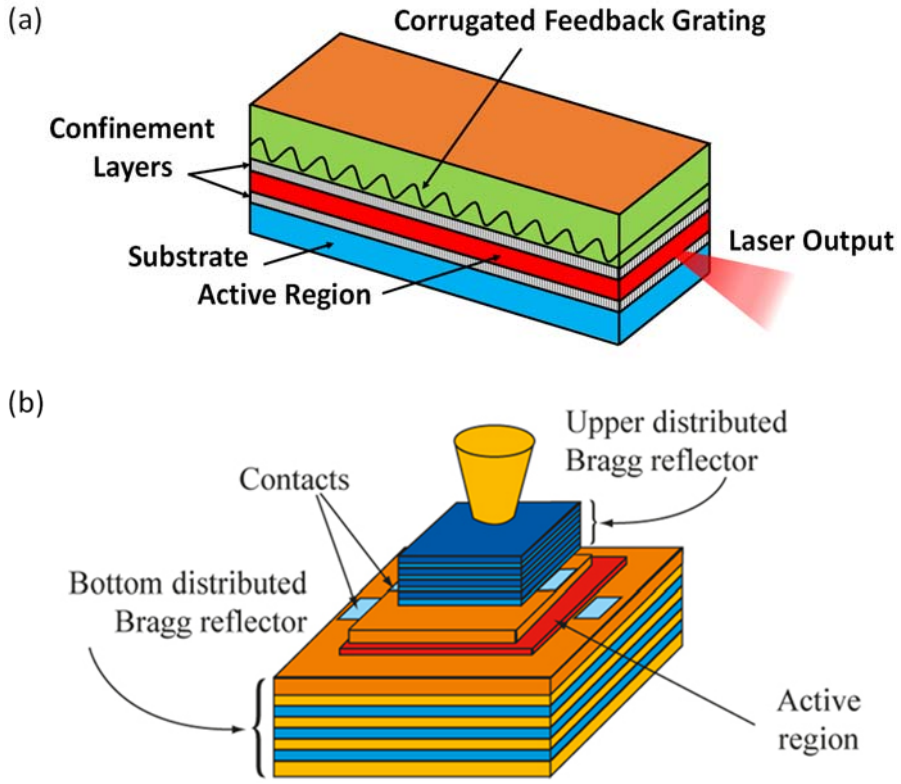

Figure 2.1. Structures of directly modulated lasers. (a) Typical DFB laser diode; (b) VCSEL.

As shown in Figure 2.1 (a), commercial DMLs generally use the distributed feedback structure with a diffraction grating, namely the Bragg grating, in the waveguide in order to obtain stable operation under direct modulation, and is thus called a "DFB" laser. The modulation bandwidth and transmission distance strongly rely on both the dimensions of the laser structure and the gain materials used, which are related to the frequency chirp parameters and the linewidth of the laser. A low frequency chirp and a narrow linewidth are required for achieving high data rate and long distance. Nowadays, commercially viable DFB-type DMLs can reach a 3-dB bandwidth of 16 GHz with the linewidth controlled within 5 MHz. The driving current is usually constrained within 100 mA. The maximum operating power can be achieved as high as 14 dBm. The baseband signal generated by an RF driver is loaded on the optical beam by modulating the injection current which is then directly applied to the laser diode chip leading to a modulated optical signal. After a standard packaging, such as the butterfly package, a DML appears as a single chip and only requires a simple electrical circuit configuration for operation, so it may fit to a compact design. For example, the DML we used in this thesis has the dimension of $26.04\times8.89\times9.11\text{mm}$ with the butterfly package.

Figure 2.1 (b) shows the structure of a typical VCSEL which is a semiconductor laser diode emitting a highly efficient laser beam vertically from its top surface. The basic light emitting principle of VCSEL is similar to ordinary semiconductor lasers. The advantage of VCSEL over edge emitting lasers mainly lies in its low fabrication cost. Because VCSELs emit optical beam perpendicular to the laser surface, tens of thousands of VCSELs can be processed on a single wafer with the mature semiconductor manufacturing technology. VCSELs are also easy to be tested while still in wafer form, which greatly increases manufacturing yield and lowers per unit cost. Besides, VCSELs can be easily integrated by being fabricated into one- or two-dimensional array, which enables only one single die to comprise tens or even hundreds of individual laser diodes to increase the total maximum output power and long-term reliability. The flexibility of adjusting the output optical power makes VCSELs suitable for a wide range of applications with various emitting power requirements. For optical transmission applications, the electro-optical characteristics of VCSELs make them capable to modulate at a data rate up to and beyond 25 Gb/s for on-off keying (OOK) format. Employing advanced modulation formats, the data rate can reach 100 Gb/s and beyond [7,11-12]. VCSELs have already been demonstrated to offer reliable high-speed optical transmissions at distances ranging from very close proximity links, i.e. a few centimetres, up to 500 m in data centre, enterprise, and campus networks [9].

2.2.1.2. Introduction to EMLs

An EML is a laser diode integrated with an EAM in a single chip. In the laser diode section, normally the same device structure as the DML is employed, such as a DFB type laser diode (see Figure 2.1 (a)). The laser diode section operates under a continuous wave (CW) mode, while the baseband RF signals are loaded onto the EAM section to generate modulated optical signals. Therefore, in contrast to a DML, the properties of the laser diode section in an EML

are immune to the process of modulation, remaining almost unchanged with and without modulation. With such characteristics, EMLs are advantageous in applications with higher data rates and longer distance transmission compared with a DML. This advantage of an EML is mainly due to its much smaller laser frequency chirp and larger extinction ratio. Nowadays, commercially viable EMLs can reach a 3-dB bandwidth of 50 GHz. The driving current is usually constrained within 100 mA. However, due to the increased insertion loss compared with DMLs, for commercial products, the EML output power is limited within 10 dBm. Unlike DMLs which have both transient and adiabatic chirps, EMLs only possess transient chirp. Additionally, an EML has a more stable wavelength under high-speed modulation, because the injection current (i.e. input RF signal) to the laser section is not modulated and therefore does not change. Thus, an EML has less frequency chirp effect. Under the same modulation format and baud rate, the reduced frequency chirp makes a narrower spectrum of the modulated optical signal which is then less vulnerable to CD. Extinction in an EML is caused by absorption as the coefficient changes with the modulated voltage applied to the EAM section, and the extinction ratio becomes higher with a large voltage input such as the on/off electrical signal. The increased output power and extinction ratio make the system more resilient to noise, leading to a higher link power budget and is thus suitable for longer reach. The frequency response of an EML depends only on the parasite inductance and capacitance in the EAM section, and is not affected by the relaxation frequency in the laser diode section as in a DML. Such properties enable an EML to have high modulation bandwidth, even greater than 40 GHz. Besides, an EML can also be packaged in a compact manner, leading to a similar size as a typical DML. Therefore, EMLs are generally used in applications with high power budget demands, such as passive optical networks [22].

2.2.2. External Optical Modulators

In medium reach and long-haul transmission systems, the $LiNbO_3$-based optical intensity and I/Q modulators have been widely applied during the past few decades. In this section, we introduce the theoretical background of these external modulators.

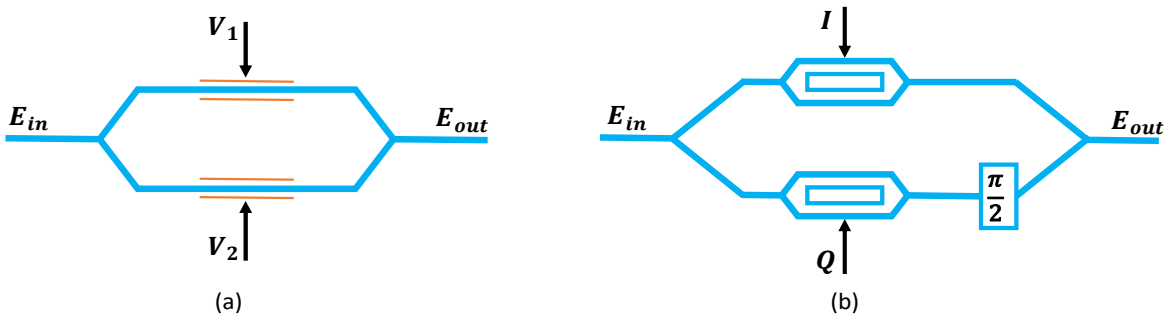

Figure 2.2. Structure of typical external modulators. (a) Dual-drive Mach-Zehnder modulator; (b) I/Q modulator.

The Mach-Zehnder modulator (MZM) has been extensively explored and demonstrated since the 1980s as an attractive high performance electro-optic modulator for high data-rate optical transmission [23-26]. Base on the linear electro-optic effect (i.e. the Pockel effect), there are various types of intensity modulators reported in the literature. The Pockel effect states that when an external electrical field is applied to a piece of optical waveguide, a change in the refractive index occurs, which is proportional to the applied electrical field. As a result, a phase change is observed for the incident optical field polarized in the direction of this external electrical field. The way in which the phase change converts into intensity modulation is determined by the device geometrical design and one of these designs is the Mach-Zehnder interferometer (MZI). Figure 2.2 (a) shows the structure of a primitive MZI-based modulator, known as the dual-drive MZM (or DDMZM). The physics of DDMZM operation has been extensively investigated in the literature [23,24] and will only be briefly reviewed here. We assume the input optical signal before modulation is expressed by [27]

$$E_{in}(t) = A_c \cos(\omega_c t + \varphi_c) \tag{2-1}$$

where A_c represents the amplitude of the signal, ω_c is the angular frequency, and φ_c is the initial phase. The input optical signal E_{in} is first divided equally into two halves at the input Y branch which acts as a 3-dB coupler. The separated signals then travel along the two arms of the DDMZM, which normally have the same physical length. Voltage is applied to each arm, leading to a phase shift in each of the optical signals. At the output of the Y branch, the optical fields recombine. If the guided modes are in-phase, after constructive interference, they excite the lowest order mode in the output waveguide. In contrast, if they are exactly 180° out of phase, their recombination excites the first order antisymmetric mode, which is the cut-off mode in the output waveguide and is rapidly attenuated. Thus, the transfer function can be written as [27]

$$\begin{aligned} E_{out}(t) &= \frac{1}{2}\left(E_{in}(t)e^{j\pi V_1(t)/V_\pi}\right) + \frac{1}{2}\left(E_{in}(t)e^{j\pi V_2(t)/V_\pi}\right) \\ &= E_{in}(t)\cos\left(\frac{\pi}{2}\cdot\frac{V_1(t)-V_2(t)}{V_\pi}\right)e^{j\pi\frac{V_1(t)+V_2(t)}{2V_\pi}} \end{aligned} \tag{2-2}$$

where $V_1(t)$ and $V_2(t)$ are the two drive RF signals, and V_π is a reference voltage depending on the geometrical and material parameters of the MZM. Eq. (2-2) indicates that the DDMZM can modulate both the amplitude and the phase of the input optical field. If we set $V_1(t) = V_2(t)$, then the DDMZM behaves as a phase modulator, while if we set $V_1(t) = -V_2(t)$, the DDMZM operates as an intensity modulator, whose transfer function is simplified as

$$E_{out}(t) = E_{in}(t)\cos\left(\frac{\pi V_1(t)}{V_\pi}\right) \tag{2-3}$$

The MZM is very sensitive to the polarization state of the input optical field, because the phase shift in each of the modulator arms is induced only in the optical field polarized in the same direction as the exciting electrical field. Due to such reasons, a polarization stabilized light

source is normally essential as the input optical signal and a polarization maintaining fibre (PMF) should also be employed between the source and the modulator.

Figure 2.2 (b) shows the structure of the optical I/Q modulator consisting of two DDMZMs operating in IM mode, and a $\pi/2$ phase shift between the two arms. After equally split by the input Y branch, the optical signal E_{in} travels along the two arms. In each arm, the amplitude of the optical field is modulated by the MZM. Before the two arms combine, a $\pi/2$ phase shift is added onto one of the arms making the signals orthogonal to each other. Using Eq. (2-1) and Eq. (2-3), the transfer function of the I/Q modulator is derived as

$$E_{out}(t) = \frac{A_c}{2}\cos\left(\frac{\pi I(t)}{V_\pi}\right)\cos(\omega_c t + \varphi_c) - \frac{A_c}{2}\cos\left(\frac{\pi Q(t)}{V_\pi}\right)\sin(\omega_c t + \varphi_c) \quad (2\text{-}4)$$

where $I(t)$ and $Q(t)$ are the drive electrical signals to the two MZMs. The optical I/Q modulator enables independent amplitude and phase modulation of the input optical field, which has the most modulation flexibility. In contrast, according to Eq. (2-2), using a DDMZM, the modulated amplitude and phase is restricted by a nonlinear relationship, which indicates that nonlinear digital filters may be needed for certain applications, such as CD compensation. In addition, as pointed out in [28], compared with DDMZM, the optical I/Q modulator introduces fewer errors due to the limited resolution of DSP.

Nowadays, commercially viable intensity MZM modulators can achieve a 3-dB bandwidth of 100 GHz much higher than those in DMLs and EMLs. Even for more complex I/Q modulators, the 3-dB bandwidth of the off-the-shelf products can reach over 30 GHz. The driving voltage is usually several volts. Despite the dominance of the MZM and I/Q modulator in high performance optical transmission systems, these external modulators are normally expensive, complex, bulky and with high optical insertion losses. For instance, a typical I/Q modulator can have an insertion loss as high as 13 dB with a package size of $90.5 \times 13.2 \times 7\text{mm}$. Therefore, the traditional $LiNbO_3$-based external modulator is not a strong candidate for the cost-sensitive applications in short-to-medium reach optical communication systems. However, in the past few years, with rapid advances in silicon photonics (SiP) technology, the cost-effective SiP-based external modulators have somehow become a potential candidate for short-reach links. Data rates as high as 100 Gb/s and beyond have been reported [3,18]. For instance, in [3], a 112-Gb/s PAM-8 signal is transmitted over 10-km SSMF with an SiP intensity modulator. With the cost and complexity reduced by the SiP technology which provides even a better performance, the external optical modulator may still be a competitive candidate in short-to-medium reach applications in the near future.

2.2.3. Advanced Modulation Formats

In this section we will introduce the concepts of several advanced modulation formats that have been extensively investigated for short-reach optical links in recent years. To begin with, we first briefly explain some of the basic modulation formats. With respect to the available modulation dimensions, two fundamental degrees of freedom are the amplitude and phase of

the optical signal. The phase modulation can be implemented by a simple electro-optic modulator manipulating the phase of the optical signal through Pockel effect. The amplitude modulation is realized by the MZM external modulator or DML. Combining both amplitude and phase modulation, the optical I/Q modulator can change the I/Q components of the optical signal independently, which leads to arbitrary constellation formations on the complex plane. Therefore, simply modulating the phase dimension results in the M-ary phase-shift keying (or M-PSK) format, while only modulating the amplitude dimension gives M-ary pulse amplitude modulation (M-PAM) format. Combining both the amplitude and phase modulation, we can further develop the M-ary quadrature amplitude modulation (or M-QAM) format. In the field of optical communication, all modulation formats that go beyond OOK format have earned the name *advanced*. Beyond these two basic dimensions, in optical domain, the polarization of the optical field, the wavelength of the light source, and the mode in multimode fibre can all be exploited as a degree of freedom, leading to PDM, WDM and SDM, respectively. In [29], a thorough review is given on the current direct detection based advanced modulation formats for short-reach optical interconnects. However, most of the above formats normally require the bulky and expensive $LiNbO_3$-based external modulators. In this thesis, we focus on the applications of the DML in single wavelength channel inside single-mode fibre, and we thus only concern the optical amplitude modulation with PDM.

2.2.3.1. The PAM modulation format

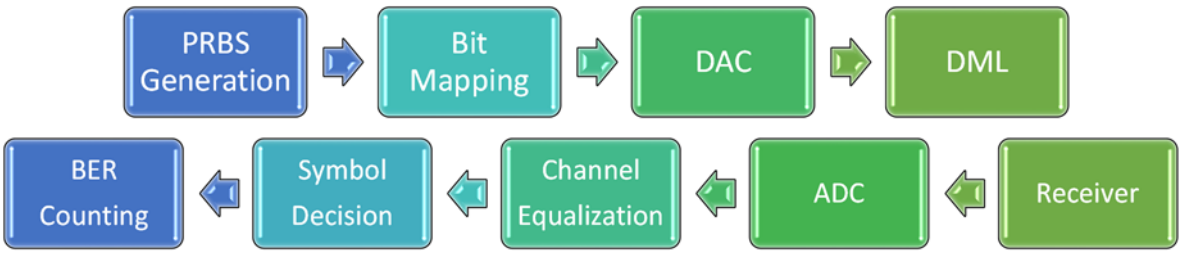

Figure 2.3. DSP flow chart of the PAM modulation format. PRBS: Pseudorandom binary sequence; DAC: digital-to-analog converter; ADC: analog-to-digital converter; BER: bit error rate.

As show in Figure 2.3, the PAM format is straightforward to implement on a DML through directly modulating the levels of the injection current into the laser diode. If needed, forward error correction (FEC) codes and pulse shaping filters can also be added into the transmitter DSP. At the receiver side, the training symbol aided least mean square (LMS) algorithm is often employed as the equalizer. Despite its simplicity, the PAM format has obvious shortcomings. When the data rate exceeds 40 Gb/s, for the PAM-4 format, the transmission distance is largely limited [9]. This can be understood by considering the relatively low spectral efficiency of the PAM-4 format and thus, a large bandwidth is required to achieve high data rates, which induces a largely increased CD-induced impairment to the signal. To overcome this, one of the proposed approaches recently is the duo-binary format, a variant of PAM, which is able to reduce the spectrum occupied by the modulated signal. Thus, it alleviates the CD-induced signal distortions and extends the transmission distance. In [30], a 28-Gbps duo-binary signal is

transmitted over 40-km SSMF with a 10-GHz DML as the transmitter and 7-GHz PIN photodiode as the receiver. 40-Gb/s TDM-PON is demonstrated with 20-GHz avalanche photodiode (APD) as the receiver in the downstream transmission over 42-km SSMF. However, when the capacity demand reaches 100 Gb/s and beyond, even with the duo-binary format, the bandwidth consumption is substantial, where high bandwidth electronics are thus essential. In addition, the reach is also largely limited due to CD. For example, in [10], a 100-Gb/s PDM PAM-4 signal is transmitted over only 100-m SSMF and in [31], a 103-Gb/s link with transmitted OOK signal detected as duo-binary signal over 1-km SSMF is reported, which requires 40G-class electronics.

2.2.3.2. The CAP modulation format

To obtain longer reach with a relatively high data rate, more advanced modulation formats with high spectral efficiencies are proposed. Despite the fact that only the optical amplitude (or intensity) modulation can be applied to DMLs, the phase dimension can still be utilized in RF domain. By introducing transmitter DSP and employing the phase modulation of the RF signal, formats like CAP and DMT are thus designed.

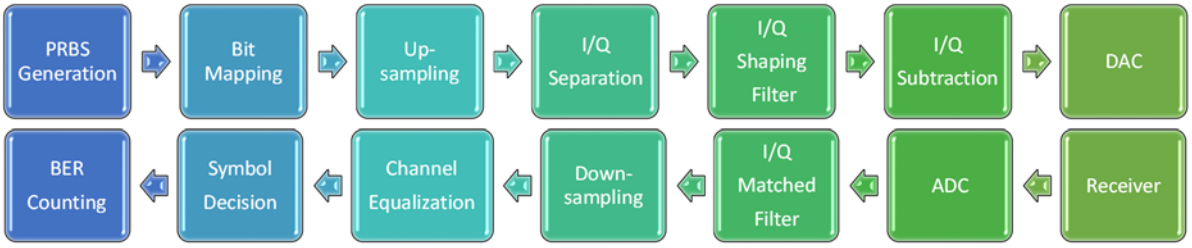

Figure 2.4. DSP flow chart of the CAP modulation format. PRBS: Pseudorandom binary sequence; DAC: digital-to-analog converter; ADC: analog-to-digital converter; BER: bit error rate.

Figure 2.4 gives the main DSP procedures of the CAP format. In essence, CAP is a special type of the QAM format. After pseudorandom binary sequence (PRBS) generation, the bit stream is first mapped into QAM constellation and the in-phase and quadrature components are separated. The two signals are then shaped by two filters with impulse responses of $f_1 = g(t)\cos(2\pi f_c t)$ and $f_2 = g(t)\sin(2\pi f_c t)$, which form a Hilbert pair. $g(t)$ represents a square-root-raised-cosine shaping filter with a roll-off coefficient of α and f_c is the central frequency given by $(1+\alpha)\cdot B/2$, where B is the baud rate. At the receiver, the signal is first passed through two matched filters given by $f_1(-t)$ and $f_2(-t)$, recovering the in-phase and quadrature components. The equalizer is often implemented by cascaded multi-modulus algorithm (CMMA), which is suitable for multi-level CAP signals. During the past decades, there have been plenty of demonstrations on CAP-based short-reach optical links, including both low and high-order CAP format. In [4], a 112-Gb/s transmission system over 10-km SSMF is reported using single band CAP-16 with the EML and in [5], a 10-Gb/s high-order CAP (i.e. CAP-128/256) signal over 40-km SSMF on a low-cost 10-GHz DML is demonstrated using the decision-directed least mean square (DD-LMS) algorithm as the adaptive equalizer. As shown

above, by introducing some transmitter DSP, the CAP format can improve the spectral efficiency compared with PAM. However, the highest spectral efficiency is achieved by the DMT format, a variant of the orthogonal frequency-division multiplexing (OFDM) format [32].

2.2.3.3. The discrete multitone modulation format

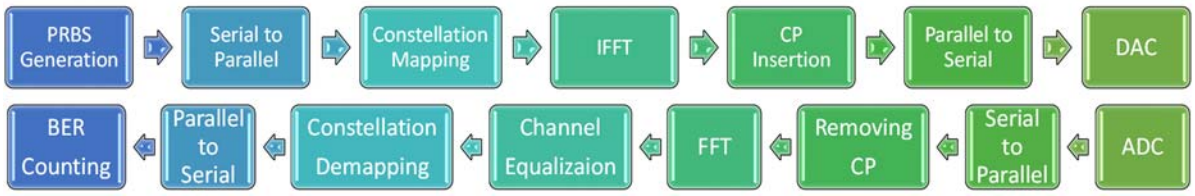

Figure 2.5. DSP flow chart of the DMT modulation format. PRBS: Pseudorandom binary sequence; DAC: digital-to-analog converter; ADC: analog-to-digital converter; BER: bit error rate; CP: cyclic prefix; FFT: fast Fourier transform; IFFT: inverse fast Fourier transform.

As a special type of OFDM, Figure 2.5 illustrates the basic transmitter DSP procedures of the DMT format. The PRBS bit stream is firstly transformed into frames by serial-to-parallel conversion and is then modulated onto each subcarrier with a basic modulation format, e.g., M-QAM or M-PSK. After adding pilot tones for time synchronization and channel estimation, the signal is then mapped into time domain using inverse fast Fourier transform (IFFT). Cyclic prefix (CP) is added to each DMT symbol to cope with the dispersion-induced inter-symbol interference (ISI) and inter-channel interference (ICI). After the signal is converted back into the serial form, it is finally sent to the digital-to-analog converter (DAC) for transmission. Due to the Hermitian symmetry property of the generated signal, it is a real-valued signal in time domain, which can be directly modulated onto a DML or an EML. At the receiver, the DSP procedure is similar to the reverse version of the transmitter DSP, except for the channel equalization process which is performed by a 1-tap equalizer for each subcarrier. In addition, the modulation formats of subcarriers can be different from each other, which is optimized adaptively according to the frequency response of the channel. The Levin-Campello algorithm (LCA) is one of the commonly used optimization algorithms [33]. Thus, the DMT format can fully exploit the whole bandwidth of a transmission link. In [33], after channel flattening through a Fabry-Perot filter, a 28 Gb/s DMT single is transmitted over up to 75-km SSMF and a 112-Gb/s transmission over 30-km SSMF is achieved employing DMT on a DML [6].

To conclude, the modulation formats employed in the short-to-medium reach optical communication systems have evolved from the simplest OOK to multi-level advanced formats such as CAP and DMT, which enables the link capacity to reach 100 Gb/s and beyond for a single wavelength. When choosing a proper format for a practical link, not only the total capacity requirement should be met, but the transceiver complexity, cost and power consumption should also be seriously considered. In this thesis, we mainly focus on the PAM format which is the most practical one, since the current commercially available transceivers for short-reach links normally employs this format.

2.2.4. Pulse Shaping Filters

In communication theory, pulse-shaping filters are normally used for shaping the waveforms of the transmitted signal pulses before sending them into the channel, which aims to limit the bandwidth occupied by the transmitted signal. Therefore, the pulse shaping technique not only reduces the required bandwidth of the channel but also provides a better control over ISI that is generated by channel impairments. The pulse-shaping filters are specially designed in a certain way so that the filter itself does not introduce ISI. Therefore, in communication theory, there are some general criteria for pulse-shaping filter design, namely, the Nyquist ISI criterion and the orthogonal pulse criterion [34]. The Nyquist-shaping pulses are appropriate for sampling receivers and the orthogonal pulses are usually used to perform pulse shaping in transmitters and also operate as matched filters in receivers. Besides, there are various other pulse-shaping approaches beyond the aforementioned Nyquist shaping and orthogonal shaping. Here, we investigate several commonly used pulse-shaping filters in transmitters.

2.2.4.1. The Gaussian filter

The impulse response of a Gaussian pulse-shaping filter is expressed by

$$h_g(t) = \frac{1}{\sigma\sqrt{2\pi}} e^{-\frac{t^2}{2\sigma^2}} \tag{2-5}$$

where σ is the standard deviation which determines the exact pulse shape. Strictly speaking, the Gaussian pulse is neither a Nyquist-shaping pulse nor an orthogonal-shaping pulse. However, by adjusting the standard deviation, it can be designed to resemble either the Nyquist or orthogonal pulses. Thus, it is widely used in optical transmission systems.

2.2.4.2. The raised-cosine filter

The frequency-domain response of a raised-cosine filter is written by

$$H_{rc}(f) = \begin{cases} T & |f| \le \frac{1-\alpha}{2T} \\ T \cdot \cos^2\left(\frac{\pi T}{2\alpha} \cdot \left(|f| - \frac{1-\alpha}{2T}\right)\right) & \frac{1-\alpha}{2T} < |f| \le \frac{1+\alpha}{2T} \\ 0 & |f| > \frac{1+\alpha}{2T} \end{cases} \tag{2-6}$$

where T is the symbol period and $\alpha \in (0,1)$ is the roll-off factor. The raised-cosine filter obeys the Nyquist ISI criterion with a bandwidth of $(1+\alpha)/T$. It is worth mentioning that the time-domain impulse response of the raised-cosine filter is expressed by the sinc function which has an infinite tail in time domain.

2.2.4.3. The root raised-cosine filter

Based on the orthogonal criterion, the root raised-cosine filter is a practical pulse-shaping filter widely applied in various communication systems as both transmitter and receiver filters. It is

named after the raised-cosine filter by taking the square root of its frequency response $H_{rc}(f)$ so that half of the filtering is performed at the transmitter side and the other half is completed at the receiver side.

The time-domain impulse response of such a filter is expressed as

$$h_{rrc}(t)=\begin{cases}\dfrac{1}{\sqrt{T}}\left(1-\alpha+4\dfrac{\alpha}{\pi}\right) & t=0\\ \dfrac{\alpha}{\sqrt{2T}}\left[\left(1+\dfrac{2}{\pi}\right)\sin\left(\dfrac{\pi}{4\alpha}\right)+\left(1-\dfrac{2}{\pi}\right)\cos\left(\dfrac{\pi}{4\alpha}\right)\right] & t=\pm\dfrac{T}{4\alpha}\\ \dfrac{1}{\sqrt{T}}\dfrac{\sin\left[\pi(1-\alpha)\cdot t/T\right]+4\alpha\cos\left[\pi(1+\alpha)\cdot t/T\right]\cdot t/T}{\pi\cdot t/T\cdot\left[1-(4\alpha\cdot t/T)^2\right]} & otherwise\end{cases} \quad (2\text{-}7)$$

where T is the symbol period and $\alpha \in (0,1)$ is the roll-off factor.

2.3. RECEIVERS IN OPTICAL FIBRE COMMUNICATION SYSTEMS

2.3.1. Direct Detection with a Single Photodetector

The core device to perform the optoelectronic conversion is a photodetector which is based on the internal photoelectric effect. There are two main types of photodetectors commercially available for optical transmission systems. The PIN photodiode is a variant of a normal p-n junction, where an intrinsic region is sandwiched between the heavily doped p region and n region. The output current of the PIN photodiode is generally weak. Thus, a transimpedance amplifier (TIA) is normally attached to the PIN photodiode, which amplifies the output current and then converts it into usable voltage. The other type is an APD with a very high sensitivity due to the internal gain section based on avalanche multiplication. The APD is usually used in situations where the received optical power is low, such as -20 dBm and even lower.

The response of a photodetector can be derived from its physical mechanism, which can be simply expressed as [35]

$$I(t)=R\left[\mathrm{Re}\left\{A(t)e^{j\omega t}\right\}\right]^{ms} \quad (2\text{-}8)$$

where $I(t)$ is the output photo-current, R is the responsivity of the photodetector, $A(t)e^{j\omega t}$ is complex optical field and "ms" denotes the mean square with respect to the optical frequency. Therefore, the photodetector is normally considered as a square-law device which detects only the intensity of the input optical field.

Eq. (2-8) is an appropriate photodetector model in most cases, except for the ignorance of the intrinsic noise. The overall noise of a photodetector is contributed by a variety of sources, mainly consisting of the detector noise and the amplifier noise. The random fluctuations of the total current flow give rise to the detector shot noise. This current is a combination of dark current and photo-current. The thermal noise of the detector is originated from the shunt resistance or the channel resistance in the case of a guard ring device. The final contribution is

the amplifier noise depending on the amplifier circuits and is a function of frequency. The overall noise can thus be represented by the quadratic sum of the above noise terms. It is more convenient to quantize the noise using the so-called noise equivalent power (or NEP). The NEP is defined by the optical power incident to the detector that is needed to equal the total noise power inside the detector. In other words, NEP is the optical power leading to an SNR of 1 [36]. NEP has a unit of $\mathrm{dBm}/\sqrt{Hz}$, and the minimum detectable optical power of a photodetector is thus given by $P_{min} = NEP \times \sqrt{BW}$, where BW is the measurement bandwidth.

Despite the high sensitivity of an APD, it generally has a much larger noise than that of the PIN photodiode. Therefore, in order to achieve the best performance, for all the experiments in this thesis, we choose the PIN photodiode as the photodetector.

2.3.2. Optical Coherent Detection

The direct detection approach can only recover the intensity of the optical field, largely limiting its usage to optical intensity modulation formats. In this section, we thoroughly investigate the optical coherent detection scheme which is capable of reconstructing both the amplitude and the phase of the received optical field [35]. The received optical signal is assumed as

$$E_s(t) = A_s(t) e^{j(\omega_s t + \varphi_s)} \tag{2-9}$$

where $A_s(t)$ denotes the amplitude, and ω_s, φ_s stand for the signal frequency and phase, respectively. The LO is written as

$$E_{LO}(t) = A_{LO}(t) e^{j(\omega_{LO} t + \varphi_{LO})} \tag{2-10}$$

where $A_{LO}(t)$, ω_{LO} and φ_{LO} are the amplitude, frequency and phase of the LO. For simplicity, we also assume that the polarizations of the signal and LO are identical. There are various structures for the implementation of a coherent receiver. In the following sections, we first introduce the concept of coherent detection using the simplest coupler-based coherent receiver and then we derive the phase-diverse coherent receiver by employing the balanced photodetector (BPD) as a DC-block. Finally, the full-blown polarization and phase-diverse coherent receiver is investigated, which is the main receiver we use for the experiments in this thesis.

2.3.2.1. Coherent detection with single photodetectors

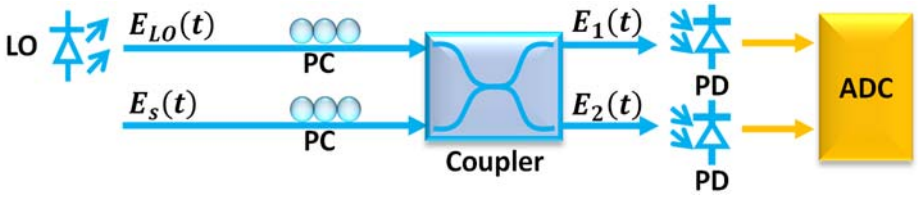

Figure 2.6. Coherent detection using single photodetectors. LO: Local oscillator; PC: polarization controller; PD: photodetector; ADC: analog-to-digital converter.

Figure 2.6 illustrates the basic concept of coherent detection through a 3-dB coupler. After polarization alignment between the LO ($E_{LO}(t)$) and the input signal ($E_s(t)$), the two optical fields mix with each other inside the 3-dB coupler. A single PD acts as the opto-electronic converter to recover the intensity of the mixed signal. The output optical fields of the coupler can be expressed by

$$\begin{bmatrix} E_1(t) \\ E_2(t) \end{bmatrix} = \frac{1}{\sqrt{2}} \begin{bmatrix} E_s(t) + E_{LO}(t) \\ E_s(t) - E_{LO}(t) \end{bmatrix} \tag{2-11}$$

Using Eq. (2-8), Eq.(2-9) and Eq. (2-10) and setting the photodetector responsivity $R = 2$, the upper branch of the final output RF signals is expressed as [35]

$$I_{RF}(t) = |E_1(t)|^2 = A_{LO}^2(t) + A_s^2(t) + 2A_{LO}(t)A_s(t)\cos(\Delta\omega t + \Delta\varphi) \tag{2-12}$$

where $\Delta\omega = |\omega_s - \omega_{LO}|$ is the frequency offset between the LO and the signal, and $\Delta\varphi = |\varphi_s - \varphi_{LO}|$ denotes the phase offset. Applying a DC-block after the PD, only the last two terms in Eq. (2-12) are left, from which we can see both the amplitude and phase of the optical signal are kept in the final output RF signal. It is also worth noting that the received signal in the beating term is amplified by the LO with a factor of $A_{LO}(t)$. Therefore, the coherent detection can largely enhance the receiver sensitivity through the LO without inserting any pre-amplification devices, such as an EDFA or a semiconductor optical amplifier (SOA). However, the above derivation ignores the noises inside the photodetector and LO which will severely contaminate the signal leading to a relatively high optical signal-to-noise ratio (OSNR) requirement for such a scheme.

2.3.2.2. Coherent detection with balanced photodetectors

BPDs are further introduced to suppress the noise and also automatically act as DC-blocks.

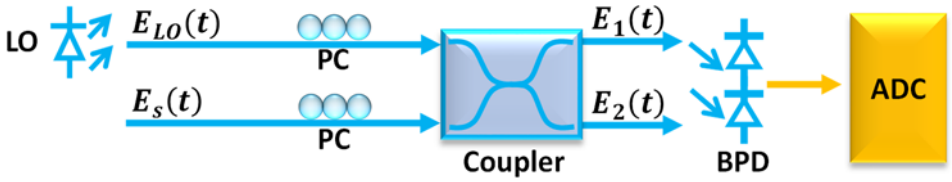

Figure 2.7. Coherent detection using balanced photodetectors. LO: Local oscillator; PC: polarization controller; BPD: balanced photodetector; ADC: analog-to-digital converter.

The BPD is two cascaded photodiodes that have almost the same parameters. Through its inner circuits, the output RF signal of a BPD is the subtraction of two outputs of the two individual photodiodes. Following the above analysis, we can thus have

$$I_{RF}(t) = |E_1(t)|^2 - |E_2(t)|^2 = 4A_{LO}(t)A_s(t)\cos(\Delta\omega t + \Delta\varphi) \tag{2-13}$$

Since the two individual photodiodes have almost the same parameters, which results in similar noise performances, the total noise at the output RF signal can be suppressed by subtraction, leading to a higher OSNR tolerance compared with the single photodiode scheme. In addition,

the receiver sensitivity is also doubled by such subtraction procedure. However, in the aforementioned two coherent detection approaches, it is still not straightforward to separate the amplitude signal and the phase signal from the final RF output. By introducing another path with a 90° phase shift, we can thus have the phase-diverse coherent receiver.

2.3.2.3. Phase-diverse coherent detection

Figure 2.8 shows the phase-diverse coherent detection scheme. Both the LO and the signal are first equally split into two paths. One path of the LO is directly mixed with the signal in a 3-dB coupler, while the other path is 90° phase-shifted before combined with the signal. After the optoelectronic conversion by BPDs, the I and Q components of the signal can thus be recovered. The whole structure is normally called the 90° optical hybrid.

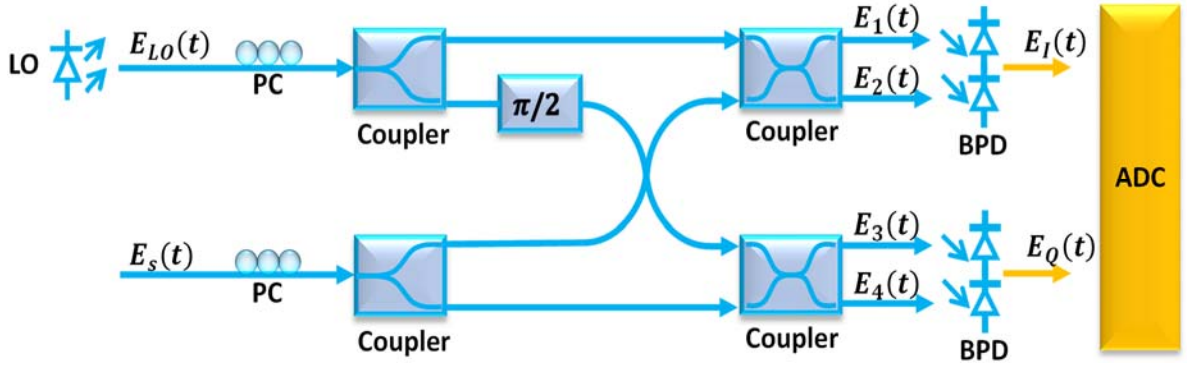

Figure 2.8. Structure of phase-diverse coherent detection. LO: Local oscillator; PC: polarization controller; BPD: balanced photodetector; ADC: analog-to-digital converter.

According to the analysis in section 2.3.2.1, the incident optical fields to the BPDs are expressed as

$$\begin{bmatrix} E_1(t) \\ E_2(t) \\ E_3(t) \\ E_4(t) \end{bmatrix} = \frac{1}{2}\begin{bmatrix} E_s(t)+E_{LO}(t) \\ E_s(t)-E_{LO}(t) \\ E_s(t)+iE_{LO}(t) \\ E_s(t)-iE_{LO}(t) \end{bmatrix} \tag{2-14}$$

After the BPDs, the recovered RF signals of the I and Q components are written by

$$\begin{aligned} \begin{bmatrix} E_I(t) \\ E_Q(t) \end{bmatrix} &= \begin{bmatrix} \left|E_s(t)+E_{LO}(t)\right|^2-\left|E_s(t)-E_{LO}(t)\right|^2 \\ \left|E_s(t)+iE_{LO}(t)\right|^2-\left|E_s(t)-iE_{LO}(t)\right|^2 \end{bmatrix} = 2\begin{bmatrix} \mathrm{Re}\left\{E_sE_{LO}^*\right\} \\ \mathrm{Im}\left\{E_sE_{LO}^*\right\} \end{bmatrix} \\ &= 2\begin{bmatrix} A_{LO}(t)A_s(t)\cos(\Delta\omega t+\Delta\varphi) \\ A_{LO}(t)A_s(t)\sin(\Delta\omega t+\Delta\varphi) \end{bmatrix} \end{aligned} \tag{2-15}$$

Therefore, the received complex RF signal is constructed by

$$I_{RF}(t) = E_I(t) + jE_Q(t) = 2A_{LO}(t)A_s(t)e^{j(\Delta\omega t+\Delta\varphi)} \tag{2-16}$$

Based on $I_{RF}(t)$, both the amplitude and phase modulation can be recovered, supporting formats like M-PSK, M-QAM, etc. However, in this scheme, accurate polarization alignment between the signal and LO is still necessary, which is normally not practical in field deployment. In the next section, we will develop the final version of coherent detection enabling polarization and phase diversity.

2.3.2.4. Polarization and phase-diverse coherent detection

Although any kind of complex modulation format can be well recovered using the above phase-diverse coherent detection, with an increasing demand on the overall data rate of transmission systems, PDM is a simple way to double the link capacity. At the receiver, in order to demultiplex the two polarizations, the dual-polarization coherent receiver is an essential component. As shown in Figure 2.9, such a receiver can be separated into three stages: polarization splitting; phase-diverse coupling and optoelectronic conversion.

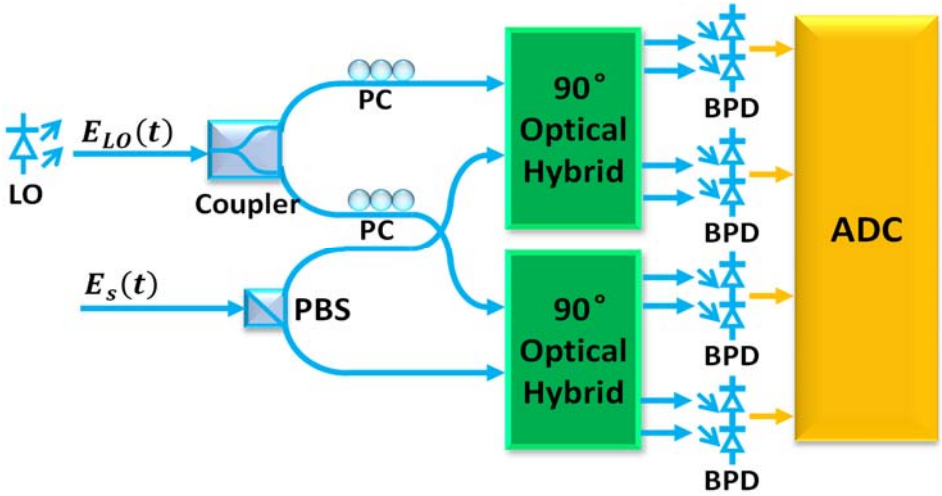

Figure 2.9. Structure of polarization and phase-diverse coherent detection. LO: Local oscillator; PBS: polarization beam splitter; PC: polarization controller; BPD: balanced photodetector; ADC: analog-to-digital converter.

In the first stage, the LO is first split into two paths both of which go through polarization controllers to align their polarizations with the two axes of the polarization beam splitter (PBS), respectively. In the meanwhile, the optical signal is split into two polarizations by the PBS. In the second stage, each LO path is individually mixed with its corresponding signal path in the 90° optical hybrid, generating eight output optical signals. In the final stage, the eight signals are transformed into current by four BPDs and are then sampled by the analog-to-digital converter (ADC). Based on Eq. (2-16), we write the detected signals in X polarization and Y polarization as

$$\begin{bmatrix} I_x(t) \\ I_y(t) \end{bmatrix} = \begin{bmatrix} 2A_{LO}(t)A_x(t)e^{j(\Delta\omega t+\Delta\varphi)} \\ 2A_{LO}(t)A_y(t)e^{j(\Delta\omega t+\Delta\varphi)} \end{bmatrix} \tag{2-17}$$

2.4. TRANSMISSION IMPAIRMENTS

In general, there are two main types of transmission impairments in an optical fibre transmission system: the linear and nonlinear impairments. In this section, we focus only on the optical device induced impairments and omit those in electronic devices, such as the thermal noise in the circuits. For single-mode fibre employing only one wavelength, the linear impairments mainly include fibre attenuation, CD, PMD, and ASE noise. The nonlinear ones are mainly contributed by SPM, XPM, four-wave mixing, etc.

In order to investigate these effects, we first introduce the nonlinear Schrödinger equation (NLSE) that governs the propagation of optical pulses inside a single-mode fibre [37]

$$\frac{\partial A}{\partial z}+i\frac{\beta_2}{2}\frac{\partial^2 A}{\partial t^2}+\frac{\alpha}{2}A=i\gamma\left|A\right|^2 A \tag{2-18}$$

where A is the signal amplitude, z is the distance the pulses have transmitted, β_2 is the group velocity dispersion coefficient, γ is the nonlinear coefficient and α is the attenuation coefficient. Based on Eq. (2-18), we can further discuss the linear and nonlinear channel impairments in the following sections. The main impairments considered in fibre transmission systems are summarized in Figure 2.10.

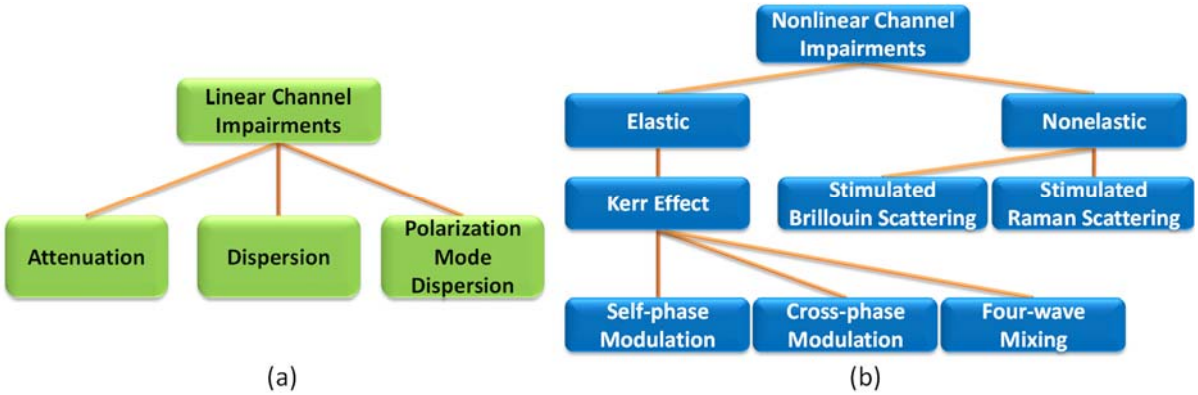

Figure 2.10. Major transmission impairments in single-mode fibres. (a) Linear; (b) nonlinear.

2.4.1. Attenuation

In Eq. (2-18), if we set the dispersion coefficient $\beta_2 = 0$ and the nonlinear coefficient $\gamma = 0$, we have $\frac{\partial \mathrm{A}}{\partial \mathrm{z}}+\frac{\alpha}{2}A=0$. Solving this equation, we can derive

$$\left|A(z,t)\right|^2=\left|A(0,t)\right|^2 e^{-\alpha z} \tag{2-19}$$

Eq. (2-19) describes the evolution of an optical pulse in a single-mode fibre without effects of dispersion and nonlinearity, which shows that the optical power decreases exponentially with the increase of transmission distance. Attenuation is a fundamental linear impairment and is usually compensated using optical amplifiers, namely, EDFAs and SOAs. The attenuation

parameter of a certain type of fibre is normally represented in dB per unit length, related to the linear scale coefficient as $\alpha_{dB} = 4.343\alpha$.

There are three dominant physical mechanisms giving rise to this attenuation: scattering, absorption and radiative loss. The Rayleigh scattering is the fundamental attenuation mechanism resulting from the refraction index fluctuations over the distances that are small enough compared to the operating wavelength. The absorption is due to the resonance peaks of silicon dioxide molecules which occur in the ultraviolet region (electronic resonances) and in the infrared region near 1.6 μm (atomic vibrational resonances). In addition, the OH^- in the fibre, which is caused by the residual water vapour in silica, generates an absorption peak near 1.4 μm. Radiative losses are usually regarded as small compared with the scattering and absorption, since the cladding is normally sufficiently thick with a polymer coating and a protective jacket to buffer external forces and prevent sharp bends.

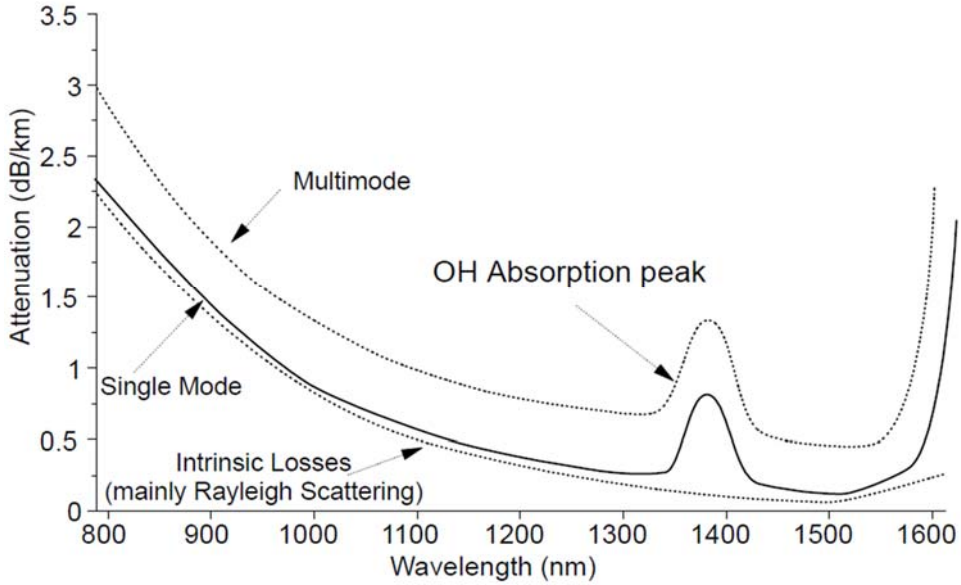

Figure 2.11. Typical fibre infrared absorption spectrum.

In Figure 2.11 [38], the fibre attenuation as a function of wavelength is shown. The appropriate transmission windows can be designed according to the above figure, which normally include three windows. The first window, also called short wavelength band, ranging from 800 nm to 900 nm, was used in the very early days of optical fibre communication, dating back to the 1970s and early 1980s. The second window, also known as the medium wavelength band, is around 1310 nm. This window was first used in the mid-1980s and is also attractive today as there is almost zero fibre dispersion for single-mode fibre within this window. The third window lies between 1510 nm and 1600 nm, also known as the long wavelength band. This window has the lowest attenuation coefficient (0.2 to 0.25 dB/km) based on current fibre manufacturing technology and is thus widely used in academia and industry. In this thesis, all the experiments are carried out in the third window at around 1550 nm.

2.4.2. Chromatic Dispersion

Generally speaking, there are various dispersion effects in a fibre, namely, modal dispersion in multi-mode fibres, material and waveguide dispersion in single-mode fibres. Here, we only consider the dominant dispersion effect in single-mode fibres, i.e. chromatic (material) dispersion. CD is caused by the wavelength dependence of the fibre refractive index. Some wavelengths travel faster than others while some wavelengths travel slower. Since optical pulses consist of a range of wavelengths, CD can thus lead to the broadening of pulses, which eventually causes ISI.

Removing fibre attenuation and nonlinear effects in Eq. (2-18), the equation gives the following solution

$$A(z,\omega) = A(0,\omega)\exp\left\{i\frac{\beta_2\omega^2 z}{2}\right\} \tag{2-20}$$

CD is commonly quantized using the dispersion parameter D, related to the dispersion coefficient β_2 as

$$D = -\frac{2\pi c}{\lambda^2}\beta_2 \tag{2-21}$$

where λ is the central wavelength and c is the speed of light. D has the unit of ps/nm/km with a value of about 17 ps/nm/km for the commercial SSMF at 1550 nm. Furthermore, we can express the transfer function of CD as

$$H(\mathrm{z},\omega) = \exp\left(-iD\cdot\frac{\lambda^2}{2\pi c}\cdot\frac{\omega^2}{2}z\right) \tag{2-22}$$

It is worth noting that the inter-symbol interference due to CD is the dominant one among all channel impairments, which is usually one of the major factors limiting the maximum reachable transmission distance and the highest achievable data rate in optical communication systems.

2.4.3. Polarization Mode Dispersion

In single-mode fibre transmission, the optical pulses can be considered as a combination of two orthogonal polarization states propagating down the fibre. These two states are also known as principle state of polarization (PSP), which is insensitive to the variation of the central wavelength. In an ideally symmetric fibre, the propagation constants of the two PSPs are exactly the same leading to a zero differential group delay (DGD). However, in practice, the existence of imperfect geometry of the fibre, varying external stress and fluctuating temperature all give rise to different refractive indices between the two PSPs, also known as birefringence. Thus, none-zero DGD occurs, causing distortions in the transmitted optical pulses, as intuitively illustrated in Figure 2.12 (a). Such effect is known as PMD.

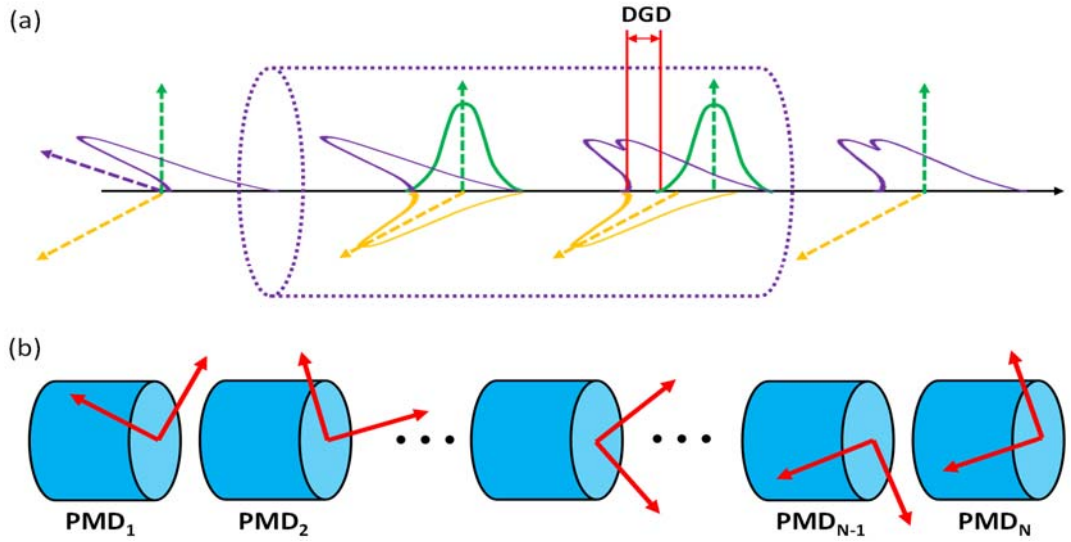

Figure 2.12. Conceptual model of PMD. (a) Simple birefringence device; (b) randomly concatenated birefringence.

The DGD ($\Delta\tau$) is not deterministic, but varies wildly with wavelengths and time. The instantaneous value of DGD follows a Maxwellian distribution, given by [39]

$$f(\Delta\tau)=\frac{32(\Delta\tau)^2}{\pi^2\langle\Delta\tau\rangle^3}\exp\left\{-\frac{4(\Delta\tau)^2}{\pi\langle\Delta\tau\rangle^2}\right\}\quad \Delta\tau\geq 0 \tag{2-23}$$

A long fibre link can be modelled as a sequence of small concatenated linearly birefringent segments. Not only the DGD value in each segment is random, but the directions of the two PSPs also randomly change along the fibre. It can be proved that the DGD distribution of such a concatenated link is also governed by the Maxwellian distribution shown in Eq. (2-23) [39]. The PMD of a single linearly birefringent segment is commonly quantized based on the mean of DGD ($\langle\Delta\tau\rangle$) as $PMD = \langle\Delta\tau\rangle/\sqrt{L}$, where L is the segment length. For a fibre link, the PMD is thus calculated as

$$PMD_{link}=\frac{1}{\sqrt{L_{link}}}\sqrt{\sum_{i=1}^{N}PMD_i^2 L_i} \tag{2-24}$$

In the above discussion, the PMD is assumed to be independent from wavelength, which is known as the first-order PMD. It can be well represented by the PSP model and characterized using Eq. (2-24) with the unit of $ps/\sqrt{km}$. However, PMD is also dependent on wavelength, known as high-order PMD where the variations of PSPs with respect to wavelength are taken into consideration. High-order PMD is characterized using the mean DGD across a certain wavelength range. In optical transmission systems, the first-order PMD is usually the dominant PMD effect and its maximum value for a certain system is given in most standards such as ITU-T. Modern fibre manufacturing technologies can easily keep the maximum fibre PMD within 0.1 $ps/\sqrt{km}$. Therefore, PMD-induced impairments are only obvious enough to degrade

overall system performance for high-speed transmissions over relatively long distances, normally beyond 100 km. For all the experiments in this thesis, which are designed for short-reach applications, the signal distortions due to PMD are relatively small and are not compensated.

2.4.4. Amplified Spontaneous Emission Noise

One of the major sources of additive noise in optical transmission systems is the ASE noise. This noise originates from the spontaneous emission inside the commonly used optical amplifiers to compensate fibre attenuation, such as EDFAs, which is then subsequently amplified in these devices. The ASE noise is normally considered as additive white Gaussian noise (AWGN) within the signal bandwidth. Sometimes, ASE noise is deliberately generated from an EDFA and added onto the optical signal to vary the channel OSNR. For all the experiments in this thesis, the OSNR sensitivity curves are measured using this approach. In addition, it is worth mentioning that although there are various other linear noise sources including quantum shot noise, thermal noise, etc., the ASE noise is usually the dominant one in long-haul transmission systems. For single-mode fibre, an EDFA is normally inserted to compensate fibre attenuation every 80 km. Therefore, the accumulated ASE noise scales with the transmission distance while other types of noises, mainly generating from optical and electronic devices, remain the same. However, in some short-reach applications where the transmission distance is within tens of kilometres, EDFAs are not applied and the receiver sensitivity is the main concern instead of OSNR sensitivity. In such cases, other noises become dominant. In this thesis, in order to cover all potential applications for short-to-medium reach optical links, the longest transmission distance is set as over 1000 km, where the ASE noise dominates and the OSNR sensitivity is our metric to measure system performance.

2.4.5. Nonlinear Impairments

Generally speaking, the nonlinear-index coefficient of silica fibres is much smaller than the other nonlinear optical media. In spite of this, the nonlinear effects inside silica fibres can be observed with relatively low incident power, due to a small effective area and the low power attenuation at wavelength between 1000 nm and 1600 nm. Therefore, the nonlinear effects play important roles in optical transmission systems using single-mode fibres. As shown in Figure 2.10, major fibre nonlinear effects can be categorized as two types: the effects that are due to the nonlinear refractive index (or Kerr effect), such as SPM and XPM; the scattering of the light wave at one frequency into other frequencies, such as the Brillouin and Raman scattering phenomena. In the following sections, we briefly introduce the SPM effect which normally occurs at a relatively low optical power and the XPM effect that becomes a non-negligible issue in WDM systems.

2.4.5.1. Self-phase modulation

Solving Eq. (2-18) in the absence of fibre dispersion, we obtain [40]

$$A(z,t) = A(0,t)\exp\left\{i\gamma\int_0^z \left|A(l,t)\right|^2 dl\right\} \tag{2-25}$$

where the SPM effect is induced by the nonlinear phase term $\varphi_{NL} = \gamma\int_0^z |A(l,t)|dl$. The nonlinear coefficient γ is defined as [40]

$$\gamma = \frac{n_2\omega_c}{cA_{eff}} \tag{2-26}$$

where n_2 is the nonlinear refractive index, ω_c is the central frequency of the light wave, c is the speed of light, and A_{eff} is the effective area of the fibre core. The nonlinear phase φ_{NL} can be further expressed as [40]

$$\varphi_{NL} = \gamma\left|A(0,t)\right|^2 L_{eff} = \gamma\left|A(0,t)\right|^2 \frac{1-e^{-\alpha z}}{\alpha} \tag{2-27}$$

where L_{eff} is the effective transmission length.

Eq. (2-25) indicates that SPM distorts the phase of the transmitted signal, which leads to a broadened spectrum. Thus, for modulation formats utilizing the phase of the optical field as a modulation dimension, the SPM effect contaminates the transmitted signal phase causing error symbol decisions at the receiver. Noticing that φ_{NL} is proportional to the optical power, the normal way of enhancing system performance, which takes advantage of the OSNR improvement through increasing the transmitted power, will not always work. However, there is still a lack of simple DSP-based approaches to perfectly remove the nonlinear impairments. As a consequence, the best system performance achievable is limited by the fibre nonlinear effects.

2.4.5.2. Cross-phase modulation

The incident optical power induced change of the fibre refractive index not only gives rise to phase distortions in the original wavelength, but also interacts with other wavelengths close to it, leading to spectral broadening. Such an effect is known as XPM. XPM is a critical concern in WDM systems, especially for dense WDM (DWDM) systems, where each channel occupies only 50-GHz bandwidth. The total phase shift of the i-th channel is expressed by

$$\varphi_{NL}^i = \gamma L_{eff} P_i + 2\gamma L_{eff}\sum_{j\neq i} P_j \tag{2-28}$$

The first term in Eq. (2-28) denotes the SPM effect caused by the optical power in the i-th channel itself. The second term stands for the XPM effect, where the factor 2 is due to the bipolar effects of the susceptibility of silica materials. The physical mechanism of XPM can be intuitively understood by noticing the fibre refractive index depends not only on the optical power of the i-th channel, but also on the optical intensity of other co-propagating channels. Unlike stimulated Brillouin and Raman scattering, the interaction among different wavelengths through XPM does not lead to power transfer. In practice, XPM is hard to estimate, because the XPM in the i-th channel is determined by the modulation patterns in all the other channels

which is randomly changing with time. However, the XPM is limited by the mismatch of group velocities among all the channels, indicating its reduction by increasing the spectral gaps among the channels [37]. In this thesis, all the experiments are carried out at a single wavelength, and thus, XPM is not considered.

2.5. CLASSICAL DSP ALGORITHMS

As discussed in section 2.3.2, using polarization and phase-diverse coherent detection, both the amplitude and phase of the optical field can be recovered (see Eq. (2-17)), based on which we can apply various DSP algorithms. The DSP facilitated coherent detection is also known as digital coherent detection, which has four major advantages. First, there are already a great number of mature DSP algorithms from other research fields, such as wireless communication, computer science, and control theory, which are ready for implementation in optical transmission systems. Second, advances in electronic microprocessors during the past decade enable powerful signal processing to be performed without excessive cost on chips. Moreover, in the foreseeable future, microprocessors will be cheaper and more powerful, which will further reduce the total cost of DSP-based optical transmission systems and support more complex DSP algorithms. Third, by introducing DSP techniques on both transmitter and receiver sides, advanced modulation formats can be easily implemented, such as DMT and CAP. Last but not least, transmission impairments can be compensated by either receiver DSP algorithms or introducing digital pre-distortions at the transmitter. In this section, we will investigate some of the classical DSP algorithms that have already become *de facto* companions in the standard dual-polarization digital coherent receiver.

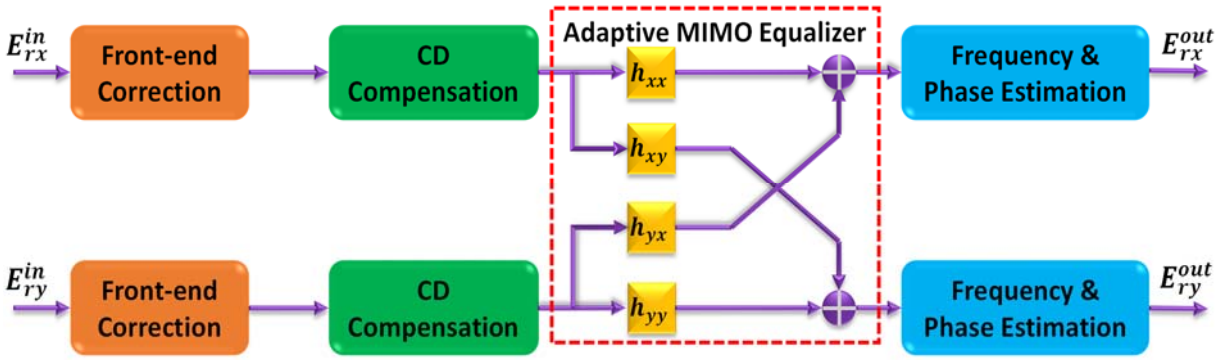

Figure 2.13. DSP flow chart for dual-polarization digital coherent detection.

Figure 2.13 illustrates the typical DSP steps in a dual-polarization digital coherent receiver. The front-end correction is first applied for deskew and power balancing, followed by CD compensation in each polarization. An adaptive equalizer is employed for polarization demultiplexing. Frequency and phase estimation is the final step to equalize the frequency and phase difference between the LO and signal.

2.5.1. Front-end Correction

In practice, it is not atypical to have power and timing mismatches among different paths due to various reasons, such as the imbalance of optical coherent receiver, gain differences of photodetectors, etc. For the output of a dual-polarization coherent receiver, there are two pairs of signals that need to be first equalized, namely, the I_x and Q_x for X polarization, and the I_y and Q_y for Y polarization. The DC component of each signal is first removed by subtracting its mean value, followed by power normalization between the I and Q component. The timing mismatch can be corrected based on the measurement results of system pre-calibration. An alternative approach is estimating the time delay by cross correlating [41]. It is common to have a time delay that is not an integer number of ADC samples. In order to compensate such delays, a frequency domain deskew algorithm is applied. The above procedure is generally called IQ compensation. After reconstruction of the complex signals E_{rx}^{in} and E_{ry}^{in}, similar power balancing and deskew process are carried out between the two polarization paths. Thus, the front-end correction is completed resulting in two well-adjusted signals ready for further processing.

2.5.2. Chromatic Dispersion Compensation

Chromatic dispersion is a fundamental phenomenon in optical fibres, which is one of the critical factors that limits the possible transmission distance and link capacity, especially in long-haul optical communication systems. Due to the above reasons, CD compensation techniques have been explored and discussed for decades. In the early days, before the advent of digital coherent detection, such techniques were mostly based on the intrinsic characteristics of various optical devices, including inverse dispersion fibres [13], chirped fibre Bragg gratings [42], optical phase conjugation [43], fibre Gires-Tournois interferometer [44], etc. Although the electrical compensation approaches were also investigated, yet they were mainly focused on the complex pre-distortion technique [45,46]. The above methods require extra bulky optical or electrical components, increasing both the complexity and cost of the transmission system. With recent advances in optical coherent receiver and electronic DSP, CD compensation becomes simpler, cheaper and more efficient. Taylor first proposed the idea of DSP-based CD compensation in [47]. It was not long before digital equalizers were designed and experimentally demonstrated. Savory implemented a practical finite-impulse response (FIR) filter in [48] and was further extended into an infinite-impulse response (IIR) filter to enhance the effectiveness of CD compensation [49]. In order to employ the above algorithms, the total amount of accumulated CD in the transmission should be estimated. Both data-aided algorithms and blind search estimation methods were extensively explored [50-53].

As discussed in section 2.4.2, in the absence of fibre nonlinear effects, CD is a static linear impairment and is also polarization independent. According to the CD transfer function (see Eq. (2-22)), digital CD compensation approaches can thus be designed by applying the inverse of Eq. (2-22), which can be implemented in either time domain or frequency domain. The time-

domain approach is based on an FIR filter. The filter tap weights are calculated from the truncated impulse response of the inverse CD transfer function with a Kaiser window, which are expressed as [41]

$$h_{cd}[k] = \frac{1}{\sqrt{\rho}} \exp\left\{-i\frac{\pi}{\rho}\left[k - \frac{N-1}{2}\right]^2\right\} \tag{2-29}$$

where k ∈ $[0, N-1]$, and N is the total number of taps given by $N = \lfloor \rho \rceil$ and ρ = $2\pi\beta_2 L/T^2$. Here, β_2 is the dispersion coefficient which can be calculated by Eq. (2-21) and , T are the total fibre length and the time interval between two consecutive sampling points at the receiver ADC, respectively. The frequency-domain compensation method is more straightforward. After transformation into frequency domain by fast Fourier transform (FFT), the signal is multiplied by the inverse of Eq. (2-22), which is then transformed back into time domain using IFFT. Alternatively, a block by block overlap/add or overlap/save method can be used as a frequency-domain version of the FIR approach. The time-domain signal is first divided into blocks. After the tap weights are applied to the FFT of the first block, it is immediately transformed back into time domain by IFFT. The start of next block is a few samples overlapped with the previous one. Similar procedures are carried out on the following blocks till the end of the signal.

In this thesis, we choose the direct frequency-domain compensation algorithm, where the total amount of CD is assumed as a known value calculated from fibre dispersion parameter D and transmission distance L.

2.5.3. Adaptive MIMO Equalization

Polarization demultiplexing is the core equalizer in the dual-polarization digital coherent receiver, constructed using four FIR filters in a butterfly structure as shown in Figure 2.14.

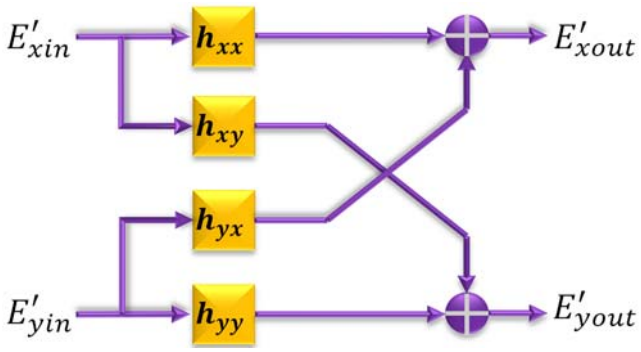

Figure 2.14. Structure of adaptive MIMO equalizer.

In this section, we first introduce the channel model, followed by a thorough investigation on several adaptive multiple-input multiple-output (MIMO) equalization algorithms, namely, constant modulus algorithm (CMA), multi-modulus algorithm (MMA) and decision-directed least mean square algorithm (DD-LMS). We only focus on the implementations of these algorithms instead of theoretically proving their effectiveness and examining their properties.

2.5.3.1. Channel model

We denote the modulated dual-polarization signal at the transmitter as [41]

$$\overrightarrow{E_{tx}}(t)=\begin{bmatrix}E_x(t)\\E_y(t)\end{bmatrix}=\begin{bmatrix}\sum_k(a_k+jb_k)P(t-kT)\\\sum_k(c_k+jd_k)P(t-kT)\end{bmatrix} \tag{2-30}$$

where $a_k+jb_k$and c_k+jd_k are the baseband RF signals for X polarization and Y polarization respectively, $P(t)$ is the pulse shape and T is the time interval between two adjacent sampling points at the receiver ADC. We further assume the transmission channel has a flat frequency response in the absence of polarization dependent loss (PDL) and PMD, then the channel can be approximately modelled by a unitary 2×2 matrix J, also known as the Jones matrix [41]

$$J=\begin{bmatrix}\cos\psi & e^{-j\Gamma}\sin\psi\\-e^{-j\Gamma}\sin\psi & \cos\psi\end{bmatrix} \tag{2-31}$$

where 2ψ and Γ are the azimuth and elevation rotation angles, respectively. Therefore, combining Eq. (2-30) and Eq. (2-31), we can write the received signal as

$$\overrightarrow{E_{rx}}(t)=J\overrightarrow{E_{tx}}(t)=\begin{bmatrix}\cos\psi & e^{-j\Gamma}\sin\psi\\-e^{-j\Gamma}\sin\psi & \cos\psi\end{bmatrix}\begin{bmatrix}E_x(t)\\E_y(t)\end{bmatrix}=\begin{bmatrix}E'_{xin}(t)\\E'_{yin}(t)\end{bmatrix} \tag{2-32}$$

From Eq. (2-32), it is not difficult to infer that the polarization demultiplexing algorithm is aimed to estimate ψ and Γ, i.e. the Jones matrix of the transmission channel. In general, such algorithms can be expressed in a uniform analytical equation as

$$\begin{bmatrix}E'_{xout}\\E'_{yout}\end{bmatrix}=H\begin{bmatrix}E'_{xin}\\E'_{yin}\end{bmatrix}=\begin{bmatrix}h_{xx} & h_{yx}\\h_{xy} & h_{yy}\end{bmatrix}\begin{bmatrix}E'_{xin}\\E'_{yin}\end{bmatrix} \tag{2-33}$$

2.5.3.2. Equalization with CMA and MMA

The CMA algorithm was first proposed by Godard in the 1980s for equalization of quadrature phase-shift keying (QPSK) signals [54], which has been subsequently applied in optical communication systems for polarization demultiplexing. CMA is designed for modulation formats that have a constant optical power, such as QPSK, 4-QAM, etc. Without loss of generality, we assume the received optical power is normalized to 1 (i.e. with a radius of 1 in the 2-D complex plane). The aim of CMA is minimizing the cost functions, defined by

$$\begin{aligned}J_{CMA,x}&=E\left[\left(1-\left|E'_{xout}\right|^2\right)^2\right]\\J_{CMA,y}&=E\left[\left(1-\left|E'_{yout}\right|^2\right)^2\right]\end{aligned} \tag{2-34}$$

In practice, we define the error functions as $e_x^2 = \left(1 - \left|E_{xout}^{'}\right|^2\right)^2$ and $e_y^2 = \left(1 - \left|E_{yout}^{'}\right|^2\right)^2$.

Generally, there are various ways to find the H matrix in Eq. (2-33) that achieves the minimum error function values. One typical approach is the stochastic gradient descent method that forces the differentials of the error functions with respect to h_{ij} $(i, j = x, y)$ to zeros, i.e.,

$$\frac{d\left\langle e_x^2\right\rangle}{dh_{xx}} = 0; \frac{d\left\langle e_x^2\right\rangle}{dh_{yx}} = 0; \frac{d\left\langle e_y^2\right\rangle}{dh_{xy}} = 0; \frac{d\left\langle e_y^2\right\rangle}{dh_{yy}} = 0 \tag{2-35}$$

The adaptive MIMO equalizer can thus be designed as such [55]

$$\begin{aligned}
h_{xx} &\to h_{xx} - \frac{\mu}{4}\frac{de_x^2}{dh_{xx}} = h_{xx} + \mu e_x E_{xout}^{'} \cdot \overline{E_{xin}^{'}} \\
h_{yx} &\to h_{yx} - \frac{\mu}{4}\frac{de_x^2}{dh_{yx}} = h_{yx} + \mu e_x E_{xout}^{'} \cdot \overline{E_{yin}^{'}} \\
h_{xy} &\to h_{xy} - \frac{\mu}{4}\frac{de_y^2}{dh_{xy}} = h_{xy} + \mu e_y E_{yout}^{'} \cdot \overline{E_{xin}^{'}} \\
h_{yy} &\to h_{yy} - \frac{\mu}{4}\frac{de_y^2}{dh_{yy}} = h_{yy} + \mu e_y E_{yout}^{'} \cdot \overline{E_{yin}^{'}}
\end{aligned} \tag{2-36}$$

where $\overline{E_{xın}^{'}}$ and $\overline{E_{yın}^{'}}$ denotes the complex conjugates of $E_{xin}^{'}$ and $E_{yin}^{'}$ respectively.

It is worth noting that the above equalizer can be implemented with a certain number of taps leading to $h_{xx}, h_{yx}, h_{xy}, h_{yy}$ being vectors. Although the CMA algorithm is constrained by the modulation formats, it is rather robust to the frequency and phase mismatches between LO and signal. This can be understood by noticing that the CMA does not contain any phase-related terms. As shown in Figure 2.13, the CMA is employed prior to the frequency and phase estimation.

The MMA algorithm is a modification of CMA, where the cost functions penalize the I and Q components of the received signals separately, given by

$$\begin{aligned}
J_{MMA,x} &= E\left[\left(R_I - \left|E_{xout,I}^{'}\right|^2\right)^2 + \left(R_Q - \left|E_{xout,\mathrm{Q}}^{'}\right|^2\right)^2\right] \\
J_{MMA,y} &= E\left[\left(R_I - \left|E_{yout,I}^{'}\right|^2\right)^2 + \left(R_Q - \left|E_{yout,\mathrm{Q}}^{'}\right|^2\right)^2\right]
\end{aligned} \tag{2-37}$$

Thus, the corresponding updating algorithm of the H matrix is then

$$
\begin{aligned}
h_{xx} &\to h_{xx} + \mu\left[E'_{xout,I}\left(R_I - \left|E'_{xout,I}\right|^2\right) + j \cdot E'_{xout,Q}\left(R_Q - \left|E'_{xout,Q}\right|^2\right)\right] \cdot \overline{E'_{xin}} \\
h_{yx} &\to h_{yx} + \mu\left[E'_{xout,I}\left(R_I - \left|E'_{xout,I}\right|^2\right) + j \cdot E'_{xout,Q}\left(R_Q - \left|E'_{xout,Q}\right|^2\right)\right] \cdot \overline{E'_{yin}} \\
h_{xy} &\to h_{xy} + \mu\left[E'_{yout,I}\left(R_I - \left|E'_{yout,I}\right|^2\right) + j \cdot E'_{yout,Q}\left(R_Q - \left|E'_{yout,Q}\right|^2\right)\right] \cdot \overline{E'_{xin}} \\
h_{yy} &\to h_{yy} + \mu\left[E'_{yout,I}\left(R_I - \left|E'_{yout,I}\right|^2\right) + j \cdot E'_{yout,Q}\left(R_Q - \left|E'_{yout,Q}\right|^2\right)\right] \cdot \overline{E'_{yin}}
\end{aligned}
\tag{2-38}
$$

In Eq. (2-37) and Eq. (2-38), $R_I = E[A_I^4]/E[A_I^2]$ and $R_Q = E[A_Q^4]/E[A_Q^2]$ are defined by the I and Q components of the transmitted baseband signal A. Compared with CMA, MMA not only offers an approach to perform polarization demultiplexing on multi-modulus modulation formats such as 16-QAM, but also has the capability of correcting the phase mismatches due to its inclusion of phase-related terms.

Both CMA and MMA converge the two outputs of the equalizer independently, indicating there is a possibility that the two demultiplexed signals converge to the same transmitted polarization. This issue is known as the singularity problem. During the past decade, various approaches have been proposed to overcome this limitation, including independent component analysis, multi-user CMA, introducing a cross correlation term in the cost function, magnitude-bounded blind source separation, or by the sequentially converging the outputs. The optimal solution to the singularity problem remains an open research problem.

2.5.3.3. Equalization with DD-LMS

DD-LMS is a simpler adaptive MIMO equalizer than CMA and MMA, where symbol decision is first carried out. The cost functions are given by

$$
\begin{aligned}
J_{DD-LMS,x} &= \left| dec\left(E'_{xin}\right) - E'_{xin} \right|^2 \\
J_{DD-LMS,y} &= \left| dec\left(E'_{yin}\right) - E'_{yin} \right|^2
\end{aligned}
\tag{2-39}
$$

where "dec" stands for the symbol decision process.

The corresponding updating algorithm of the H matrix is then expressed as

$$
\begin{aligned}
h_{xx} &\to h_{xx} + \mu e_x \cdot \overline{E'_{xin}} \\
h_{yx} &\to h_{yx} + \mu e_x \cdot \overline{E'_{yin}} \\
h_{xy} &\to h_{xy} + \mu e_y \cdot \overline{E'_{xin}} \\
h_{yy} &\to h_{yy} + \mu e_y \cdot \overline{E'_{yin}}
\end{aligned}
\tag{2-40}
$$

where $e_x = \left| dec\left(E'_{xin}\right) - \left|E'_{xout}\right| \right|$ and $e_y = \left| dec\left(E'_{yin}\right) - \left|E'_{yout}\right| \right|$. The accuracy of DD-LMS largely depends on the symbol decision procedure. With a relatively large number of decision errors, DD-LMS may converge to the wrong values or even cannot converge.

Therefore, in practice, in order to obtain the optimal performance, the decision process is replaced by training symbols, which are assumed as known at the receiver.

In this thesis, as the experiments are all carried out with the PAM-4 format, MMA is the most appropriate algorithm for polarization demultiplexing.

2.5.4. Frequency and Phase Estimation

After polarization demultiplexing, the frequency and phase mismatches between LO and the signal are then compensated based on various estimation algorithms. For state-of-the-art optical coherent detection, the LOs are usually external cavity lasers (ECLs) with linewidths below 100 kHz, with the frequency difference between LO and the transmitter laser kept below 100 MHz for reliable frequency locking. However, it is always desirable to employ cost-effective lasers such as DMLs with linewidths in the MHz range and also to relax the requirement on the frequency alignment of LO and the transmitter laser. Needless to say, the accurate recovery of the signal phase is vital for the overall system performance, and can be achieved based on the powerful digital compensation algorithms.

Early efforts have been made to lock the phase of the LO since the 1980s, in which an optical phase-locked loop (PLL) was employed [56,57]. However, even today, the optical PLL is still difficult to build due to the lack of a practical voltage-controlled oscillator (VCO) that can be precisely operated at the optical stage. In the past decade, with the rapid growth in the computation power of microprocessors, numerous DSP-based simple yet effective methods have been proposed to estimate the phase of the LO. It has been shown that the maximum a posteriori (MAP) phase estimation achieves the true optimal estimate, but it is not feasible for implementations on real-time DSP chips [58]. The digital PLL has been successfully applied to various optical communication systems with external modulators as transmitters [59-61]. In [59], a 160-Gb/s PDM 16-QAM single channel transmission over 3123.9-km SSMF was demonstrated making use of a digital PLL as the frequency offset compensator. And in [60], a modified decision-directed PLL (DD-PLL) was applied to carrier phase and frequency estimation in a 112-Gb/s PDM 16-QAM system in which the reference constellation was rotated in steps of $\pi/20$ to get the most likely phase angle corresponding to the smallest mean-square error. Employing a second-order digital PLL, frequency offset and laser phase noise was jointly compensated in [61].

The digital PLL is a quite general approach. However, in real-time coherent transmission systems, due to the inevitable time delay in the feedback path of the PLL, there is an upper limit of the allowable LO linewidth [58]. In order to overcome such obstacles, people have noticed the fact that for particular modulation formats, the specific distribution of the constellation points can also be utilized as extra information for frequency and phase estimation. Therefore, a plenty of alternative approaches have been proposed to enable hardware parallelization and pipelining, such as the power law-average phase estimate and its variations [62-64] for M-PSK and M-QAM formats, differential phase based methods for frequency offset estimation in QPSK format [55]. It has been proved that the Wiener filter-based power law-average

estimation algorithm is practical which can also achieve the near-optimal estimate given by the MAP estimation approach [58].

In this thesis, the modulation format is PAM-4 at a single wavelength, where the aforementioned compensation approaches based on regular complex modulation formats cannot be employed. Thus, we propose two methods for frequency offset and phase mismatch compensation: (i) linear fitting; and (ii) digital PLL.

After polarization demultiplexing, the output signal of the adaptive equalizer in either polarization can be expressed by $A(t)exp\left\{i\cdot\left(2\pi\Delta ft+\varphi(t)\right)\right\}$, where Δf is the LO frequency offset and $\Delta\varphi$ is the remaining phase component including meaningful phase information from the baseband modulation, transmitter laser and LO phase noise, etc. It is reasonable to assume within the data frame under consideration, Δf remains constant and thus the phase of the signal $2\pi\Delta ft+\varphi(t)$ can be approximated as a linear function with respect to t. By linearly fitting the measured absolute phase values, Δf is obtained from the slope of the fitted line. Despite the simplicity of this approach, it is apparent that Δf is required to be large enough to guarantee that $\varphi(t)$ can be treated as small fluctuations compared with $2\pi\Delta ft$.

The digital PLL is an alternative method. We design the loop filter as a standard proportional-integral (PI) controller in the form of

$$H(s)=\frac{\tau_2 s+1}{\tau_1 s} \tag{2-41}$$

where τ_1 and τ_2 are the parameters to be configured and s denotes the complex frequency. As the overall shape of $2\pi\Delta ft+\varphi(t)$ resembles a ramp signal, to achieve theoretical zero steady-state tracking error, we introduce another pole by attaching an integration section K/s. Thus, we obtain the open loop transfer function as

$$G(s)=\frac{\tau_2 s+1}{\tau_1 s}\cdot\frac{K}{s} \tag{2-42}$$

Using bilinear transformation, a digitized version of Eq. (2-42) is applied in our experiments with the parameters τ_1, τ_2 and K adjusted correspondingly to obtain the optimal system performance.

In this thesis, due to the complex parameter tuning procedure for digital PLL and its limited performance enhancement in our experiments, linear fitting is chosen as the frequency offset and phase mismatch compensation algorithm.

2.6. CONCLUSIONS

In this chapter, we investigated the basic subsystems of a typical short-to-medium reach optical transmission system. We first gave an introduction to several commonly used transmitters, including the DML, the EML and the traditional external modulators, namely MZM intensity modulators and optical I/Q modulators. We then briefly discussed the general principles of some of the advanced modulation formats that have been extensively explored and

demonstrated in the past five years, namely, PAM, CAP and DMT. After an introduction to pulse shaping filters as the last section in transmitter subsystems, the details of optical coherent detection were provided. From the fundamental concept of coherent detection, we derived the full-blown dual-polarization optical coherent receiver step by step. In the following section, the main transmission impairments inside an SSMF were investigated, which can be categorized as linear and nonlinear impairments. For the last part in this chapter, some of the typical DSP algorithms used in a digital coherent receiver were presented in details, which includes front-end correction, CD compensation, adaptive MIMO equalization and carrier frequency and phase estimation. We especially examined the polarization demultiplexing algorithm which is one of the key procedures in the dual-polarization digital coherent receiver, such as CMA, MMA and DD-LMS. Along with all the above introductions, we also addressed the algorithms that will be employed in the experiments in chapter 3 and 4.

Chapter 3
Simulation and Analysis of Directly Modulated Lasers

3.1. INTRODUCTION

During the past few decades, benefiting from the progress in optical and electrical devices, optical communication has advanced in leaps and bounds. As one of the key components in an optical transmission link, the semiconductor laser has gradually become the dominant light source. From the low-cost DML which is preferred for short-to-medium reach optical links, to the high performance ECL that is widely used in long-haul transmission, the semiconductor laser is indispensable in almost all optical communication applications. The physical nature of the semiconductor laser has been extensively explored since its invention in the 1960s. Theoretical models have been built and analysed for the active region of either a single-mode or multi-mode semiconductor laser, such as the lumped rate equation model [65,66] and the most precise model developed from the density matrix theory [67]. Furthermore, taking the external cavity into consideration, various numerical methods have also been developed to better simulate the laser behaviour as a whole, such as the transmission line model [68] and the split-step time domain model [69] that is based on the coupled-wave equations and the carrier rate equations. The above approaches have been shown to successfully reveal the major characteristics of different types of lasers, including multi-electrode DFB laser diodes [70], mode-locked laser diodes [71], and super-structure grating distributed Bragg reflector (DBR) laser diodes [72], etc. In recent years, the two major commercially available types of DMLs suitable for short-to-medium reach optical transmission systems are the DFB laser and the VCSEL. Therefore, in order to gain a better understanding of the DML behaviour and then fully utilize its characteristics for optical transmission purposes, it is worthwhile developing an appropriate simulation model.

In this chapter, we first introduce the theoretical background of the classical rate equation model for single-mode semiconductor lasers, based on which we analyse the laser steady-state characteristics, and the small/large signal dynamics of the laser active region. We also show that the frequency chirp can be properly described using our model. We further investigate the intrinsic laser noises generated from the fluctuations of carrier and photon densities and add

extra noise terms into our model. Finally, we focus on the thermal FM of DML and experimentally characterize the dynamic frequency chirp originated from fast temperature changes in a DFB laser using optical coherent receiver. We report the observation of a 7.5-ns time constant and the system impact of such a fast time constant is also theoretically analysed.

3.2. CLASSICAL RATE EQUATIONS

3.2.1. Basic Principles of Light Emission

The foundation of laser theory was first established in 1958 by Schawlow and Townes [73] and was soon demonstrated through experiments in a ruby laser and a He-Ne laser in the early 1960s [74-76]. The basic principle of semiconductor laser is based on the amplification of optical wave which is majorly generated by the stimulated emission of photons invoked by optical transition of electrons inside semiconductor materials [77]. The above process is illustrated in Figure 3.1.

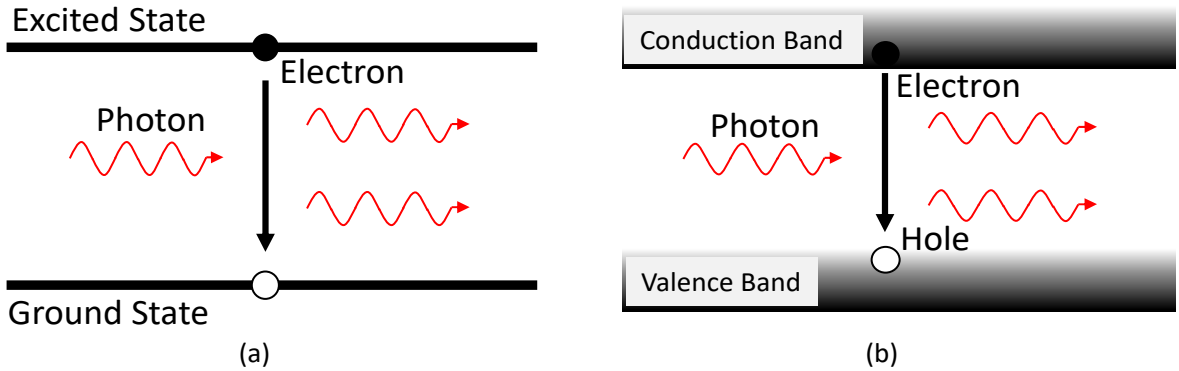

Figure 3.1. Stimulated emission of a photon. (a) In an atom; (b) in a semiconductor.

According to Bohr's atomic model, the energy of an electron inside an atom is not continuous, but has discrete values, corresponding to different energy levels. As shown in Figure 3.1 (a), considering a simple case with only two energy levels, we assume the energy difference between these two levels is E and only the upper level is occupied by an electron. When a photon with the exact energy of $E = \hbar\omega$ is incident (ω is the angular frequency of the optical wave and $\hbar = h/2\pi$, h is the Plank constant), there is a probability for the electron to transfer from the upper level to the lower level. In the meantime, a photon with the same state as the incident one is emitted. Here the same state means the two photons have the same frequency, phase, propagation direction and polarization. The process is quite similar inside a semiconductor, except for the fact that instead of having discrete levels, the electron energy forms a band structure. As illustrated in Figure 3.1 (b), we assume the semiconductor is in a state where there are plenty of electrons in the conduction band and plenty of holes in the valence band. If the energy of the incident photon exactly matches the gap between the two bands, light emission takes place, with the generation of an exactly copied photon of the incident

one. The above process is known as stimulated emission based on which optical amplification is obtained and the semiconductor starts to lase.

The stimulated emission acts as the driving source inside the active region of a semiconductor laser to make it function. Besides, there are various other phenomena happening simultaneously, such as spontaneous emission, photon loss, etc. In the following sections, a complete derivation of single-mode laser rate equation is described taking consideration of all major processes in the laser active region.

3.2.2. Derivation of the Basic Laser Rate Equation

3.2.2.1. Carrier generation and recombination

The electron-hole pair is generally called carrier and its density is denoted as $N(t)$. The carrier density in the laser active region follows a simple dynamic given as follows

$$\frac{\partial N(t)}{\partial t} = G_{gen} - G_{rec} \tag{3-1}$$

where G_{gen} and G_{rec} represent the rate of carrier generation and the rate of carrier recombination respectively. The only source of carrier generation is the current injected into the active region which is represented by the electron injection rate per volume given by $I(t)/eV_a$, where $I(t)$ is the total injected current, e is the electron charge and V_a is the volume of active region. We can then write the carrier generation rate as $G_{gen} = I(t)/eV_a$. The carrier recombination process is much more complicated, generally separated as three major phenomena, the spontaneous recombination (R_{sp}), the non-radiative recombination (R_{nr}), and the net stimulated recombination (R_{st}). We can write

$$G_{rec} = R_{sp} + R_{nr} + R_{st} \tag{3-2}$$

It is common to describe the first two terms in the above equation which is known as the unstimulated carrier decay by a carrier lifetime τ_n. The stimulated recombination (R_{st}) is related to the generation of photons whose details will be given in the next section. Thus, G_{rec} can be expressed by

$$G_{rec} = \frac{N(t)}{\tau_n} + R_{st} \tag{3-3}$$

The above expression is an intuitive model of carrier recombination rate. Furthermore, G_{rec} can also be approximated using a polynomial form, given by

$$G_{rec} = B \cdot N(t)^2 + \left(A \cdot N(t) + C \cdot N(t)^3 \right) + R_{st} \tag{3-4}$$

where A is the linear recombination coefficient, B is the spontaneous recombination coefficient and C is the Auger recombination coefficient. To be more specific, $R_{sp} = B \cdot N(t)^2$ and $R_{nr} = A \cdot N(t) + C \cdot N(t)^3$.

Without loss of generality, we use Eq. (3-3) as our model to describe the dynamics of the carrier density, resulting in the final form shown in the following equation

$$\frac{\partial N(t)}{\partial t} = \frac{I(t)}{eV_a} - \frac{N(t)}{\tau_n} - R_{st} \tag{3-5}$$

3.2.2.2. Photon generation and loss

The dynamics of the photon density consists of the photon generation and the photon loss. The photons inside a laser are generated through the electron-hole pair recombination with the majority contributed by the stimulated emission described in section 3.2.1. And the rest is generated from the spontaneous emission of carriers. The photon loss at lasing wavelength(s) generally consists of the external photon loss that is originated from the optical absorption and scattering inside the laser cavity, and the mirror photon loss which is caused by the reflection facets of the laser diode. In general, the photon loss is normally represented by a photon lifetime constant τ_p. Therefore, the dynamics of photon density can be modelled as

$$\frac{dS(t)}{dt} = \Gamma R_{st} + \Gamma R_{sp} - \frac{S(t)}{\tau_p} \tag{3-6}$$

It is worth mentioning that the volume occupied by the photons V is larger than the volume occupied by the carriers, known as the active region volume V_a. Therefore, if the stimulated carrier recombination rate is R_{st}, then the stimulated photon generation rate is $(V_a/V) \cdot R_{st}$. Here, the coefficient V_a/V is commonly called the confinement factor denoted as Γ in Eq. (3-6). So far, the rate equation for photon density can be written as

$$\frac{dS(t)}{dt} = \Gamma R_{st} + \Gamma\beta\frac{N(t)}{\tau_n} - \frac{S(t)}{\tau_p} \tag{3-7}$$

where the coefficient β is the ratio of spontaneous emissions that are contributed to generating new photons at the lasing wavelength(s) in all the possible spontaneous emissions which form a broad spectrum.

3.2.2.3. Net stimulated emission

Let's now consider the stimulated emission part (R_{st}) that stems from photon-stimulated electron-hole pair recombination. Suppose the initial value of the photon density is S_0 and after a small cavity length Δl, the photon density increases by ΔS. The growth of the photon density is modelled as an exponential function with a coefficient g denoting the gain per unit length, and can thus be expressed as

$$S_0 + \Delta S = S_0 \cdot e^{g \cdot \Delta l} \tag{3-8}$$

For a sufficient small Δl, we have $e^{g \cdot \Delta l} \approx 1 + g \cdot \Delta l$. Noticing $\Delta l = v_g \cdot \Delta t$, where v_g is the group velocity of the optical wave in the cavity, we finally arrive at

$$\Delta S = v_g \cdot g \cdot S_0 \cdot \Delta t \tag{3-9}$$

Therefore, the rate of net stimulated emission can then be expressed as

$$R_{st} \approx \frac{\Delta S}{\Delta t} = v_g \cdot g \cdot S_0 \tag{3-10}$$

Generally, the gain g is a function of the lasing wavelength and the carrier density, given by $g = g(N(t), \lambda)$. The modelling of the gain g can result in complicated forms and is commonly expressed by a high-order polynomial of $N(t)$ and λ. For simplicity, the wavelength dependence of g is ignored since we are considering an ideal single-mode laser and the carrier density dependence is modelled using the 1st-order polynomial of $N(t)$. Finally, we arrive at the following equation for g

$$g = a_0 N(t) - a_0 N_0 \tag{3-11}$$

where N_0 is the carrier density at transparency and a_0 is the scaling factor.

Till now, we have already derived the classical rate equation of the carrier density and photon density, which is expressed by

$$\begin{aligned} \frac{dS(t)}{dt} &= \Gamma v_g a_0 \left(N(t) - N_0\right) S(t) - \frac{S(t)}{\tau_p} + \frac{\Gamma \beta N(t)}{\tau_n} \\ \frac{dN(t)}{dt} &= \frac{I(t)}{eV_a} - v_g a_0 \left(N(t) - N_0\right) S(t) - \frac{N(t)}{\tau_n} \end{aligned} \tag{3-12}$$

3.2.3. Laser Frequency Chirp

Based on the fundamental laser rate equations, we introduce an intrinsic phenomenon in every semiconductor laser diode. On the one hand, as shown in Eq. (3-11), variation of the carrier density modulates the gain, and thus changes the laser output power, given as $P(0) \cdot exp(g_c l)$. On the other hand, the laser output power can be written by the effective refractive index $n_{eff} = n_R - i \cdot n_I$ as follows

$$P(l) = P(0) \cdot \left| \exp\left(-i \frac{2\pi}{\lambda_0} n_R l - \frac{2\pi}{\lambda_0} n_I l \right) \right|^2 = P(0) \cdot \exp\left(-\frac{4\pi}{\lambda_0} n_I l \right) \tag{3-13}$$

where λ_0 is the wavelength in vacuum. Thus, we obtain the following relation between the gain g_c and the effective refractive index

$$g_c = -\frac{4\pi}{\lambda_0} n_I \tag{3-14}$$

Using the definition of linewidth enhancement factor α, we have

$$\alpha = \frac{dn_R}{dn_I} = -\frac{4\pi}{\lambda_0} \frac{dn_R}{dg_c} \tag{3-15}$$

Assuming that the laser emission frequency satisfies the Fabry-Perot cavity resonance condition

$$l = m\frac{c_0}{2n_R}\frac{1}{f} \Rightarrow f = m\frac{c_0}{2n_R}\frac{1}{l} \tag{3-16}$$

By taking the derivative of f with respect to the carrier density $N(t)$, we have

$$\frac{df}{dN} = -\frac{m}{2\cdot l\cdot n_R}\frac{c_0}{n_R}\frac{dn_R}{dN} = -\frac{1}{\lambda_0}\frac{c_0}{n_R}\frac{dn_R}{dN} = -\frac{1}{\lambda_0}v_g\frac{dn_R}{dN} \tag{3-17}$$

Noticing that g_c is the net cavity gain of photon density, given by $g_c = \Gamma g - \frac{1}{\tau_p} = \Gamma a_0(N - N_0) - \frac{1}{\tau_p}$, we thus can obtain

$$\frac{df}{dN} = -\frac{1}{\lambda_0}v_g\frac{dn_R}{dg_c}\frac{dg_c}{dN} = \frac{\alpha}{4\pi}v_g\frac{dg_c}{dN} = \frac{\alpha}{4\pi}v_g\Gamma a_0 \tag{3-18}$$

Therefore, the frequency chirp Δf can be finally expressed by

$$\Delta f \approx \frac{\alpha}{4\pi}v_g\Gamma a_0\cdot\Delta N \tag{3-19}$$

Considering $f = 2\pi\frac{d\varphi}{dt}$ and ignoring the variation notation Δ, the phase of the output optical field is

$$\frac{d\varphi}{dt} = \frac{1}{2}\alpha\cdot v_g\cdot g_c = \frac{1}{2}\alpha\left\{\Gamma v_g a_0\left(N - N_0\right) - \frac{1}{\tau_p}\right\} \tag{3-20}$$

3.2.4. The Complete Rate Equation Model

From the derivation in the above section, we reach the classical rate equations, which reflect the interaction between the photons and the carriers in a semiconductor laser with carrier-induced frequency chirp included. It is concluded as follows [78]

$$\begin{aligned}
\frac{dS(t)}{dt} &= \Gamma v_g a_0\frac{N(t) - N_0}{1 + \varepsilon S(\mathrm{t})}S(t) - \frac{S(t)}{\tau_p} + \frac{\Gamma\beta N(t)}{\tau_n}\\
\frac{dN(t)}{dt} &= \frac{I(t)}{eV_a} - v_g a_0\frac{N(t) - N_0}{1 + \varepsilon S(\mathrm{t})}S(t) - \frac{N(t)}{\tau_n}\\
\frac{d\varphi(t)}{dt} &= \frac{1}{2}\alpha\left\{\Gamma v_g a_0\left(N(t) - N_0\right) - \frac{1}{\tau_p}\right\}
\end{aligned} \tag{3-21}$$

where $S(t)$ is the photon density, $N(t)$ is the electron density, $\varphi(t)$ is the optical phase, Γ is the optical confinement factor, v_g is the group velocity, a_0 is the active layer gain coefficient, N_0 is the carrier density at transparency, τ_n, τ_p and β are carrier lifetime, photon lifetime and spontaneous emission factor respectively, V_a is the volume of the laser active region, ε is the gain saturation parameter, e,h,and η are electron charge, Planck constant, laser frequency and quantum efficiency. The laser power output from one of the laser facet is given by $P = SV_a\eta\upsilon/(2\Gamma\tau_p)$. The expression of rate equations here differs from the above derivation by

taking the nonlinearity of the laser gain into consideration, which is commonly included by a phenomenological form shown in Eq. (3-21) using the gain saturation parameter ε.

In summary, the particle flow inside a typical single mode semiconductor laser is shown in Figure 3.2.

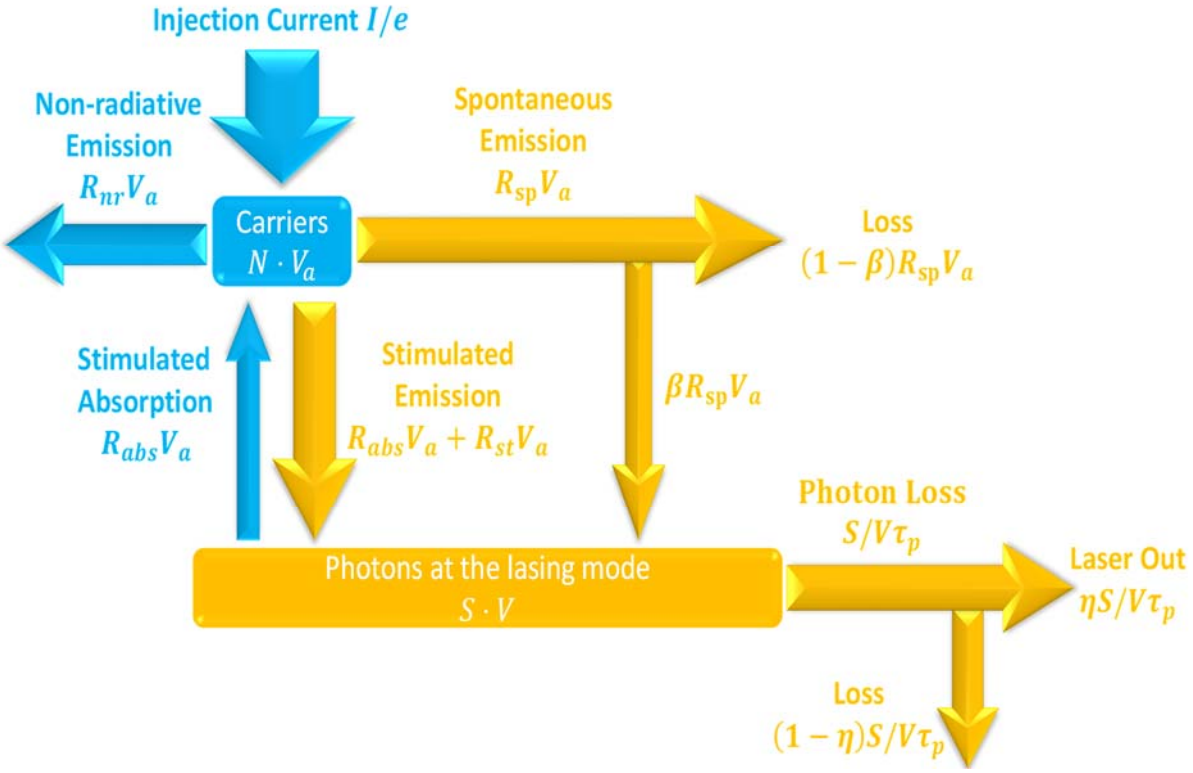

Figure 3.2. Particle flow in a single-mode semiconductor laser.

The majority of the carriers in the active region (V_a) are generated by the injection current. Some of the carriers recombine without emitting photons, which is called the non-radiative emission. Some of the carriers recombine to generate spontaneous emission resulting in a broad spectrum. A small portion of the spontaneous emission contributes to the photons at the lasing mode which has a much narrower spectrum. The rest of the carriers form the stimulated emission which is the major source of photon generation at the lasing mode. On the photon side, a small portion of the photons are absorbed to generate new carriers, which is called the stimulated absorption. The rest of the photons are lost by absorption, scattering and most importantly, coupling out from the mirrors at the end of the laser external cavity, which contributes to the final laser output. The ratio of the photons that are coupled out is denoted as η, also known as the general quantum efficiency.

Thus, we reach the complete rate equation model to reveal the dynamics inside a single-mode semiconductor laser. By solving Eq. (3-21), the dynamics of the laser output power and carrier-induced frequency chirp can be strictly described, which is helpful to get an understanding of the detailed behaviour of a DML under modulation.

3.3. NOISES IN SEMICONDUCTOR LASERS

3.3.1. The Concept of Langevin Force

Although the model described in section 3.2 is usually good enough to simulate a semiconductor laser under most conditions, yet the laser noises have not been included, which can have significant impacts on the overall performance of optical transmission systems. The origin of the laser noise can be understood by noticing the fact that the spontaneous and stimulated emission of photons is not a process precisely described by the above equations. In contrast, it is a random process whose fluctuations cause the carrier and photon densities to vary randomly with time. Such a noisy laser model is achieved using the well-known Langevin force approach. This approach models the random fluctuations of carrier and photon densities into forcing terms in the laser rate equation and the noises can be well simulated by directly solving Eq.(3-21). The principles are explained as follows.

Considering two different kinds of particles a and b, interacting with each other following the equations below

$$\begin{aligned}\frac{dN_a(t)}{dt} &= G_{aa} + G_{ab} - L_{aa} - L_{ab} \\ \frac{dN_b(t)}{dt} &= G_{bb} + G_{ba} - L_{bb} - L_{ba}\end{aligned} \tag{3-22}$$

where N_a and N_b stand for the total number of particle a and b, respectively. G_{ii} and G_{ij} describe the generation of particle i ($i = a\ or\ b$), caused by stimulation of i itself and by transferring from j, respectively. L_{ii} and L_{ij} describe the loss of particle i, caused by recombination of i itself and by transferring to j, respectively. It is obvious that $G_{ab} = L_{ba}$ and $G_{ba} = L_{ab}$. We assume the system is in steady state, which gives $\frac{dN_a}{dt} = 0$ and $\frac{dN_b}{dt} = 0$.

The random nature of generation and loss of the particles can be modelled through random perturbations from the steady state as $N(t) = N_{st}(t) + \delta N(t)$. $N_{st}(t)$ is the steady state value of the total number of the particle and $\delta N(t)$ is a random process with zero average value, varying $N_{st}(t)$ by one at random time t_i. By taking the time derivative, we obtain

$$\frac{dN(t)}{dt} = \frac{dN_{st}(t)}{dt} + \frac{d\delta N(t)}{dt} = G + F_N(t) = G + \sum_i c_i \delta(t - t_i) \tag{3-23}$$

where G is the generation rate of the particle and $\delta(t)$ is the Dirac function with $c_i = \pm 1$ denoting the weights at time t_i.

The autocorrelation function of $F_N(t)$ can be simply derived as

$$\begin{aligned}R_{NN}(\tau) &= \langle F_N(t) F_N(t-\tau) \rangle = \left\langle \sum_i \delta(t - t_i) \delta(t - t_i - \tau) \right\rangle \\ &= \delta(\tau) \left\langle \sum_i \delta(t - t_i) \right\rangle = G\delta(\tau)\end{aligned} \tag{3-24}$$

where the bracket denotes taking average on time.

Taking the above analysis into Eq. (3-22), we have

$$\begin{aligned}\frac{dN_a(t)}{dt} &= G_{aa} + G_{aa}(t) + G_{ab} + G_{ab}(t) - L_{aa} + L_{aa}(t) - L_{ab} - L_{ab}(t) \\ &= G_{aa} + G_{ab} - L_{aa} - L_{ab} + F_a(t) \\ \frac{dN_b(t)}{dt} &= G_{bb} + G_{bb}(t) + G_{ba} + G_{ba}(t) - L_{bb} + L_{bb}(t) - L_{ba} - L_{ba}(t) \\ &= G_{bb} + G_{ba} - L_{bb} - L_{ba} + F_b(t)\end{aligned} \tag{3-25}$$

with the correlation functions given by

$$\begin{aligned}R_{aa}(\tau) &= \langle F_a(t) F_a(t-\tau) \rangle = (G_{aa} + G_{ab} + L_{aa} + L_{ab})\delta(\tau) \\ R_{bb}(\tau) &= \langle F_b(t) F_b(t-\tau) \rangle = (G_{bb} + G_{ba} + L_{bb} + L_{ba})\delta(\tau) \\ R_{ab}(\tau) &= \langle F_a(t) F_b(t-\tau) \rangle = -(L_{ab} + L_{ba})\delta(\tau)\end{aligned} \tag{3-26}$$

3.3.2. The Rate Equation Model with Laser Noises

In this section, we apply the basic principles of Langevin forces introduced in section 3.3.1 to the rate equation model of the semiconductor laser. For the reason of convenience, we rewrite Eq. (3-21) using the total number of photon and carrier and after adding the Langevin force terms, we obtain [79]

$$\begin{aligned}\frac{d(S(t)V)}{dt} &= \Gamma v_g a_0 \frac{N(t) - N_0}{1 + \varepsilon S(\mathrm{t})} S(t)V - \frac{S(t)V}{\tau_p} + \frac{\Gamma \beta N(t) V}{\tau_n} + F_s(t) \\ \frac{d(N(t)V_a)}{dt} &= \frac{I(t)}{e} - v_g a_0 \frac{N(t) - N_0}{1 + \varepsilon S(\mathrm{t})} S(t)V_a - \frac{N(t)V_a}{\tau_n} + F_N(t) \\ \frac{d\varphi(t)}{dt} &= \frac{1}{2}\alpha \left\{ \Gamma v_g a_0 (N(t) - N_0) - \frac{1}{\tau_p} \right\} + F_\varphi(t)\end{aligned} \tag{3-27}$$

The functions $F_S(t)$, $F_N(t)$ and $F_\varphi(t)$ are Langevin noise sources and V is the photon modal volume given by $V = V_a/\Gamma$. The noise sources $F_S(t)$ and $F_\varphi(t)$, which are originated from the overall effects of many independent sources of spontaneous emission, are typically modelled by a Gaussian process with zero mean value. $F_N(t)$ is considered to arise from the shot noise and should form a Poisson process. However, the event rate is so high that due to the law of large numbers, it can also be approximately considered as a Gaussian process. According to Eq. (3-26), the variances of the three noise forces are evaluated from the autocorrelation functions of the noise sources, which are given by

$$\begin{aligned}\left\langle F_S(t)F_S(t')\right\rangle &= V_{SS}\delta(t-t')\\ \left\langle F_N(t)F_N(t')\right\rangle &= V_{NN}\delta(t-t')\\ \left\langle F_\varphi(t)F_\varphi(t')\right\rangle &= V_{\varphi\varphi}\delta(t-t')\end{aligned} \tag{3-28}$$

where $V_{SS}(t)$, $V_{NN}(t)$ and $V_{\varphi\varphi}(t)$ are the variances of autocorrelations, and δ is Dirac's delta function.

Thus, the variances can be expressed as [79]

$$\begin{aligned}V_{SS}(t) &= \Gamma v_g a_0 \frac{N(t)+N_0}{1+\varepsilon S(\mathrm{t})}S(t)V + \frac{S(t)V}{\tau_p} + \frac{\Gamma\beta N(t)V}{\tau_n}\\ V_{NN}(t) &= \frac{I(t)}{e} + v_g a_0 \frac{N(t)+\mathrm{N}_0}{1+\varepsilon S(\mathrm{t})}S(t)V_a + \frac{N(t)V_a}{\tau_n}\\ V_{\varphi\varphi}(t) &= \frac{V_{SS}(t)}{4(S+1)^2}\end{aligned} \tag{3-29}$$

In order to apply the above generated equations to the laser simulation model, it is worth noticing the assumption that between the interval of two simulation time points Δt, the laser is in a quasi-steady state. Based on such assumption, the delta function can be calculated as $1/\Delta t$. At each simulation point, the Langevin forces can thus be calculated according to the following equations

$$\begin{aligned}F_S(t) &= \sqrt{\frac{V_{SS}(t)}{\Delta t}}g_S\\ F_N(t) &= \sqrt{\frac{V_{NN}(t)}{\Delta t}}g_N\\ F_\varphi(t) &= \sqrt{\frac{V_{\varphi\varphi}(t)}{\Delta t}}g_\varphi\end{aligned} \tag{3-30}$$

where g_S, g_N and g_φ are Gaussian probability distribution functions with zero mean values and unity variances.

3.4. SIMULATION MODEL

3.4.1. The Runge-Kutta Algorithm

Based on Eq. (3-27), a real-time laser model can be programmed using the Matlab® built-in block diagram environment Simulink®, which is widely used for real-time systematic simulations. The laser model is programmed in level-2 S-function, driven by the Simulink® ordinary differential equation (ODE) solver engine.

We choose the 4th-order Runge-Kutta method, which is a general algorithm to numerically solve ODEs. Suppose we have the following 1st-order ODE set

$$\begin{cases} \dfrac{dy_1}{dx} = f_1\left(x, y_1, y_2 \cdots, y_m\right) \\ \dfrac{dy_2}{dx} = f_2\left(x, y_1, y_2 \cdots, y_m\right) \\ \quad \vdots \\ \dfrac{dy_m}{dx} = f_2\left(x, y_1, y_2 \cdots, y_m\right) \end{cases} \quad \text{with} \quad \begin{cases} y_1\left(x_0\right) = x_1^0 \\ y_2\left(x_0\right) = x_2^0 \\ \quad \vdots \\ y_m\left(x_0\right) = x_m^0 \end{cases} \tag{3-31}$$

The values of the variables y_i $(i = 1,2,\cdots,m)$ in $k+1$ step are calculated using 4th-order Runge-Kutta method as

$$\begin{cases} y_1^{k+1} = y_1^k + \dfrac{h}{6}\left(K_{11} + 2K_{12} + 2K_{13} + K_{14}\right) \\ y_2^{k+1} = y_2^k + \dfrac{h}{6}\left(K_{21} + 2K_{22} + 2K_{23} + K_{24}\right) \\ \quad \vdots \\ y_m^{k+1} = y_m^k + \dfrac{h}{6}\left(K_{m1} + 2K_{m2} + 2K_{m3} + K_{m4}\right) \end{cases} \tag{3-32}$$

where

$$\begin{cases} K_{i1} = f_i\left(x_k, y_1^k, y_2^k, \cdots, y_m^k\right) \\ K_{i2} = f_i\left(x_k + \dfrac{h}{2}, y_1^k + \dfrac{h}{2}K_{11}, y_2^k + \dfrac{h}{2}K_{21}, \cdots, y_m^k + \dfrac{h}{2}K_{m1}\right) \\ K_{i3} = f_i\left(x_k + \dfrac{h}{2}, y_1^k + \dfrac{h}{2}K_{12}, y_2^k + \dfrac{h}{2}K_{22}, \cdots, y_m^k + \dfrac{h}{2}K_{m2}\right) \\ \quad \vdots \\ K_{i4} = f_i\left(x_k + h, y_1^k + hK_{13}, y_2^k + hK_{23}, \cdots, y_m^k + hK_{m3}\right) \end{cases} \quad i = 1,2,\cdots,m \tag{3-33}$$

and h is the step size which can be fixed or varied at different steps.

The complete execution steps are summarized in Table 3.1.

Table 3.1. Execution procedures for the 4th-order Runge-Kutta algorithm.

Step 1	Set $k = 0$, and initialize $y_i^0(x_0), i = 1,2,\cdots m$.Then, set step size h.
Step 2	Calculate y_i^{k+1} according to Eq. (3-32) and Eq.(3-33).
Step 3	Update $x_i^{k+1} = x_i^k + h$.
Step 4	Check whether x_i^{k+1} exceeds the stop value of x_i. If the answer is no, set $k = k+1$ and go back to Step2. Otherwise, go to Step 5.
Step 5	Output x_i and its corresponding y_i for all k.

3.4.2. The Numerical Model for Laser Simulation

Figure 3.3 shows the main program for laser simulation purpose.

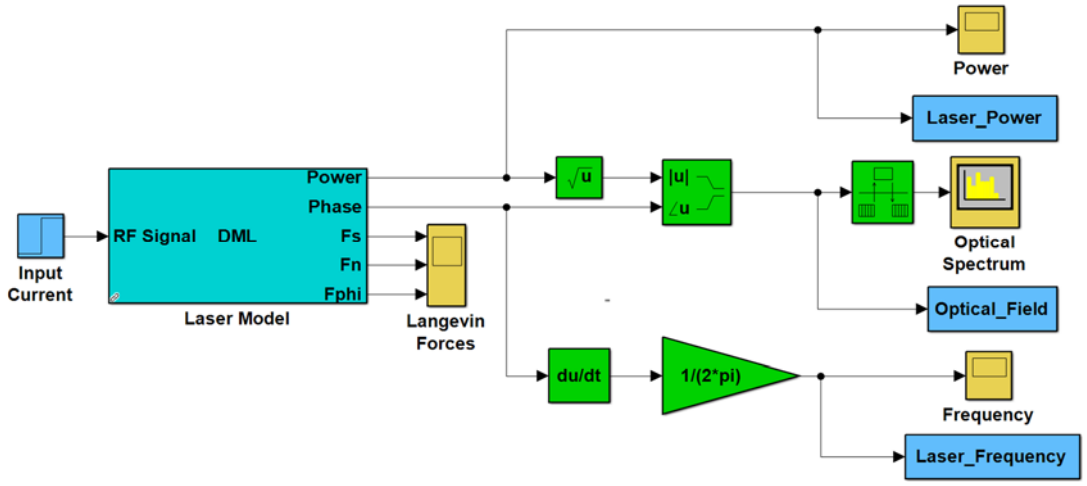

Figure 3.3. The simulation model of semiconductor lasers.

In Figure 3.3, the RF signal modulated onto the DML is set as the input of the model. The model outputs the power and phase of the laser under simulation. F_s, F_n and F_{phi} denote the Langevin forces that are added onto the photon density, carrier density and the phase, respectively. At the end of the DML model outputs, the complex optical field of the laser and the laser frequency are constructed. The optical spectrum is also directly displayed in the model. For the input test signal, it can be set as a standard step signal to reveal the step response of the laser, or a constant to show the steady-state characteristics of the laser. When modulation is needed, the input signal can be set as the time-domain representation of a specific kind of modulation format, such as PAM-4.

Table 3.2. Simulation parameters for the laser rate equation model.

Parameters	Value	Unit
Optical Confinement Factor	0.4	–
Active Layer Gain Coefficient	3×10^{-20}	m^3
Group Velocity	9×10^{7}	$m\cdot s^{-1}$
Phenomenological Gain Compression Factor	3.4×10^{-23}	m^3
Carrier Density at Material Transparency	1×10^{24}	m^{-3}
Spontaneous Emission Coupling Factor	3×10^{-4}	–
Carrier Lifetime	3×10^{-9}	s
Photon Lifetime	1×10^{-12}	s
Active Region's Volume	1×10^{-16}	m^3
Total Differential Quantum Efficiency	0.4	–
Linewidth Enhancement Factor	5	–
Plank Constant	6.624×10^{-34}	$J\cdot s$
Charge Associated with an Electron	1.602×10^{-19}	C

Table 3.2 lists all the essential parameters used in the model shown in Figure 3.3, which are chosen according to typical values of semiconductor lasers [80]. In the real-time simulation, the calculation step is set to be a fixed one with the value of 1 ps so as to have a high enough precision to better describe the laser dynamics.

3.4.3. Simulated Characteristics of the Laser Rate-Equation Model

3.4.3.1. The steady-state solution

To describe the steady-state characteristics of the above laser rate-equation model, we set the first derivatives of carrier and photon densities with respect to t to zero, i.e. $\frac{dS}{dt} = 0$ and $\frac{dN}{dt} = 0$. The calculation result is obtained using the Newton-Raphson numerical method and is shown in Figure 3.4.

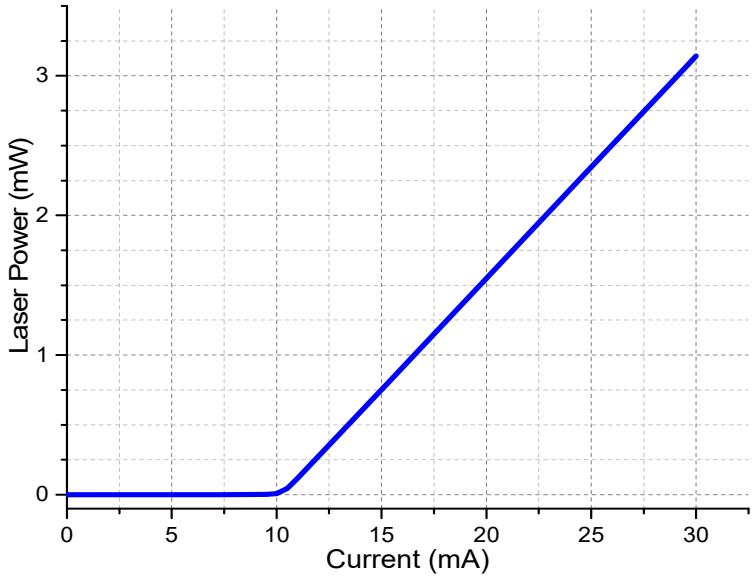

Figure 3.4. Steady-state characteristics of the laser rate-equation model.

From Figure 3.4, we can easily tell the threshold current of this laser model is about 10 mA with the parameters given in Table 3.2. Above the threshold, the laser output power linearly increases with the bias current, at an approximate slope of $0.156\ mW/mA$. Such a steady-state behaviour corresponds to the experimental observations of typical semiconductor lasers.

3.4.3.2. Small-signal response analysis

When the semiconductor laser is biased at a certain current, the small-signal model is an effective approximation to analytically describe the laser dynamics. By linearizing Eq. (3-21) at different steady-state conditions, the analytical forms of the laser small-signal responses can be given as follows.

The small-signal IM response is written as

$$\frac{d}{dt}\begin{bmatrix}\Delta S\\ \Delta N\end{bmatrix}=\begin{bmatrix}\dfrac{\Gamma v_g a_0\left(N_{std}-N_0\right)}{\left(1+\varepsilon S_{std}\right)^2}-\dfrac{1}{\tau_p} & \dfrac{\Gamma v_g a_0 S_{std}}{1+\varepsilon S_{std}}+\dfrac{\Gamma\beta}{\tau_n}\\ -\dfrac{v_g a_0\left(N_{std}-N_0\right)}{\left(1+\varepsilon S_{std}\right)^2} & -\dfrac{v_g a_0 S_{std}}{1+\varepsilon S_{std}}-\dfrac{1}{\tau_n}\end{bmatrix}\begin{bmatrix}\Delta S\\ \Delta N\end{bmatrix}+\begin{bmatrix}0\\ \dfrac{1}{eV_a}\end{bmatrix}\Delta I \tag{3-34}$$

$$\Delta P=\begin{bmatrix}V_a\eta h\upsilon/(2\Gamma\tau_p) & 0\end{bmatrix}\begin{bmatrix}\Delta S\\ \Delta N\end{bmatrix}$$

And the small-signal FM response is expressed as

$$\frac{d}{dt}\begin{bmatrix}\Delta S\\ \Delta N\end{bmatrix}=\begin{bmatrix}\dfrac{\Gamma v_g a_0\left(N_{std}-N_0\right)}{\left(1+\varepsilon S_{std}\right)^2}-\dfrac{1}{\tau_p} & \dfrac{\Gamma v_g a_0 S_{std}}{1+\varepsilon S_{std}}+\dfrac{\Gamma\beta}{\tau_n}\\ -\dfrac{v_g a_0\left(N_{std}-N_0\right)}{\left(1+\varepsilon S_{std}\right)^2} & \dfrac{4\pi}{\alpha\Gamma v_g a_0}\left(-\dfrac{v_g a_0 S_{std}}{1+\varepsilon S_{std}}-\dfrac{1}{\tau_n}\right)\end{bmatrix}\begin{bmatrix}\Delta S\\ \Delta N\end{bmatrix}+\begin{bmatrix}0\\ \dfrac{1}{eV_a}\end{bmatrix}\Delta I \tag{3-35}$$

$$\Delta f=\begin{bmatrix}0 & \dfrac{\alpha\Gamma v_g a_0}{4\pi}\end{bmatrix}\begin{bmatrix}\Delta S\\ \Delta N\end{bmatrix}$$

where S_{std} and N_{std} are the photon density and carrier density at the given steady-state condition, which is calculated using the method in the above section.

From Eq. (3-34) and Eq. (3-35), it can be concluded that either the IM or FM small-signal response falls into the form of a typical second-order system. The relevant frequency response analysis is shown in Figure 3.5.

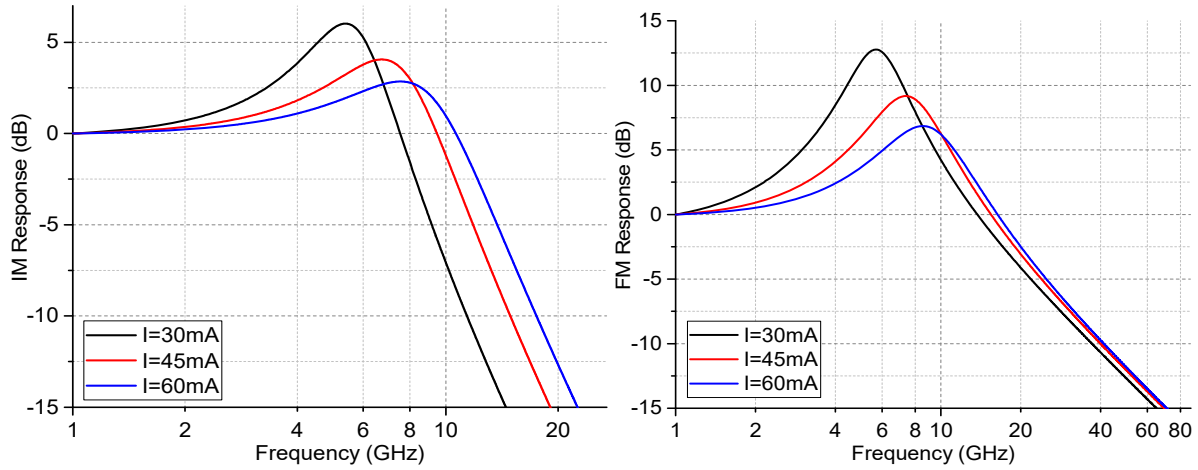

Figure 3.5. The small-signal response of the laser rate-equation model. (a) Intensity modulation; (b) frequency modulation. IM: Intensity modulation; FM: frequency modulation.

Obvious resonance peaks can be observed in Figure 3.5. For IM response, as shown in Figure 3.5 (a), with a growing bias current from 30 mA to 60 mA, the resonant frequency grows from 5.2 GHz to 7.9 GHz and the damping factor of the system also increases. Similar trend is observed in the FM response as shown in Figure 3.5 (b). The existing of a resonance peak predicts the ringing behaviour of the step response of the laser. The examination under step

input signal is essential, since for the non-return to zero (NRZ) modulation format, the rising and falling edge of each symbol resembles the standard step signal. However, in reality, only considering the small-signal response is not enough, because the RF signal change between two levels can normally reach tens of miliamperes. Therefore, it is much more useful to perform the large-signal response analysis.

3.4.3.3. Large-signal analysis

Applying the 4th-order Runge-Kutta solver engine in Simulink®, large-signal responses of the proposed laser rate-equation model can be calculated in real time. The following figure illustrates the dynamics of the laser power and frequency, where a bias voltage of 60 mA and a step current input of 10 mA are applied to the model.

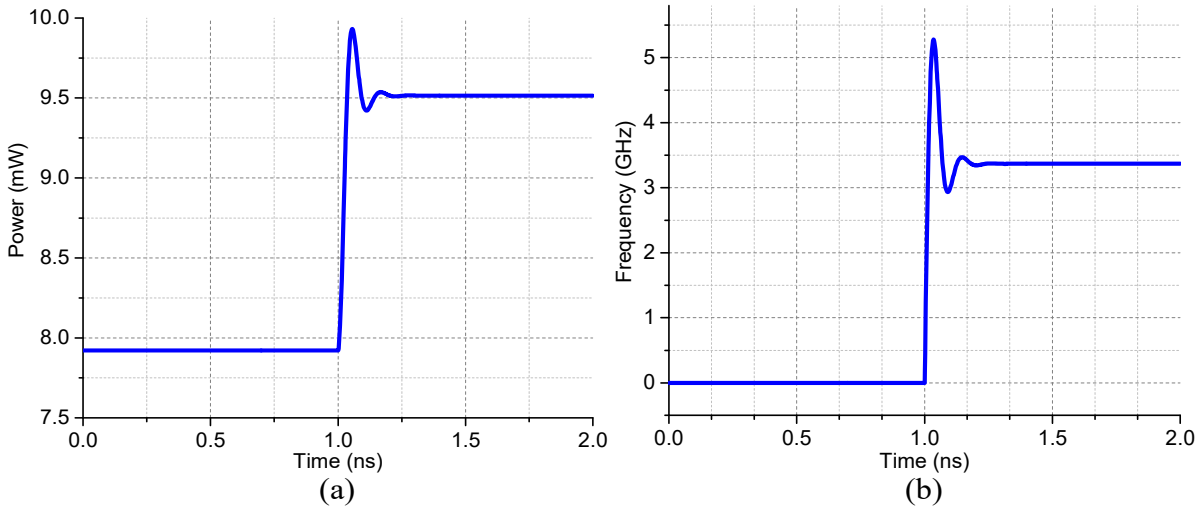

Figure 3.6. The large-signal response of the laser rate-equation model. (a) Intensity modulation; (b) frequency modulation.

In Figure 3.6, both intensity response and frequency response show obvious ringing effects. For the output power, a 1.6-mW power increase between the two steady states with a rising time of 0.04 ns and an overshoot about 3.7% is shown. As for the large-signal FM response, an approximate 3.4-GHz frequency shift with a rising time of 0.03 ns and an overshoot as large as about 55% is observed clearly under a 10-mA input current increase.

3.4.3.4. Noises inside the laser active region

Employing Eq. (3-27), where the Langevin forces are included in the laser model, the intensity noise and phase noise inside the laser active region are simulated. With a constant bias current at 60 mA, the simulation is carried out leading to the following results.

From Figure 3.7, a peak at about 8 GHz is observed for the cases both with and without the nonlinear coefficient, showing the deviation of the line shape from the typical Lorentzian shape. It is well known that the laser phase noise can be modelled by a Wiener process generating the Lorentzian line shape which has been verified experimentally in ECLs. The red line shown in the figure is obtained based on the Wiener process noise model, which exhibits a typical

Lorentzian line shape. However, the above results show a non-Lorentzian line shape in the power spectrum density of the DML. Such a deviation may have non-negligible impacts on the phase recovery algorithms, and furthermore affects the overall performance of the entire transmission system. Figure 3.7 also reveals the effect of nonlinear coefficient ε in the rate equations. With a higher value of ε, the damping effect becomes severer.

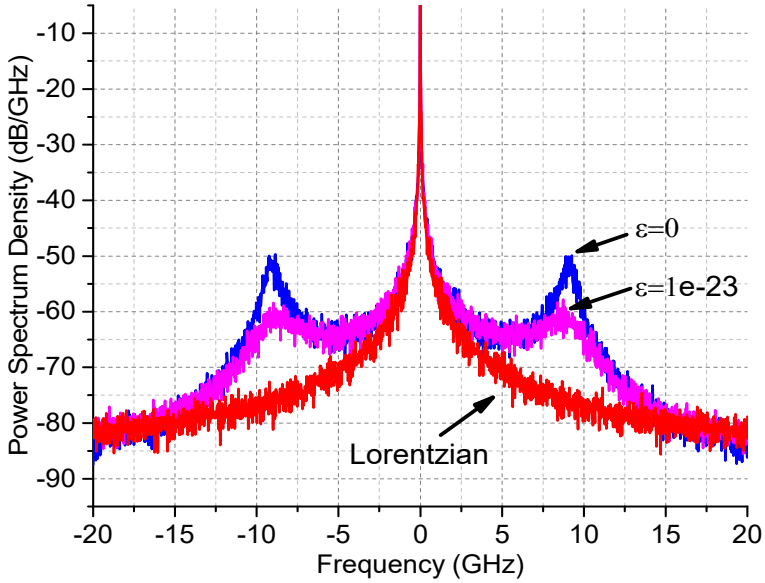

Figure 3.7. Power spectrum density of the laser rate equation model with noises. (ε is the nonlinear coefficient in Eq. (3-27)).

The relative intensity noise (RIN) and the frequency noise (FN) are easily evaluated using $\Delta P = P - \overline{P}$ and Δf, respectively. The spectra of the RIN and FN can be obtained by performing the Fourier transform of the auto-correlation functions of ΔP and Δf.

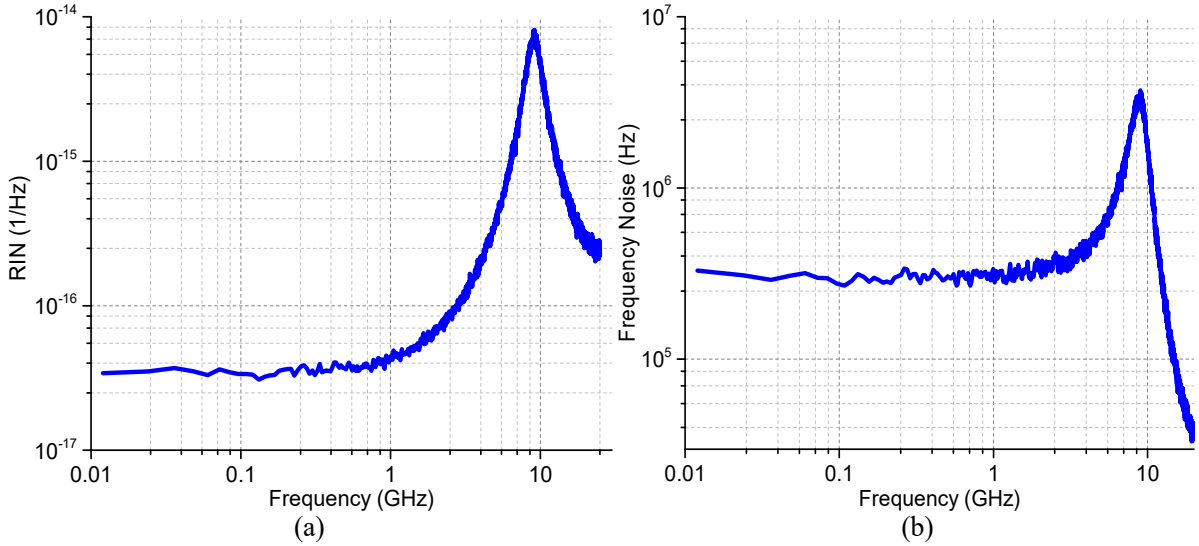

Figure 3.8. Simulated laser noise spectra. (a) RIN noise; (b) frequency noise.

Figure 3.8 shows the calculation results at $\varepsilon = 1\times10^{-23}$ with the same bias current of 60 mA. On both spectra, we can see a clearly shown peak at about 10 GHz, explaining the deviation from the Lorentzian line shape in Figure 3.7. The laser linewidth can be determined from the low frequency component of the FN spectrum, using the well-known relation given by $\Delta f = 4\pi \cdot FN|_{\omega=0}$. For this particular model, the laser linewidth is about 3.8 MHz, which is a reasonable value for typical DMLs.

3.4.3.5. Large-signal modulation behaviour

In this section, the behaviour of the laser rate-equation model under RF signal modulation is examined. The RF signal applied is a standard NRZ signal and is assumed to have the following shape [78]

$$I_p = \begin{cases} 0 & t < 0 \\ I_m\left[1-\exp\left(-t^2/\tau_r^2\right)\right] & 0 \le t \le T \\ I_m\left[1-\exp\left(-T^2/\tau_r^2\right)\right]\cdot\exp\left(-t^2/\tau_r^2\right) & t > T \end{cases} \quad (3\text{-}36)$$

where I_m is the peak modulation current, τ_r determines the pulse rise time or fall time and T is the bit period.

A 2-Gb/s NRZ signal with a peak-to-peak current of 20 mA is added onto the laser rate-equation model in the simulation with $\tau_r = 0.05\ ns$. The laser is still biased at 60 mA. In Figure 3.9 (a) and (b), the time-domain RF and optical signal outputs from the DML are shown for the first 3 ns.

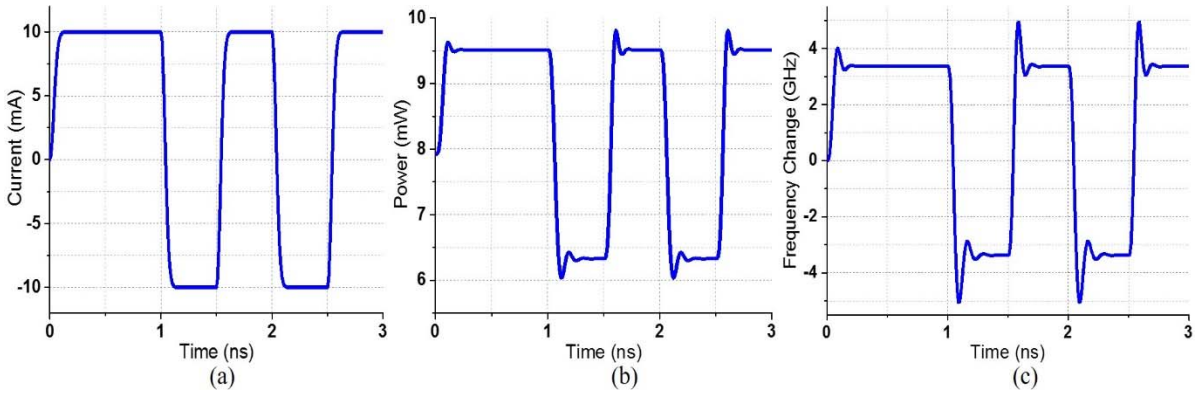

Figure 3.9. Large-signal modulation dynamics of the laser rate-equation model. (a) RF modulation current; (b) laser intensity response; (c) frequency chirp.

Figure 3.9 (b) shows the transient response of the laser output power. The ringing effect which is similar to the laser large-signal response under step input signal can be observed (see Figure 3.6 (a)). The average optical power is about 7.9 mW, which is the value under the 60-mA bias current. Besides, with a 10-mA input current increase, an approximate 1.6-mW output power change at steady-state condition is observed. In Figure 3.9 (c), the dynamics of the FM response

of the simulated laser is illustrated. A 3.4-GHz frequency shift is shown originated from the 10-mA input current change with clear ringing effects in the transient process.

Due to such FM effects, as shown in Figure 3.9 (c), the spectrum of the laser output optical field is largely broadened compared with that of the driving RF signal.

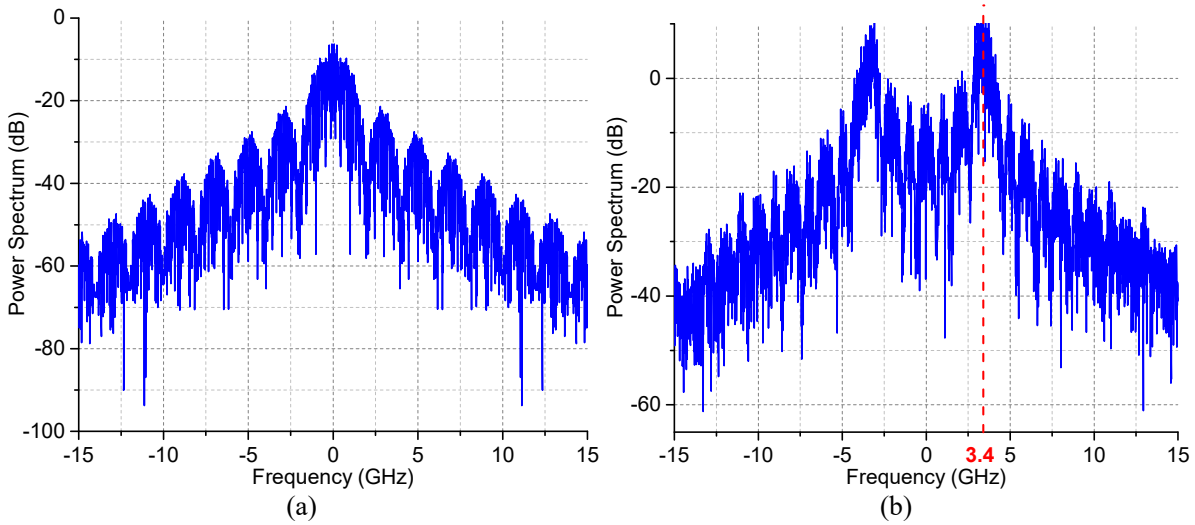

Figure 3.10. Spectra of the driving RF signal and the output of the laser rate-equation model. (a) RF signal spectrum; (b) laser model output signal spectrum.

Compared with Figure 3.10 (a), in Figure 3.10 (b), the signal spectrum is shifted by approximately 3.4 GHz, which corresponds to the result shown in Figure 3.9 (c). It is not difficult to analyse the simplest NRZ signal, but for more complicated modulation formats, the spectrum of output optical field becomes difficult to obtain an intuitive interpretation. Nevertheless, from the above results, it is straightforward to draw the conclusion that the spectrum broadening effect of the modulated DML is inevitable due to the intrinsic laser frequency chirp. Therefore, it is an important issue to be considered in optical transmission systems, which not only makes the optical signal more vulnerable to CD, but also poses much more pressure on the receiver bandwidth. The strengthened CD-induced signal impairments severely limit the transmission distance. And the extra bandwidth requirement at the receiver can largely increase the cost of the whole optical transmission system. These two issues will be further discussed in chapter 4.

Finally, it is worth mentioning that although we have used typical laser parameters in all of the above simulations, the extraction of these parameter values through experiments is not that straightforward and thus, appropriate laser characterization methods should be carefully investigated. Most of these approaches are commonly started from a series of measurements of laser threshold current, output power, small-signal resonance frequency and damping factor. Some of the laser parameters can be calculated directly from these measurements and the rest can only be obtained through a guess-and-optimize procedure. The optimization process is aimed to find the most probable set of parameters [81]. Despite the high computational

complexity, the advantage of this method is its exclusion of the influence of mounting fixture or packaging of the laser diode and has been widely employed for laser characterization.

To conclude, the laser simulation model we have developed so far, is totally based on the classical single-mode laser rate equation. It not only includes the basic dynamics of the laser active region, but also takes the nonlinear effects and noise sources into consideration. However, there are still plenty of other effects that are less important to be included in the above rate-equation model, such as the parasite parameters due to the package of the laser diode, the thermal FM effect that is generated by the injection current induced temperature changes, etc. The overall impact of parasite parameters can be regarded as a low pass filter exerting on the output optical field. As for the thermal FM effect, it will be thoroughly analysed in the next section. Nevertheless, our proposed laser rate-equation model is already sufficient and accurate enough to describe both the steady-state performance and the dynamic characteristics of a typical DML, which can be further applied to systematic simulation of any DML-based optical transmission system.

3.5. THERMAL FREQUENCY MODULATION OF DML

3.5.1. Theory of Thermal Frequency Modulation in DML

Frequency modulation (FM) of the laser diode has been studied for more than three decades. The relation between the input current and frequency change of the laser is more complicated than the current-power relation. There are two major FM effects: (i) the carrier induced FM, due to the carrier density change inside the laser diode, which directly determines the variation of refractive index of the laser active region and (ii) thermal FM, stemming from the temperature changes caused by the heating effect of the injection current. The carrier induced FM can be fully characterized using the standard rate equations and ignoring the third spontaneous emission term which is insignificant under most circumstances, the carrier induced FM is conveniently characterized using the following equation [82]

$$\Delta f = \frac{\alpha}{4\pi}\left(\frac{d}{dt}\ln\left(\mathrm{P(t)}\right) + \kappa\,\mathrm{P(t)}\right) \tag{3-37}$$

where α is the linewidth enhancement factor and κ is the adiabatic chirp coefficient given by $\kappa = 2\Gamma\varepsilon/V_a\eta h\nu$.The detailed properties of the carrier induced FM have been investigated and a precise characterization of the FM response of this kind has been described [82]. However, the laser rate equation (see Eq. (3-27)) does not capture the thermal FM, which needs to be considered separately. It can be expressed by [83]

$$\frac{1}{f}\frac{df}{dT} = \frac{-1}{L}\frac{dL}{dT} - \frac{1}{n}\frac{dn}{dT} \tag{3-38}$$

where f is the laser frequency, L is the cavity length, n is the refractive index of the active region and T is the temperature of the active region. The thermal FM has long been considered to be a slow effect that contributes to the total FM response at a modulation frequency around

10 MHz [84]. However, time constants in the range of 10 to 20 ns have also been reported [84]. Eq. (3-38) is typically used for analytical calculations. For experimental use, a semi-empirical model was given to describe the thermal FM by using the summation of multiple time constants in the following form [84]

$$\Delta f_1(\mathrm{t}) = -\Delta f_0(\mathrm{t}) = \sum_{n=1}^{N} c_n \tanh\left(-\frac{t}{2\tau_n}\right) \tag{3-39}$$

where Δf_1 and Δf_0 represent the frequency change within high power level bit and low power level bit, respectively. Therefore, the total FM can be described using the following equation

$$\Delta f \approx \frac{\alpha}{4\pi}\left(\frac{d}{dt}\ln\left(\mathrm{P(t)}\right) + \kappa \mathrm{P(t)}\right) \pm \sum_{n=1}^{N} c_n \tanh\left(-\frac{t}{2\tau_n}\right) \tag{3-40}$$

where $\pm$ is determined by the power level of the symbol under consideration.

The measurement of the thermal FM characteristics of the DML with a 3-dB bandwidth of 10 GHz is carried out and we report the observation of a 7.5-ns time constant.

3.5.2. Experiment Setup for Characterization of the Thermal FM in a DML

Conventionally, phase responses of an optical component are measured by the modulation phase shift method [85], or the interferometric method [86]. However, these methods normally require suppression of mechanical vibrations and temperature fluctuations. In [87], the DSP-based coherent detection method has been shown to characterize passive optical components with sub-MHz resolution utilizing OFDM signals.

In our experiment, we use digital coherent detection to directly measure this frequency change, which is obviously more accurate than the previous interferometric method [84]. Additionally, coherent detection is capable of recovering the full optical field, which greatly facilities the subsequent signal processing on the detected signal.

The experiment setup is shown in Figure 3.11.

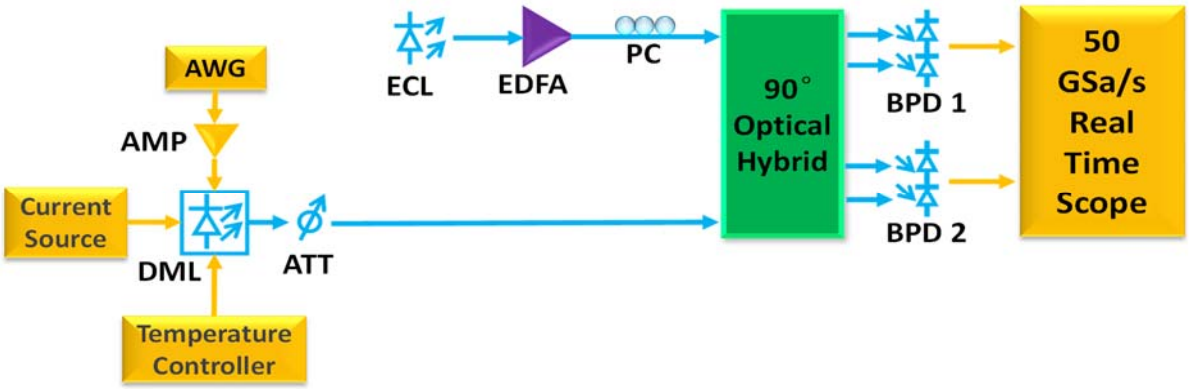

Figure 3.11. Experiment setup for thermal frequency modulation measurement. AWG: Arbitrary waveform generator; AMP: RF amplifier; DML: directly modulated laser; ATT: optical attenuator; PC: polarization controller; ECL: external cavity laser; EDFA: erbium-doped fibre amplifier; BPD: balanced photodetector.

The DML used in the experiment is an InGaAsP/InP multiple-quantum-well distributed-feedback (MQW-DFB) laser from GOOCH & HOUSEGO™. The laser module is in standard 7-pin butterfly package containing a thermoelectric cooler (TEC), thermistor, back facet monitor detector, and bias tee. The laser diode is biased at 70 mA by a constant current source and lases near 1550-nm wavelength. A temperature controller is connected to the DML. Monitored by the built-in thermistor and controlled through its inner TEC, the temperature of the laser diode is stabilized at 24.5℃. At the output end of the DML, an optical attenuator is attached to limit the average output power at 10 dBm. Square-wave RF signals at different repetition frequencies are first generated by an arbitrary waveform generator (AWG) with V_{pp} of 1 V and then amplified by a 19-dB RF amplifier. At the receiver end, an ECL with 10-kHz linewidth and 4-dBm output power is used as LO. The DML output optical field is then mixed with LO inside the 90° optical hybrid followed by two pairs of 43-GHz BPDs. A Tektronix® real-time scope with an electrical bandwidth of 16 GHz is run at 50 GSa/s. Afterwards, offline DSP is carried out in MATLAB® to calculate the amplitude and phase of the received signals. After frequency offset compensation, a Bessel digital filter is used to filter out the noise. Finally, the phase difference between every two sampling points is generated, which can then be further processed to represent the frequency change. This above process is repeated for varying modulation frequencies from 80 MHz to 1 GHz.

3.5.3. Results and Discussions

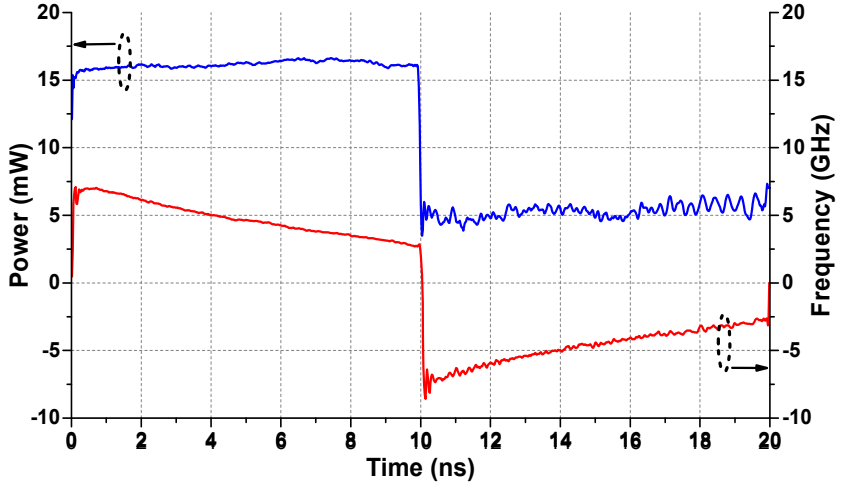

Figure 3.12. Signal power and frequency modulation at 100 MHz.

From Eq. (3-37), it is obvious that without thermal FM, as long as the symbol period is long enough, the frequency change of the laser between two symbols of different power levels will stabilize at a certain value after an initial transient. Therefore, the frequency drift effect shown in Figure 3.12 can only be explained by the thermal FM of the DML. Using Eq. (3-39), we characterize the thermally-induced frequency drift, and obtain excellent agreement between the measurement and the theoretical equation at both low and high frequencies. This again confirms that the frequency drift we observe is originated from thermal FM. Since our testing is

performed at relatively high frequencies, well beyond 10 MHz that is typically used in such measurement [84], the fitting gives only one time constant. The thermal FM Δf_T is given by

$$\Delta f_T(\mathrm{t}) = 7.8\tanh\left(-\frac{t}{15ns}\right) \tag{3-41}$$

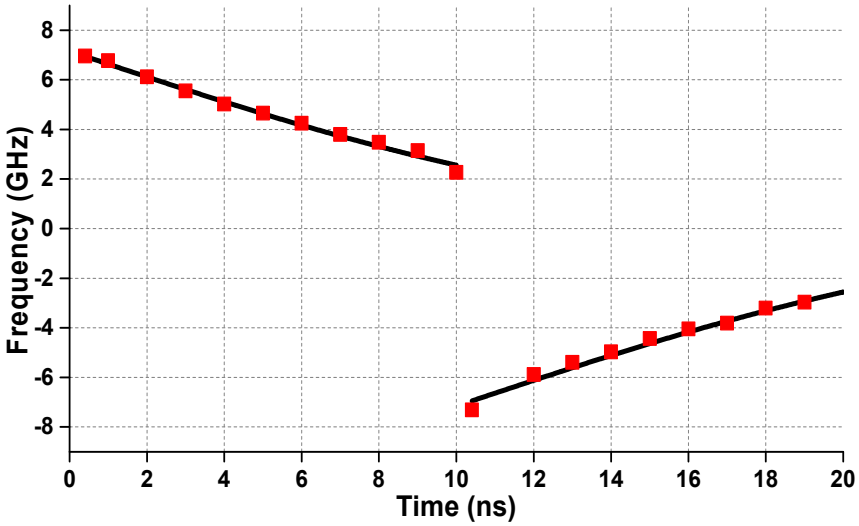

Figure 3.13. Dynamic frequency change of the DML due to thermal FM. Square dots are the experiment results, and solid lines are the curve fits using Eq. (3-39).

Figure 3.13 shows the measured frequency modulation at 100 MHz modulation frequency and corresponding curve fit with Eq. (3-41).This gives a time constant of 7.5 ns for the thermal FM effect. A time constant of the frequency change in this scale can have significant impact when the frequency or phase modulation of DML is utilized in directly modulated and coherently detected systems [16].

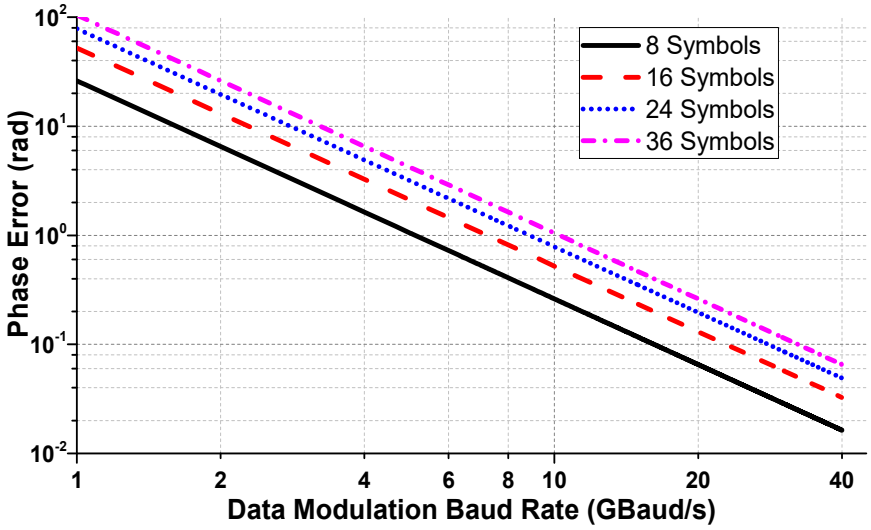

Figure 3.14. Phase change estimation at different modulation frequencies. The legend shows varying frequency/phase estimation window length.

In direct modulated and coherent detected systems, the phase change within one symbol length is one important quantity [16], it is instructive to analyse the impact of the thermal FM effect on this phase change quantity. The phase error $\Delta\varphi$ per symbol would be due to the thermal FM effect and is expressed as

$$\Delta\varphi = 2\pi \cdot \Delta f \cdot T \tag{3-42}$$

where Δf is the thermal frequency drift which can be calculated by using Eq. (3-41), T is the symbol length. The time t in Eq. (3-41) is equal to the length of phase/frequency estimation window. Figure 3.14 shows the phase error at baud rate of 1 to 40 GBaud/s when a DML is used for complex data modulation. It can be seen that with the decrease of baud rate, the phase drift becomes larger. It is unlikely to modulate the DML at very low frequency in optical communication. However, Figure 3.14 reveals that even at a high baud rate of 10 GBaud, the phase error can be sufficiently large to cause the smearing of constellation points. Consequently, when frequency or phase modulation of DML is utilized in coherently detected systems, the impact of such fast frequency change will dramatically increase the phase error, and thus should be compensated accordingly.

3.6. **CONCLUSIONS**

In this chapter, we first explained the basic principles of a semiconductor laser and showed the derivation of the single-mode laser rate equation. Based on the laser rate equation, a simulation model was further developed and we demonstrated several major characteristics of the semiconductor laser diode. Finally, we characterized the thermal FM properties of a directly modulated DFB laser using DSP facilitated optical coherent detection. We observed a relatively fast thermal effect of the frequency change and also identified the possible impacts of such a fast effect on optical communication systems.

Chapter 4
The Complex-Modulated Directly Modulated Laser

4.1. INTRODUCTION

Over the past decade, the DML-based short-to-medium reach optical communication system has been extensively explored. Recent reports have demonstrated high-capacity optical links for 100 Gb/s and beyond with different advanced modulation formats and various multiplexing techniques [5-12,88,89]. However, at a higher data rate, for ordinary DMLs, the intrinsic frequency chirp becomes increasingly detrimental due to a largely broadened optical spectrum. For specially designed DMLs, such as the transverse-coupled-cavity vertical-cavity surface-emitting laser (TCC-VCSEL) [20], the laser modulation bandwidth can be achieved with reduced frequency chirp, but the increased RF signal bandwidth itself still broadens the optical spectrum. In either case, DML-based systems suffer both a severer inter-symbol interference and an increasing CD which is difficult to mitigate with the square-law direct detection. In order to overcome the CD-induced impairments, inverse-dispersion fibre [13], optical injection locking [14], and optical filter [15] have been proposed. However, these methods always require extra devices, increasing both complexity and cost, and are thus not desirable for the cost-sensitive short-reach optical links that is within a few hundreds of kilometres. As the DSP facilitated coherent detection can easily compensate large amount of CD, its superiority over traditional direct detection systems has been shown in DML-based short-reach optical communication systems [11,12].

Despite the successful application of coherent receivers, compared with the classical systems using $LiNbO_3$-based external modulators and complex modulation formats such as QAM, DML-based systems with PAM formats still have a rather large OSNR sensitivity disadvantage. In [12], efforts have been made to improve the OSNR sensitivity of such DML-based coherent systems. By adding an optical filter to realize frequency-to-amplitude modulation (FM-to-AM) conversion, a 2-dB OSNR sensitivity improvement is achieved in a polarization multiplexed PAM-4 system. However, the work in [11] and [12] only focuses on the IM of the DML, where the frequency chirp has been considered as a source of signal distortion and thus a limitation on

the overall system performance. We propose a novel modulation scheme, which is called CM-DML. By utilizing both the intensity and phase modulation with optical coherent detection and carefully estimating the DML chirp parameters, we show a considerable OSNR sensitivity enhancement.

It is true that the frequency chirp provides another modulation dimension and gives dramatic performance improvement. However, it inevitably broadens the optical spectrum and subsequently requires higher receiver bandwidth. It is thus desirable to constrain the electrical bandwidth requirement for CM-DML systems to maintain the low cost for the receiver. We perform a systematic study of the impact of receiver filtering effects on the performance of CM-DML systems with a conclusion that CM-DML can be implemented using cost-effective receiver subsystem without need for excessive receiver bandwidth.

In this chapter, we first give a detailed introduction to the basic principles of CM-DML systems, followed by a thorough simulation-based analysis. Then, we experimentally demonstrate the capability of the CM-DML system to deliver 10-GBaud dual-polarization PAM-4 signal over 1200-km SSMF on a 10-GHz DML. By increasing the order of the PAM modulation format, we successfully transmitted 10-GBaud dual-polarization PAM-8 signal over 320-km SSMF, reaching a record RF spectral efficiency of 6-bit/s/Hz. Utilizing 16-GHz DMLs, we push the link data rate to 100 Gb/s and show the successful transmission of PAM-4 signal over 1600-km SSMF with a BER under 20% FEC threshold. Finally, by introducing a digital filter at the receiver side, we show that for 1-dB OSNR penalty at 20% FEC, the required electrical bandwidth is 7.5 GHz for 10-GBaud PAM-4 CM-DML systems.

4.2. THEORY OF THE COMPLEX-MODULATED DML

4.2.1. Introduction to Basic Concepts of CM-DML

As discussed in section 3.2.3, the predominant frequency chirp of a semiconductor laser is an intrinsic phenomenon originated from the refractive index change of the laser active region, which is known as the carrier-induced FM. In [90], it has been pointed out that the frequency chirp can be directly expressed using the output power of the laser, which has already been shown in Eq. (3-37). We rewrite it as follows

$$\Delta f = \frac{\alpha}{4\pi}\left(\frac{d}{dt}\ln\left(\mathrm{P(t)}\right)+\kappa\,\mathrm{P(t)}\right) \tag{4-1}$$

where $P(t)$ is the output power of the laser, α is the linewidth enhancement factor, and κ is the adiabatic chirp coefficient. Here we assume $P(t)$ is varying slowly with time. By integrating between two sampling points t_1 and t_2 spaced at a symbol period T, we arrive at the differential phase of

$$\Delta\varphi = 2\pi\int_{t_1}^{t_2}\Delta f\cdot dt \approx \frac{\alpha}{2}\left(\ln\frac{P(t_2)}{P(t_1)}+\kappa\frac{P(t_2)+P(t_1)}{2}T\right) \tag{4-2}$$

Eq. (4-2) gives the explicit expression of the phase difference between the two transmitted symbols. Then, we can define the phase at time t as

$$\psi(t) = \frac{\alpha}{2}\left(\ln P(t) - \kappa \frac{P(t)}{2} T\right) \tag{4-3}$$

Thus, the phase for the symbol at t_2 can be represented by

$$\theta(t_2) = \Delta\varphi + \psi(t_1) = \Delta\varphi + \frac{\alpha}{2}\left(\ln P(t_1) - \kappa \frac{P(t_1)}{2} T\right) \tag{4-4}$$

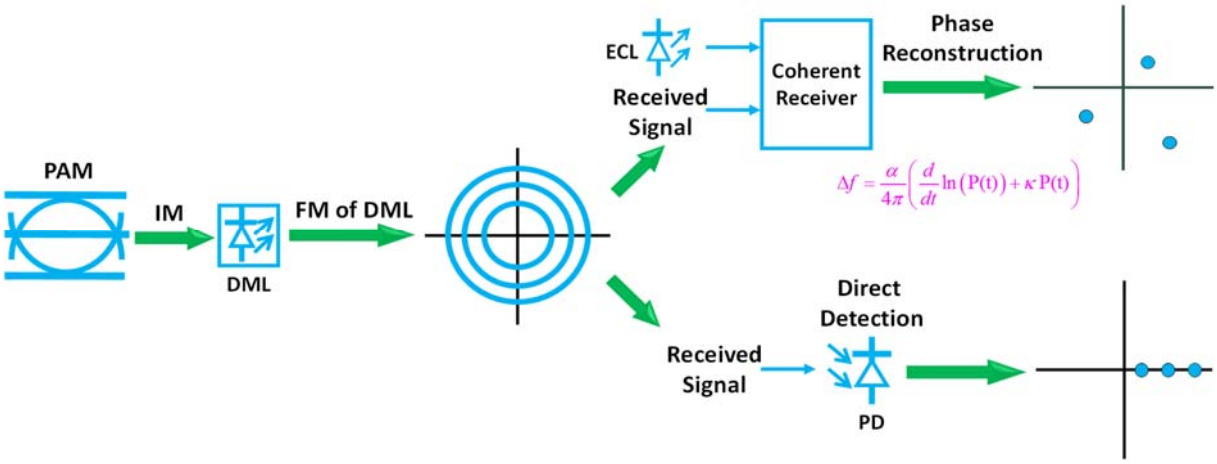

Figure 4.1. Illustration of the basic principles of a CM-DML system. PAM: Pulse amplitude modulation; IM: intensity modulation; FM: frequency modulation; ECL: external cavity laser; PD: photodetector.

In Figure 4.1, by taking a PAM-3 signal as an example, we show the concepts of a CM-DML system and comparison with the conventional direct detection approach. After one-dimensional baseband PAM-3 signal is loaded onto the DML through intensity modulation, not only the laser output power changes, but there is also an extra frequency shift added onto the optical field (see Eq. (4-1)) due to the FM of the DML. Such FM effect gives rise to the circular rotation of the constellation points. At the receiver side, we illustrate two different detection methods. The conventional direct detection scheme is shown in the lower branch of Figure 4.1, where only the intensity of the received optical signal is recovered and the phase of the signal is omitted. Thus, the recovered constellation is still one-dimensional. In contrast, the optical coherent detection scheme is shown in the upper branch of Figure 4.1, where a standard dual-polarization receiver is employed with a high wavelength precision and low phase noise ECL as the LO. Such a coherent receiver can recover both the power and phase of the received signal which is further processed through offline DSP. First, the measured phase difference between two adjacent symbols can be directly obtained by simple subtraction. Second, using the received signal power, the estimated phase difference between the symbols can be calculated according to Eq. (4-2). Laser parameters α and κ used for the above phase estimation procedure are obtained by sending pilot symbols prior to data transmission and can be easily recalibrated

through our proposed estimation algorithm. Finally, the constellation points as shown can be reconstructed based on Eq. (4-4).

Figure 4.1 clearly shows the advantage of CM-DML approach over the conventional direct detection scheme. From the final recovered constellation graphs, we can see that for CM-DML systems, the Euler distance between the two adjacent points is much larger than that in the direct detection method. It is well known that sufficient spacing among the constellation points make modulation formats such as 4-QAM and QPSK have the best OSNR sensitivity. Therefore, compared with direct detection, in theory, we can expect a significant OSNR sensitivity enhancement for our proposed CM-DML scheme.

In an early attempt to implementing the CM-DML system [91], the symbol decision procedure is performed by simply calculating the Euler distances between the theoretically calculated point positions in the constellation (see Eq. (4-4)) and the measured point positions. With such symbol decision approach, a 6-dB OSNR sensitivity improvement is achieved at 7% FEC threshold. A more effective algorithm can be designed by noticing the existence of a 2-tap memory in Eq. (4-2). The received data can thus be modelled as a Markov chain process, where the Viterbi algorithm can be employed for the symbol decision procedure, which will be further discussed in the following section. In either case, we omit the thermal frequency modulation of DML as discussed in chapter 3, since the minimum baud rate we used in all the following experiments is 10-GBaud/s, resulting in an insignificant phase error for each symbol.

4.2.2. Introduction to Dynamic Programming

In the realm of telecommunication, the Viterbi algorithm is widely employed as a decoding algorithm for convolutional codes in noisy digital communication channels and has been supported on hardware such as commercial DSP chips. As an effective symbol decision algorithm, the Viterbi algorithm has already become a standard module in various commercial receiver optical sub-assemblies (ROSAs) to better equalize the transmission impairments and is also known as maximum likelihood sequence estimation (or MLSE). In essence, the Viterbi algorithm is a special type of DP algorithm.

The term dynamic programming is first introduced by Richard Bellman in the 1940s and is concluded in the famous Bellman equation. DP is a general method used to efficiently solve a complex problem by breaking down it into multiple sub-problems. The sub-problems are solved and the results are stored into a data structure so that when the same sub-problem occurs again, the results can be readily obtained without solving it again. Such a technique is normally called "memoization" and is aimed to largely reduce the time complexity of an algorithm in expense of a moderate storage space. DP-based algorithms have been widely adopted in many different fields, including mathematics, computer science, control theory, economy, etc., and are more often used for optimization problems. In a general optimization problem, a criterion is usually set as the total cost of each possible solution to the problem. The criterion has many different names such as cost function in computer science and control theory, effectiveness function in economy and management science. In the following sections, we first introduce the principles

of solving an optimization problem through DP. Then, the Viterbi algorithm used for symbol decision in telecommunication systems can be naturally derived. For convenience of description, we first define several terms as follows.

Stage. The first step in DP is decomposing a complex problem into discrete inter-connected sub-problems which are called stages. Thus, the whole problem is topologically sorted based on the decomposing method so that the DP algorithm can work along a certain sequence of stages. Finding such a chain of stages may sometimes be natural and become very difficult under other circumstances. Whether a problem is broken down reasonably or not determines the computational complexity of DP. We use S_k to denote the k-th stage.

State. State defines the initial conditions at the starting point of each stage. The variables used to describe the state are called state variables, denoted as C_i. Thus, we can express the state of the k-th stage as $S_k = \{C_1, C_2, \dots, C_M\}$. It is desirable for the stage sequence to have the property that given S_k, all states after S_k are conditionally independent from any state before S_k, which is called the Markov property. In the following discussion, we assume that all the problems are carefully decomposed to own the Markov property.

Decision. At a given stage, the decision set means all the possible operations that can be taken to determine the state of next stage. We use $u_k(S_k)$ to represent a certain operation at stage S_k and the decision set is expressed as $D_k(S_k)$.

Strategy. We call a strategy as the set of the sequential decision chain from stage S_k to the final stage S_N, expressed by $p_{k,N}(S_k) = \{u_k(S_k), u_{k+1}(S_{k+1}), \dots, u_N(S_N)\}$. When $k = 1$, we have a strategy of the whole problem $p_{1,N}(S_1) = \{u_1(S_1), u_2(S_2), \dots, u_N(S_N)\}$. All possible strategies for the entire stage sequence are formed as a set, denoted as P.

State Transition Equation. Given a certain decision $u_k(S_k)$, the state of next stage S_{k+1} is determined through an evolution equation called the state transition equation. Such a deterministic relationship is expressed as $S_{k+1} = T_k(S_k, u_k)$, where T_k is called the state transition function.

Cost Function. To evaluate the overall performance of a certain strategy $p_{k,N}$, some kind of criterion needs to be defined which is called the criterion function. We use $V_{k,N} = V_{k,N}(S_k, u_k, S_{k+1}, \dots, S_N)$ to represent the criterion function. It is always required that $V_{k,N}$ is separable, i.e. $V_{k,N}(S_k, u_k, S_{k+1}, \dots, S_N) = \Psi_k\left(S_k, u_k, V_{k+1,N}(S_{k+1}, \dots, S_N)\right)$, where Ψ_k is a strictly monotonic deterministic function with respect to N. Furthermore, we can define the cost function as the optimal value of the criterion function among all possible strategies, i.e. $f_k(S_k) = opt_{\{u_k,\dots,u_N\}} V_{k,N}$.

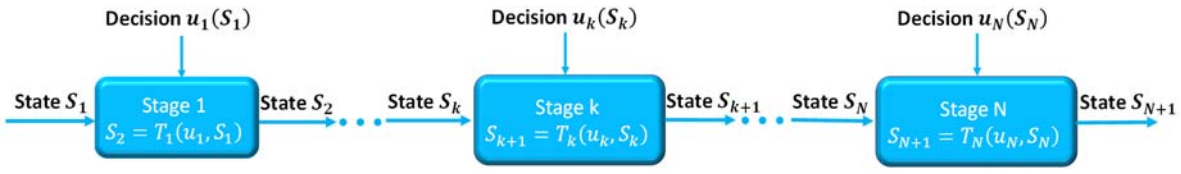

Figure 4.2. Formation of a typical dynamic programming problem.

We conclude the working flow of a DP algorithm in Figure 4.2 using the above definitions.

The execution of DP can be performed from either side of the stage sequence. We first consider the backward evolving direction with the criterion function defined by summation

$$V_{k,N} = \sum_{j=k}^{N} v_j\left(S_j, u_j\right) \tag{4-5}$$

where $v_j(S_j, u_j)$ denotes the criterion function at stage j. We can rewrite Eq. (4-5) in a recursive form as

$$V_{k,N}\left(S_k, p_{k,N}\right) = v_k\left(S_k, u_k\right) + V_{k+1,N}\left(S_{k+1}, p_{k+1,N}\right) \tag{4-6}$$

Therefore, we can write the cost function $f_k(S_k) = opt_{\{u_k,\ldots,u_N\}} V_{k,N}$ as

$$\begin{aligned} f_k\left(S_k\right) &= \underset{p_{k,N}}{opt}\, V_{k,N}\left(S_k, p_{k,N}\left(S_k\right)\right) \\ &= \underset{\{u_k, p_{k+1,\mathrm{N}}\}}{opt}\left\{v_k\left(S_k, u_k\right) + V_{k+1,N}\left(S_{k+1}, p_{k+1,N}\right)\right\} \\ &= \underset{u_k}{opt}\left\{v_k\left(S_k, u_k\right) + \underset{p_{k+1,N}}{opt}\, V_{k+1,N}\right\} \\ &= \underset{u_k \in D_k(S_k)}{opt}\left\{v_k\left(S_k, u_k\right) + f_{k+1}\left(S_{k+1}\right)\right\} \end{aligned} \tag{4-7}$$

with the border condition $f_{N+1}(S_{N+1}) = 0$.

Similarly, for the forward evolving direction, we have

$$f_k\left(S_{k+1}\right) = \underset{u_k \in D_k^r(S_{k+1})}{opt}\left\{v_k\left(S_{k+1}, u_k\right) + f_{k-1}\left(S_k\right)\right\} \tag{4-8}$$

where $D_k^r(S_{k+1})$ is the decision set determined by S_{k+1} instead of S_k. And the border condition is $f_0(S_1) = 0$.

Under the criterion function Eq. (4-5), Eq. (4-7) and Eq. (4-8) are called the fundamental equations for DP which recursively describes the entire solving procedure. For other criterion functions, it is not hard to get similar equations and the DP algorithm can be implemented based on the fundamental equation.

The Optimality Theorem. For a multi-stage optimization problem with N stages numbered by $k = 1,2,\ldots,N$. The allowable strategy $p_{1,N}^* = \{u_1^*, u_2^*, \ldots, u_N^*\}$ is the optimal strategy, if and only if, for $\forall\, k, 1 < k <$ N and initial state S_1, the following equation holds

$$V_{1,N}\left(S_1, p_{1,N}^*\right) = \underset{p_{1,N} \in p_{1,N}(S_1)}{opt}\left\{V_{1,N}\left(S_1, p_{1,N}\right) + \underset{p_{\mathrm{k},N} \in p_{\mathrm{k},N}\left(\tilde{S}_k\right)}{opt}\, V_{k,N}\left(\tilde{S}_k, p_{k,N-1}\right)\right\} \tag{4-9}$$

where $p_{1,N} = \left(p_{1,k-1}, p_{k,N}\right)$, and $\tilde{S}_k = T_{k-1}(S_{k-1}, u_{k-1})$ is the state determined by S_1 and $p_{1,N}$. Eq. (4-9) is also called the Bellman equation.

Corollary. Suppose $p_{1,N}^*$ is the optimal strategy. Then, for $\forall\, k, 1 < k <$ N, $p_{k,N}^*$ is the optimal strategy for the sub-sequence from S_k^* to S_N^*.

The above corollary is intuitively expressed by Bellman as the principle of optimality [92]: An optimal policy has the property that whatever the initial state and initial decision are, the remaining decisions must constitute an optimal policy with regard to the state resulting from the first decision.

4.2.3. Derivation of the Viterbi Algorithm

As a special DP algorithm, the Viterbi algorithm is designed for the hidden Markov model (HMM) and also obeys the aforementioned optimality theorem. The HMM is a statistical model in which the stochastic process is modelled as a Markov chain process with unobserved states. Although the hidden states are invisible, the outputs that are dependent on the hidden states are measurable to the observer. The original idea of the Viterbi algorithm comes from the fact that in order to find the most probable sequence of the invisible states in an HMM, DP can be applied. Suppose an HMM with the hidden state space $\chi = \{x_1, x_2, \dots, x_{M-1}, x_M\}$ and a total sequence of N stages. The state S_k for the k-th stage is represented by the probability distribution of the random variable $X_k \in \mathcal{X}$ with the initial value of $P(X_1 = x_i) = \pi_i$. The transition probability P_{ij} is used as the transition function from x_i to x_j. The observed output sequence $Y_1, Y_2, \dots, Y_N$ depends on the hidden sequence $X_1, X_2, \dots, X_N$. We can then apply the fundamental equations of DP and write

$$\begin{aligned} f_1 \mid_{X=x_i} &= P\left(Y_1 \mid X = x_i\right) \cdot \pi_i \\ f_k \mid_{X=x_i} &= \max_{j\in\{1,2,\dots,M\}} V_{1,k}\left(P\left(Y_k \mid X = x_i\right), P_{x_j x_i}, f_{k-1} \mid_{X=x_i}\right) \end{aligned} \tag{4-10}$$

where f_k is the cost function at the k-th stage and $V_{1,k}$ is the criterion function to evaluate the overall performance of the sequence from 1 to k. We denote the state value that maximizes the second equation in Eq. (4-10) as $d_k|_{X=x_i}$ and for the last stage N, we calculate $d_N|_{X=x_{l(N)}} = max_{i\in\{1,2,\dots,M\}} f_N|_{X=x_i}$,where $l(N)$ is the value that maximizes $f_N|_{X=x_i}$ .The most likely sequence is retrieved as $d_N|_{X=x_{l(N)}}, d_{N-1}|_{X=x_{l(N-1)}}, \dots, d_1|_{X=x_{l(1)}}$.

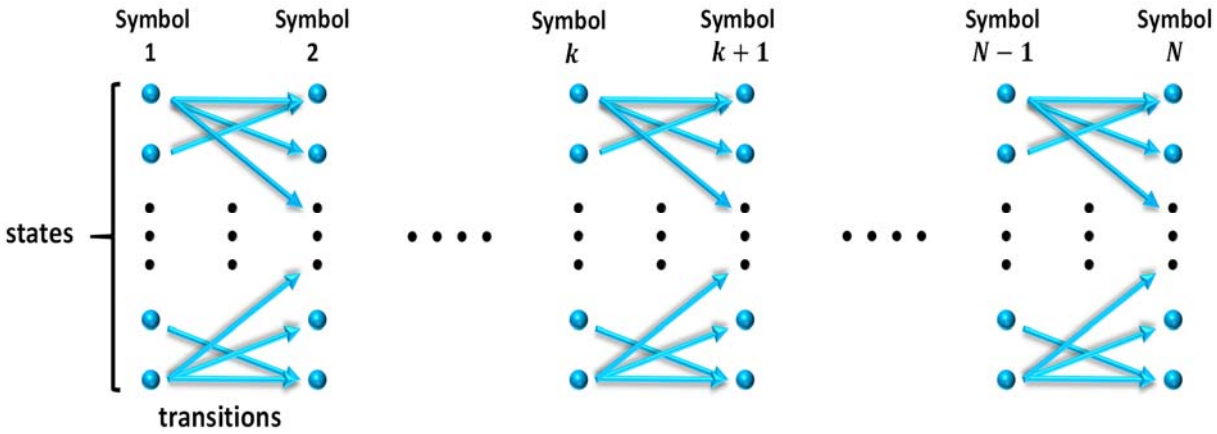

Figure 4.3. Principles of the Viterbi algorithm for maximum likelihood sequence estimation.

As shown in Figure 4.3, the Viterbi algorithm is straightforward for the symbol decision procedure in telecommunication systems, as the symbol sequence is split into discrete stages in nature and can be well modelled using HMM. The actual transmitted symbols are modelled as the hidden states while the received symbols represent the observed output sequence. Choosing a proper criterion function $V_{1,k}$ in Eq. (4-10), the recovered symbol sequence is guaranteed to be the most likely one by the optimality theorem.

4.2.4. Symbol Decision Algorithms for CM-DML Systems

For the CM-DML system, we propose two different symbol decision algorithms which are both based on DP.

Parameter Estimation Based DP (PE-DP). Under the assumption that all the transitions between two adjacent symbols are equally probable, we carefully define the criterion function to get the best overall performance, i.e. lowest BER. We first estimate the chirp parameters α and κ by sending training symbols, which will be further discussed in section 4.3.1. Then, we define the measurement of the cost of each possible transition between time x_{t1} and x_{t2} as follows

$$g\left(x_{t1},x_{t2}\right)=\left|P(x_{t1})-P_{obv}\left(x_{t1}\right)\right|^2+\left|\sqrt{P\left(x_{t2}\right)}e^{j\Delta\varphi}-\sqrt{P_{obv}\left(x_{t2}\right)}e^{j\Delta\varphi_{obv}}\right|^2 \quad (4\text{-}11)$$

where $P(x_{t1})$, $P(x_{t2})$ are the expected power levels at time t_1 and t_2, measured using pilot symbols, $P_{obv}(x_{t1})$ and $P_{obv}(x_{t2})$ are the measured optical signal powers, $\Delta\varphi$ is the estimated phase difference based on Eq. (4-2), and $\Delta\varphi_{obv}$ is the measured phase difference between the two consecutive symbols. Finally, we adopt the criterion function in summation form as Eq. (4-5), which is calculated through accumulating the values of Eq. (4-11) along the symbol sequence. Therefore, applying Eq. (4-8), the cost function can be written as

$$f\left(t_2\right)=\min_{\{x_{t1},x_{t2}\}\in \textit{all transitions}}\left\{g\left(x_{t1},x_{t2}\right)+f\left(t_1\right)\right\} \quad (4\text{-}12)$$

Table 4.1 illustrates the complete procedure of the PE-DP algorithm in detail.

Table 4.1. The PE-DP algorithm for symbol decision in the CM-DML system.

Step 1	Initialize the cost function value as zero.
Step 2	From the starting symbol in the sequence, Eq. (4-11) is calculated for each possible transition between two consecutive symbols (16 possible transitions for PAM-4 signals and 64 possible transitions for PAM-8 signals).
Step 3	Among all the calculated values, the minimum one is chosen as a surviving path, i.e., the most likely transition between the two symbols.
Step 4	Store the selected transition in Step 3, and add its corresponding value onto the cost function using Eq. (4-12).

Step 5	After executing Step 2 to Step 4 for each transition between the two symbols under consideration, update the cost function value as the newly calculated one. Then, move on to the next two adjacent symbols and repeat Step 2 to Step 4 till the end of the symbol sequence.
Step 6	On reaching the last symbol, there will be only one path left in the entire symbol sequence. By tracing back along the chain, all the symbols can thus be decided.

Maximum a Posteriori Based DP (MAP-DP). In PE-DP, we assume a uniform probability distribution of all the possible transitions, which is generally not the case in reality. Besides, the chirp parameters are sensitive to environmental changes such as fluctuations of the ambient temperature, and thus, have to be recalibrated from time to time. Therefore, we propose another approach based on the posterior probability given by $Pr\left(P_{t1}, P_{t2}|\tilde{P}_{t2}, \widetilde{\Delta\varphi}\right)$. Using the Bayes formula, we can write

$$\Pr\left(P_{t1}, P_{t2} \mid \tilde{P}_{t2}, \widetilde{\Delta\varphi}\right) = \frac{\Pr\left(\tilde{P}_{t2}, \widetilde{\Delta\varphi} \mid P_{t1}, P_{t2}\right) \cdot \Pr\left(P_{t1}, P_{t2}\right)}{\Pr\left(\tilde{P}_{t2}, \widetilde{\Delta\varphi}\right)} \tag{4-13}$$

where P_{t1} and P_{t2} are the actual transmitted powers for the consecutive symbols at time t_1 and t_2. $\tilde{P}_{t2}$ and $\widetilde{\Delta\varphi}$ are the observed symbol power at t_2 and the measured differential phase between t_1 and t_2, respectively.

Assuming the observed symbol power is independent from the differential phase, we obtain

$$\begin{aligned} \Pr\left(\tilde{P}_{t2}, \widetilde{\Delta\varphi} \mid P_{t1}, P_{t2}\right) &= \Pr\left(\tilde{P}_{t2} \mid P_{t2}\right) \cdot \Pr\left(\widetilde{\Delta\varphi} \mid P_{t1}, P_{t2}\right) \\ \Pr\left(\tilde{P}_{t2}, \widetilde{\Delta\varphi}\right) &= \Pr\left(\tilde{P}_{t2}\right) \cdot \Pr\left(\widetilde{\Delta\varphi}\right) \end{aligned} \tag{4-14}$$

Applying Eq. (4-14) on Eq. (4-13), we generate the posterior probability as

$$\Pr\left(P_{t1}, P_{t2} \mid \tilde{P}_{t2}, \widetilde{\Delta\varphi}\right) = \frac{\Pr\left(\tilde{P}_{t2} \mid P_{t2}\right) \cdot \Pr\left(\widetilde{\Delta\varphi} \mid P_{t1}, P_{t2}\right) \cdot \Pr\left(P_{t1}, P_{t2}\right)}{\Pr\left(\tilde{P}_{t2}\right) \cdot \Pr\left(\widetilde{\Delta\varphi}\right)} \tag{4-15}$$

In Eq. (4-15), $Pr\left(\tilde{P}_{t2}|P_{t2}\right)$ is the conditional probability of the received symbol power given the transmitted symbol. $Pr\left(\widetilde{\Delta\varphi}|P_{t1}, P_{t2}\right)$ is the conditional probability of the received differential phase between the two consecutive symbols, given their transmitted versions. $Pr(P_{t1}, P_{t2})$ is the prior probability distribution of the any two adjacent transmitted symbols. $Pr\left(\tilde{P}_{t2}\right)$ and $Pr\left(\widetilde{\Delta\varphi}\right)$ are the prior probability distribution of the received symbol power and the differential phase, respectively. All the above probability distributions can be obtained by sending training symbols where P_{t1} and P_{t2} are treated as known. The calculated posterior distribution is stored in a data structure such as a hash table for future reference. We set the criterion function as the accumulated product of $Pr\left(P_{t1}, P_{t2}|\tilde{P}_{t2}, \widetilde{\Delta\varphi}\right)$ along the symbol sequence. Thus, we can write the cost function as

$$f\left(t_2\right) = \max_{\{P_{t1},P_{t2}\} \in \textit{all transitions}} \left\{ \Pr\left(P_{t1}, P_{t2} \mid \tilde{P}_{t2}, \widetilde{\Delta\varphi}\right) \cdot f\left(t_1\right) \right\} \tag{4-16}$$

Table 4.2 illustrates the complete procedure of MAP-DP in detail.

Table 4.2. The MAP-DP algorithm for symbol decision in the CM-DML system.

Step 1	Initialize the cost function value as one.
Step 2	From the starting symbol in the sequence, for each possible transition between the two adjacent symbols, calculate the posterior probability of the observed pair $\{\tilde{P}_t, \widetilde{\Delta\varphi}\}$ using Eq. (4-15).
Step 3	Among all the calculated values, the maximum one is chosen as a surviving path, i.e., the most likely transition between the two symbols.
Step 4	Store the selected transition in Step 3, and multiply its corresponding value onto the cost function using Eq. (4-16).
Step 5	After executing Step 2 to Step 4 for each transition between the two symbols under consideration, update the cost function value as the newly calculated one. Then, move on to the next two adjacent symbols and repeat Step 2 to Step 4 till the end of the symbol sequence.
Step 6	On reaching the last symbol, there will be only one path left in the entire symbol sequence. By tracing back along the chain, all the symbols can thus be decided.

Without parameter estimation, MAP-DP makes the laser frequency chirp model transparent to the user. In essence, the chirp model is already included in the posterior probability distribution and is automatically learned through the training procedure. Although the learned distribution is influenced by chirp parameter changes, due to its statistical property, the distribution is more robust than the estimated parameters α and κ. Therefore, it is preferred to implement the MAP-DP algorithm rather than the PE-DP algorithm.

4.2.5. Simulation and Analysis of the CM-DML System

In the above sections, we have introduced the major concepts of the CM-DML scheme and its corresponding DP-based symbol decision algorithms. In this section, we further investigate the theoretical performance of the CM-DML system through computer-aided simulation which is carried out in Matlab®.

4.2.5.1. Simulation setup and parameters

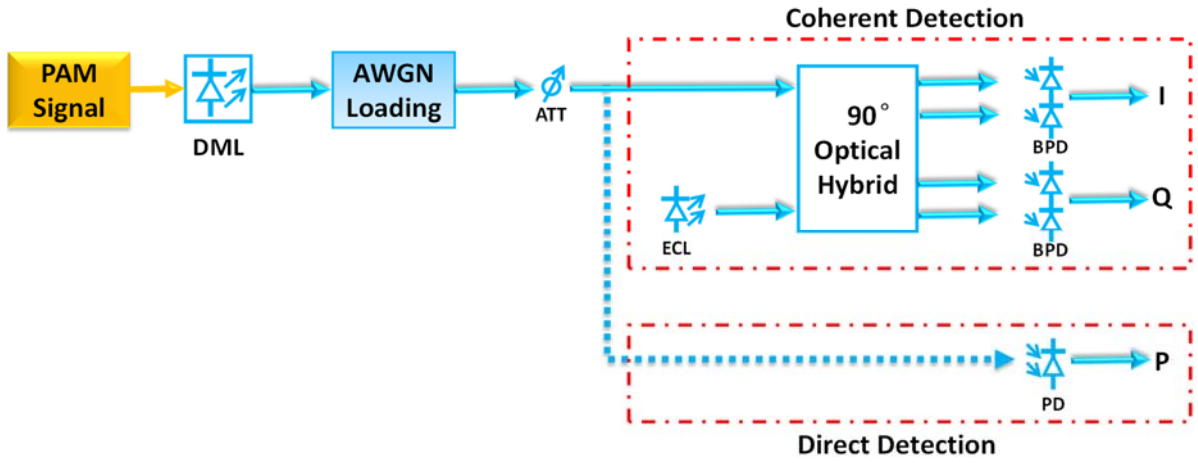

Figure 4.4. Simulation setup for theoretical analysis of the CM-DML system. AWGN: additive white Gaussian noise; ATT: optical attenuator; ECL: external cavity laser; BPD: balanced photodetector; PD: photodetector.

The following simulation in this section is based on the setup shown in Figure 4.4.

The baseband RF signal is first generated using a PRBS bit stream containing $2^{15}-1$ bits. After mapping the PRBS data into PAM-N format, the baseband signal is loaded onto the DML model. Complex AWGN is added onto the optical field including both the intensity and the phase. An attenuator is simulated to control the average received power. Finally, the signal is sent into the standard coherent receiver with two BPDs, which recovers the real and imaginary parts of the signal as I and Q, respectively. As a comparison, we also simulate the direct detection approach using a single photodetector, recovering only the intensity of the received signal denoted as P. For the symbol decision algorithm, we choose PE-DP for the coherent detection scheme and Euler distance comparison for direct detection scheme.

For convenience of analysis, we define

$$c_1 \triangleq \frac{\alpha}{2}, \quad c_2 \triangleq \frac{\alpha}{2}\cdot\frac{\kappa}{2}\cdot T \tag{4-17}$$

where α is the linewidth enhancement factor, κ is the adiabatic chirp coefficient and T is the symbol period determined by the transmitter baud rate in the simulation. We can thus rewrite Eq. (4-2) as

$$\Delta\varphi = c_1 \ln\frac{P(t_2)}{P(t_1)} + c_2\left(P(t_1)+P(t_2)\right) \tag{4-18}$$

The parameters used in the simulation are listed in Table 4.3.

Table 4.3. Simulation parameters for the CM-DML system.

Parameter	Value	Unit
DML Relative Intensity Noise	-145	dBc/Hz
DML Linewidth	1	MHz
DML Output Power (Average)	10	dBm

DML Chirp Parameter C1	2.3	-
DML Chirp Parameter C2	1.2	-
Photodiode Noise Equivalent Power	6×10^{-12}	$W/Hz^{1/2}$
Local Oscillator Power	15	dBm
Local Oscillator Relative Intensity Noise	-165	dBc/Hz
Local Oscillator Linewidth	10	kHz
Transmitted PAM Signal Baud Rate	10	GBaud
Received Optical Power	-10	dBm

From Eq. (4-11) and Eq. (4-15), we can see that the differential phase $\Delta\varphi$ has a major influence on the PE-DP algorithm. In order to perform a thorough analysis on what benefits we can have by taking the advantage of the information in $\Delta\varphi$, for the convenience of discussion, we fix the optical power for each PAM level. Therefore, from Eq. (4-18), only the chirp parameters C_1 and C_2 determine the value of $\Delta\varphi$. We generate 10-GBaud PAM-4 and PAM-8 signals for all the simulations with the output optical power levels set to be 7.0 dBm, 9.2 dBm,10.7 dBm,11.8 dBm for PAM-4 and 7.0 dBm, 8.1 dBm, 9.0 dBm, 9.7 dBm, 10.3 dBm, 10.8 dBm, 11.3 dBm, 11.8 dBm for PAM-8.

4.2.5.2. The advantage of CM-DML

We first demonstrate the advantage of CM-DML systems over the traditional IM-DD approach using the parameters illustrated above.

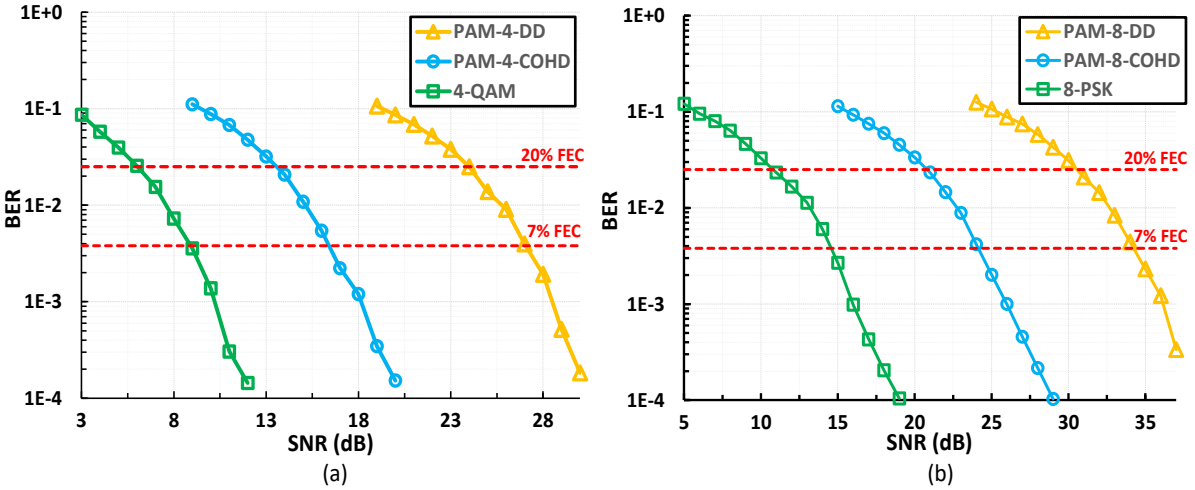

Figure 4.5. Simulated SNR sensitivity for the CM-DML system. (a) PAM-4; (b) PAM-8. DD: Direct detection; COHD: coherent detection; FEC: threshold of forward error correction codes.

Figure 4.5 shows the simulated SNR sensitivity of the system shown in Figure 4.4. We adopt 3.8×10^{-3} as the 7% hard-decision FEC threshold and 2.5×10^{-2} as the soft-decision FEC threshold. Figure 4.5 (a) shows the performance of a PAM-4 system. The CM-DML scheme achieves about 11-dB SNR sensitivity gain over the traditional IM-DD scheme. Furthermore, for comparison, we also simulate 4-QAM format under the same system parameters as a reference. The sensitivity gap between CM-DML and 4-QAM is about 7.5 dB, which is due to

the imperfect constellation point allocation of CM-DML compared with that of 4-QAM. Nevertheless, the above result signifies that it is reasonable to convert the one-dimensional PAM-4 format into a complex one for optical transmissions with large ASE noise, namely, a longer distance with more optical amplifiers.

Maintaining the same parameters in Table 4.3, we move on to PAM-8. For such a higher order modulation format, in terms of SNR sensitivity, the advantage of CM-DML over IM-DD gradually reduces to 10 dB as shown in Figure 4.5 (b). Moreover, compared with 8-PSK, the SNR sensitivity gap expands to 9.5 dB. Such a result can be understood by noticing that from PAM-4 to PAM-8, CM-DML requires 8-dB more SNR at 7% FEC threshold while from 4-QAM to 8-PSK, the SNR increment at 7% FEC threshold is 6 dB.

4.2.5.3. Optimal chirp parameters

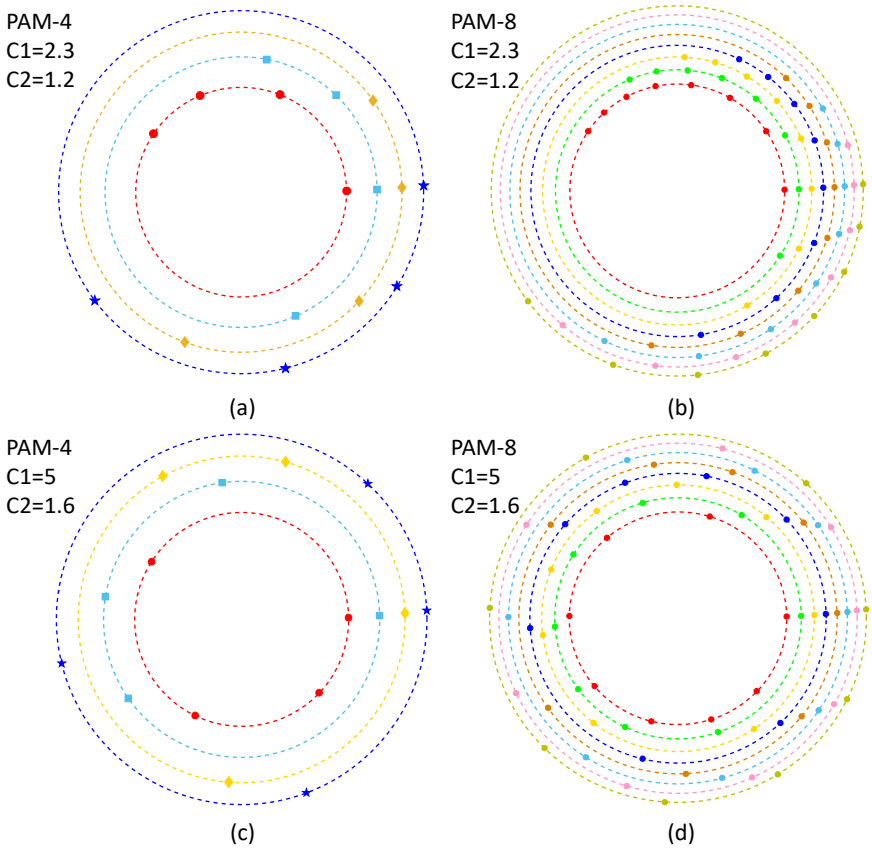

Figure 4.6. Chirp parameter impacts on the differential phase distribution. (a) PAM-4 with $C_1 = 2.3$ *and* $C_2 = 1.2$*; (b) PAM-8 with* $C_1 = 2.3$ *and* $C_2 = 1.2$*; (c) PAM-4 with* $C_1 = 5$ *and* $C_2 = 1.6$*; (d) PAM-8 with* $C_1 = 5$ *and* $C_2 = 1.6$*.*

It is well known that 4-QAM has the best SNR sensitivity due to its equally distributed constellation points. In contrast, the constellation point distribution of CM-DML relies on the chirp parameters. As shown in Figure 4.5 (a), the lack of a perfect constellation gives rise to the rather large SNR sensitivity gap between the CM-DML and 4-QAM. Therefore, we further examine the impacts of chirp parameters on the constellation of CM-DML. Figure 4.6 shows

the differential phase distribution on the 2-D complex plane, which is calculated by $\sqrt{P_m} \cdot exp(i\Delta\varphi_{mn})$. P_m is the optical power of the m-th level in PAM format and $\Delta\varphi_{mn}$ is the differential phase between the m-th power level and the n-th power level, which is calculated by Eq. (4-18). In Figure 4.6 (a) and (b), with the chirp parameters chosen as $C_1 = 2.3$ and $C_2 = 1.2$, for each power level, the differential phases fall into the range $[0, 0.81\pi]$ for both PAM-4 and PAM-8, leading to an unbalanced distribution where more than half of the power circle is empty. Thus, from Eq. (4-11), we can infer the SNR sensitivity degradation from 4-QAM (or 8-PSK) occurs for PAM-4 (or PAM-8). In Figure 4.6 (c) and (d), we set $C_1 = 5$ and $C_2 = 1.6$ and the frequency chirp effect is enhanced. We then observe all the differential phases fall into the range $[0,1.75\pi]$ and $[0,1.80\pi]$ for PAM-4 and PAM-8, respectively. The little difference of the phase range between PAM-4 and PAM-8 can be understood by noticing that PAM-8 has more levels than PAM-4 and the adiabatic chirp determined solely by the sum of power levels also contributes to the overall $\Delta\varphi$. Such a differential phase distribution almost occupies the entire $[0,2\pi]$ range, making the most out of the available space on the complex plane. Therefore, we can expect a much better SNR sensitivity performance for $C_1 = 5$ and $C_2 = 1.6$,compared with that of $C_1 = 2.3$ and $C_2 = 1.2$.

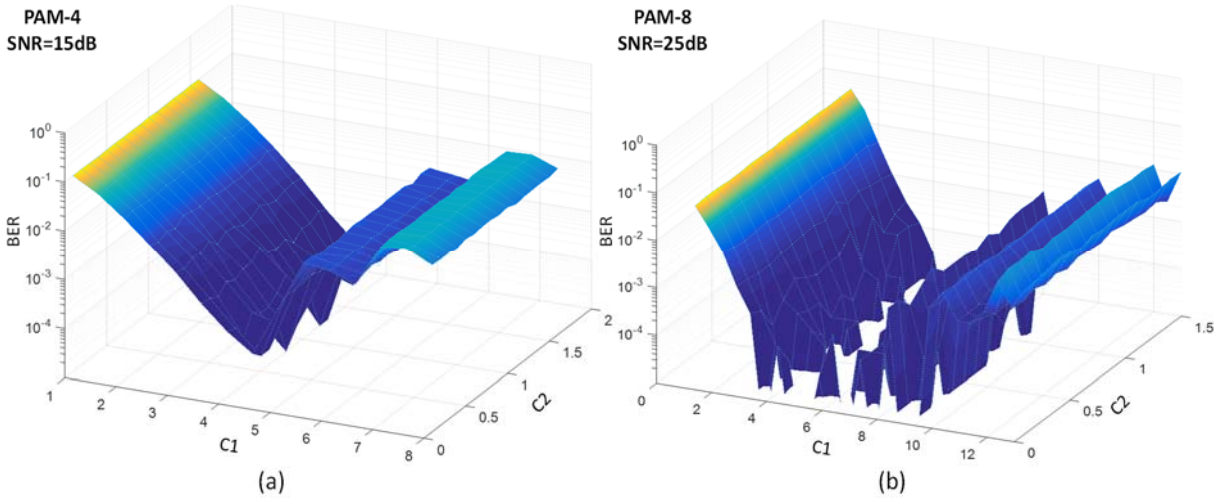

Figure 4.7. Chirp parameter impacts on bit error rate. (a) PAM-4 at SNR 15dB;(b) PAM-8 at SNR 25dB.

Figure 4.7 shows the impacts of chirp parameters on the overall system performance in terms of BER. In Figure 4.7 (a), for the PAM-4 CM-DML system at an SNR of 15 dB, when $C_1 < 4$, BER smoothly drops from 10^{-1} to below 10^{-4} with the increase of C_1, while when C_1 increases more than 5, BER rises to above 10^{-1} again. It is not surprising to notice that BER performance is sensitive to the chirp parameter C_1 and is rather robust to the variation of C_2. As expressed in Eq. (4-18), the sensitivity of $\Delta\varphi$ with respect to C_1 is determined by the coefficient $ln\big(P(t_2)/P(t_1)\big)$ ranging from 0 to 1.1 while the differential phase sensitivity with respect to C_2 is reflected through $P(t_2) + P(t_1)$ ranging from 0.01 to 0.03, which is much smaller than the value range of $\ln\big(P(t_2)/P(t_1)\big)$. When C_1 is below 4, BER decreases in a smooth manner

due to $\Delta\varphi$ is still within the 2π range where phase ambiguity does not happen. In contrast, when C_1 becomes larger than 5, BER rises with fluctuations that are caused by the ambiguities at phase unwrapping. Figure 4.7 (b) shows the case of PAM-8, in which we set the SNR at 25 dB. The overall trend of the BER curve is similar to that of PAM-4, except for the fact that the optimal value of C_1 sits in a much larger range from 4 to 8. If we ignore the minor influence from C_2, under a fixed value of C_1, both PAM-4 and PAM-8 have the same $\Delta\varphi$ range (see Figure 4.6), where PAM-8 has more intervals than PAM-4, giving smaller values of the coefficient $\ln\big(P(t_2)/P(t_1)\big)$. The performance of PAM-8 is thus less sensitive to C_1 than that of PAM-4, resulting in a larger optimal value range for C_1. Although the high-order modulation format requires much higher SNR to achieve a certain BER threshold (see Figure 4.5), it is more robust to chirp parameter variations. From the above analysis, we can see that there is an upper bound and also a lower bound for C_1 to achieve the lowest BER. In practice, $\Delta\varphi$ may also be sensitive to C_2 so that it is crucial to optimize the DML chirp parameters to achieve the optimal overall system performance.

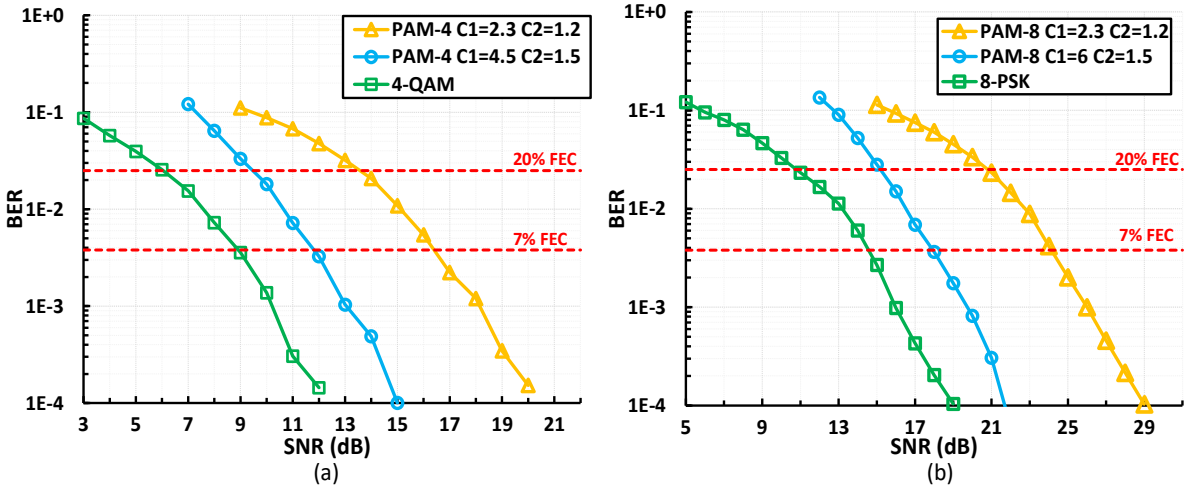

Figure 4.8. SNR sensitivity with the optimal chirp parameters. (a) PAM-4 with $C_1 = 4.5, C_2 = 1.5$; (b) PAM-8 with $C_1 = 6, C_2 = 1.5$.

Figure 4.8 shows the SNR sensitivity under the optimal choice of chirp parameters according to Figure 4.7, in which $C_1 = 4.5, C_2 = 1.5$ for PAM-4 and $C_1 = 6, C_2 = 1.5$ for PAM-8. In Figure 4.8 (a), the SNR sensitivity gap between PAM-4 CM-DML and 4-QAM shrinks to only 3 dB at 7% FEC threshold and in Figure 4.8 (b), the sensitivity difference between PAM-8 CM-DML and 8-PSK reduces to 3.5 dB. By simply reallocating the differential phase distribution, i.e. the point positions in the constellation, we obtain more than 4-dB SNR sensitivity improvement for PAM-4 and 6-dB for PAM-8.

4.2.5.4. Conclusions

In conclusion, based on the setup in Figure 4.4 and parameters in Table 4.3, we demonstrated the advantage of CM-DML scheme over traditional IM-DD scheme in terms of SNR sensitivity

through simulation which confirmed the theory developed in section 4.2.1 to section 4.2.4. Therefore, CM-DML is more suitable for long distance transmission to endure more noise such as the ASE noise from EDFAs. Furthermore, we pointed out that by optimizing the differential phase distribution on the 2-D complex plane through modifying the DML chirp parameters, significant SNR sensitivity improvement can be achieved. It is exciting to notice that SNR sensitivity of PAM-4 (or PAM-8) CM-DML can approach very close to that of 4-QAM (or 8-PSK). Although in reality both the power levels of PAM signal and the chirp parameters affect the differential phase distribution and are thus both need to be optimized, due to the low-cost property of DMLs, CM-DML is a promising modulation scheme to compete with the commercialized QAM transmitter using external modulators for cost-sensitive medium-reach optical links in MAN.

4.3. TRANSMISSION EXPERIMENTS BASED ON CM-DML

4.3.1. Chirp Parameter Estimation Algorithm

In the above section, we introduced the symbol decision algorithm using chirp parameter estimation (i.e. PE-DP), the effectiveness of which has already been confirmed by simulation results. Furthermore, the values of the chirp parameters play vital roles in the differential phase distribution that affects the overall system performance as a result. Therefore, precise characterization of the laser chirp parameters α and κ becomes a prior task in the experiment. α and κ are estimated through a data-aided approach, where the training symbols sent before the data have a pattern shown in Figure 4.9.

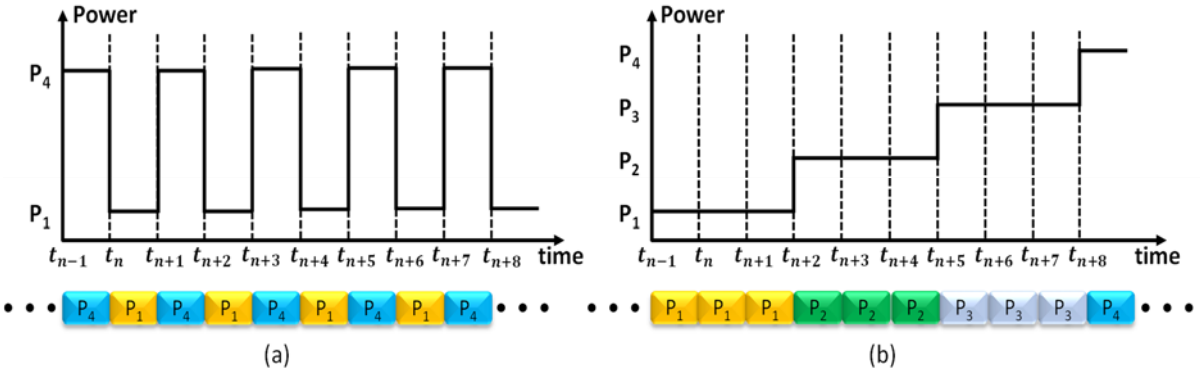

Figure 4.9. Training symbols for the estimation of laser chirp parameters. (a) Parameter α; (b) parameter κ.

As shown in Eq. (4-2), the phase difference $\Delta\varphi$ is related to the pattern of the modulation signal through the chirp parameters α and κ. Based on Eq. (4-2), α and κ can be characterized using specially designed training symbols. To estimate the coefficient α, the applied training symbol sequence is shown in Figure 4.9 (a), where the modulation signal switches between the highest and the lowest power levels in the PAM format. For a single transition from the highest to the lowest level, the differential phase between these two consecutive symbols is expressed by

$$\Delta\varphi\left(t_{n-1},t_n\right)=\frac{\alpha}{2}\left(\ln\frac{P_1}{P_4}+\kappa\cdot\frac{P_1+P_4}{2}\cdot T\right) \tag{4-19}$$

where P_1 and P_4 are the output optical powers of the DML corresponding to the lowest and highest PAM levels respectively, and $T=t_n-t_{n-1}$ is the symbol length. Similarly, for the transition from the lowest to the highest level, we have

$$\Delta\varphi\left(t_n,t_{n+1}\right)=\frac{\alpha}{2}\left(\ln\frac{P_4}{P_1}+\kappa\cdot\frac{P_1+P_4}{2}\cdot T\right) \tag{4-20}$$

Noting that in Eq. (4-19) and Eq. (4-20), the adiabatic chirp remains the same (i.e. the value of $\kappa\cdot(P_1+P_4)/2\cdot T$), the term corresponding to κ can be cancelled by subtracting Eq. (4-20) from Eq. (4-19). Thus, the chirp parameter α is given by

$$\alpha=\frac{\Delta\varphi\left(t_{n-1},t_n\right)-\Delta\varphi\left(t_n,t_{n-1}\right)}{\ln\left(P_1/P_4\right)} \tag{4-21}$$

Figure 4.9 (b) shows the training symbol sequence for estimating the parameter κ, where the modulated signal follows a staircase pattern increasing from the lowest to the highest power level. For the three continuous symbols at time t_{n-1}, t_n and t_{n+1}, the signal remains the same at P_1. Noticing that the transient chirp in Eq. (4-2) (i.e. the value of $\alpha/2\cdot\ln\left(P(t_n)/P(t_{n-1})\right)$), equals to zero when the output optical power maintains the same, we can thus write

$$\Delta\varphi\left(t_{n-1},t_n\right)=\Delta\varphi\left(t_n,t_{n+1}\right)=\frac{\alpha\kappa}{2}\cdot T\cdot P_1 \tag{4-22}$$

In order to remove the residue of frequency offset and also suppress the phase noise, the following three symbols at time t_{n+2}, t_{n+3} and t_{n+4} with power level P_2 are further taken into account. Similarly, we have

$$\Delta\varphi\left(t_{n+2},t_{n+3}\right)=\Delta\varphi\left(t_{n+3},t_{n+4}\right)=\frac{\alpha\kappa}{2}\cdot T\cdot P_2 \tag{4-23}$$

Subtracting Eq. (4-23) from Eq. (4-22), the parameter κ can thus be estimated as

$$\kappa=\frac{2\left(\Delta\varphi\left(t_{n-1},t_n\right)-\Delta\varphi\left(t_{n+2},t_{n+3}\right)\right)}{\alpha\left(P_1-P_2\right)T}=\frac{2\left(\Delta\varphi\left(t_n,t_{n+1}\right)-\Delta\varphi\left(t_{n+3},t_{n+4}\right)\right)}{\alpha\left(P_1-P_2\right)T} \tag{4-24}$$

Finally, to characterize α and κ as accurate as possible, in the following experiments, averaging is taken over two hundred training symbols.

4.3.2. The 10-GBaud Dual-polarization PAM-4 CM-DML System

In this section, employing the same 10-GHz MQW-DFB DML from GOOCH & HOUSEGO™ as in chapter 3, we experimentally demonstrate the capability of CM-DML systems to transmit 10-GBaud dual-polarization PAM-4 signal.

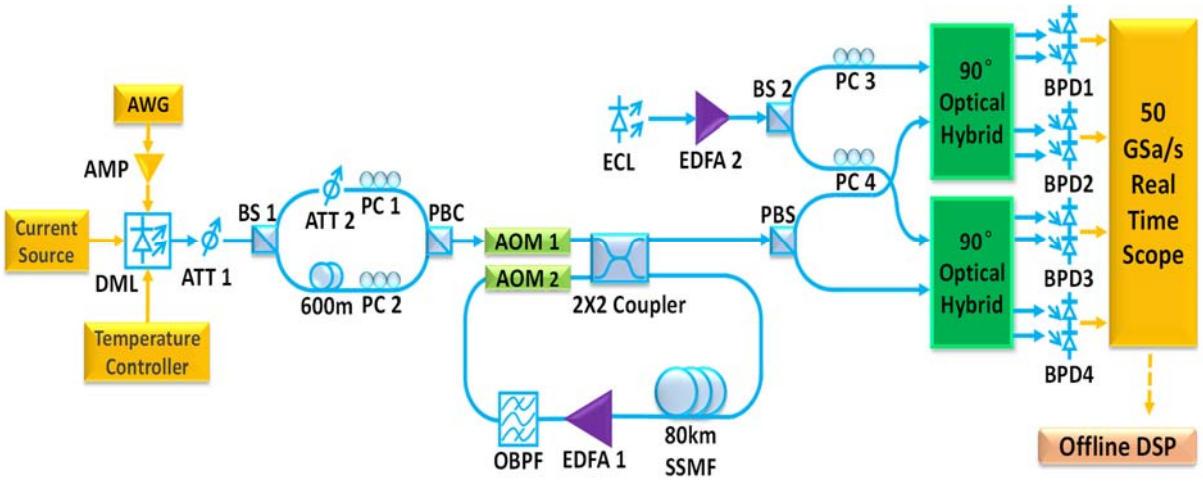

Figure 4.10. 10-GBaud dual-polarization CM-DML experiment setup. AWG: Arbitrary waveform generator; AMP: RF amplifier; DML: directly modulated laser; ATT: optical attenuator; BS: 50:50 beam splitter; PC: polarization controller; PBC: polarization beam combiner; AOM: acoustic optical modulator; OBPF: optical bandpass filter; EDFA: erbium-doped fibre amplifier; ECL: external cavity laser; PBS: polarization beam splitter; BPD: balanced photodetector.

Figure 4.10 illustrates the experimental setup for the 10-GBaud PAM-4 CM-DML system. The baseband PAM-4 signal is first generated by an AWG sampling at 10 GSa/s with $V_{pp} = 0.5\,V$. After amplified by a 19-dB RF amplifier, the PAM-4 RF signal drives the 10-GHz DML lasing around the wavelength of 1550 nm, with linewidth of 10 MHz. A temperature controller is connected to the DML. Monitored by the built-in thermistor and controlled through its inner thermoelectric cooler, the temperature of the laser diode is stabilized at 24.5℃. The DML is biased at 70 mA by a constant current source, which fully utilizes the linear response range of the DML, leading to an optical signal with equally spaced intensity. At the output end of the DML, an optical attenuator is attached to limit the average output power at 5 dBm. The optical signal is then fed into a dual-polarization emulator. The emulator first equally splits the signal into two paths, with one path delayed by 600-m SSMF and the other attenuated to guarantee the two polarizations have equal optical power at the input of polarization beam combiner (PBC). Employing such an emulator, the transmitted signals in the two polarizations are phase de-correlated. After polarization alignments through PC1 and PC2, these two paths are combined with a PBC and then launched into a recirculating loop consisting of one span of 80-km SSMF and an EDFA with a noise figure of 6 dB to compensate the loop loss of 17 dB. At the receiver, an ECL with linewidth of 10 kHz serves as the LO. The signal and LO are fed into a dual-polarization coherent receiver. The LO is first split into two paths both of which go through polarization controllers (PC3 and PC4) to align the polarizations of the two paths with the two polarization axes of the PBS, respectively. Each LO path is further mixed with its corresponding signal split by the PBS in the 90° optical hybrid, whose output is transformed into voltage by four 43-GHz balanced photodetectors (BPDs). The final RF signals are sampled by a 4-channel Tektronix® real-time oscilloscope running at 50 GSa/s with a 3-dB bandwidth of 16 GHz.

Offline DSP procedures are listed in Table 4.4.

Table 4.4. Offline DSP procedures for dual-polarization 10-GBaud PAM-4 CM-DML system.

Step 1	Chromatic dispersion compensation.
Step 2	Polarization demultiplexing by a 40-tap 2×2 adaptive MIMO equalizer based on MMA.
Step 3	LO frequency offset compensation.
Step 4	DML chirp parameter estimation.
Step 5	Differential phase reconstruction.
Step 6	Maximum likelihood sequence estimation and symbol decision.

For comparison, the intensity-only decision is made immediately after step 2. In step 3, linear fitting is chosen as the frequency offset compensation algorithm due to the complex parameter tuning procedure for digital PLL.

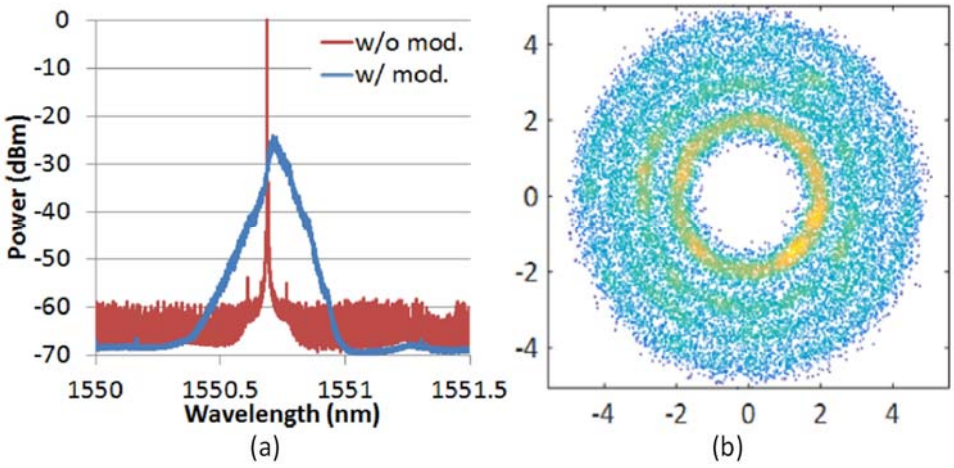

Figure 4.11. Optical spectrum and PAM-4 constellation. (a) Optical spectrum of dual polarization PAM-4 signal before entering the loop; (b) PAM-4 constellation of X polarization (OSNR 24 dB).

Figure 4.11 (a) shows the optical spectrum of the dual-polarization PAM-4 signal at the end of the polarization emulator, which has a 10-dB bandwidth of around 0.2 nm due to the broadening effect of laser frequency chirp. In Figure 4.11 (b), the PAM-4 constellation of X polarization after MMA equalization is shown. At OSNR of 24 dB, we can hardly distinguish the boundaries of the four rings of the PAM-4 signal indicating a relatively large BER for intensity-only symbol decision. However, by taking advantage of the differential phase between two adjacent symbols and applying MLSE for symbol decision, the BER is reduced from 0.012 to 0.00014 for this figure.

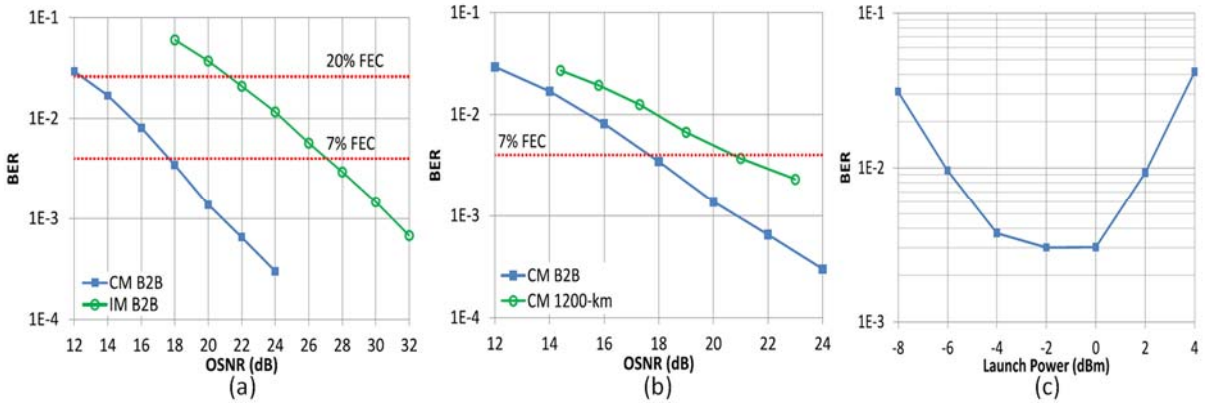

Figure 4.12. 40-Gb/s dual-polarization PAM-4 system performance. (a) OSNR sensitivity comparison between the complex modulation (CM) scheme and the intensity modulation (IM) scheme; (b) OSNR sensitivity of CM scheme after 1200-km SSMF; (c) BER versus fibre launch power. B2B: back-to-back measurement; 20% FEC:SD-FEC threshold of 3.8×10^{-3}*; 7% FEC: HD-FEC threshold of* 2.5×10^{-2}.

Figure 4.12 (a) shows an approximate 9-dB OSNR sensitivity enhancement of the CM-DML scheme compared with the IM scheme for back-to-back (B2B) measurement. However, in numerical simulations, as shown in Figure 4.5, we can see about 11-dB OSNR improvement. This discrepancy may be caused by variations of DML chirp parameters due to temperature fluctuations, and imperfections of the coherent receivers. The CM-DML system requires an OSNR of around 12 dB (18 dB) for 40-Gb/s signal to obtain a BER below 20% (7%) FEC threshold. Taking the previous dual-polarization PAM-4 coherent detection based DML experiment [12] as a benchmark, after data-rate normalization, our CM-DML system achieves about 8-dB OSNR sensitivity advantage. Figure 4.12 (b) illustrates the OSNR sensitivity after 1200-km SSMF transmission, where CM-DML still achieves the 7% FEC threshold at an OSNR of 18 dB, about 3 dB worse than the B2B case. The OSNR sensitivity degradation is probably caused by channel impairments such as the PDL, PMD and fibre nonlinearity. Since our transmission distance (i.e. 1200 km) already falls into the range of long-haul optical communications, it is well-proved that the CM-DML scheme has the capability of supporting optical transmission applications from short reach to medium reach. Furthermore, by employing DMLs with higher bandwidths, namely 20 GHz or even 40 GHz [93,94], the CM-DML system can readily achieve 100 Gb/s and beyond per wavelength.

4.3.3. The 10-GBaud Dual-polarization PAM-8 CM-DML System

In section 4.2.5, the potential of our proposed CM-DML scheme to sustain high-order PAM format has been shown (see Figure 4.5 (b)). Using the same setup with the same devices as illustrated in Figure 4.10, we increase the modulation format from PAM-4 to PAM-8.

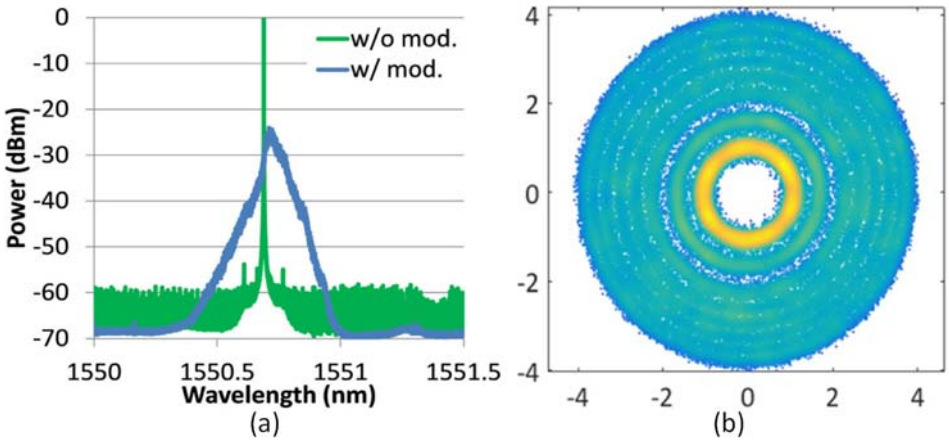

Figure 4.13. Optical spectrum and PAM-8 constellation. (a) Optical spectrum of dual polarization PAM-4 signal before entering the loop; (b) PAM-4 constellation of X polarization (OSNR 36 dB).

Figure 4.13 (a) shows the optical spectrum of the dual-polarization PAM-4 signal at the end of the polarization emulator, which has a 10-dB bandwidth of around 0.2 nm. In Figure 4.13 (b), the PAM-8 constellation of X polarization after MMA equalization is shown. Compared with the PAM-4 constellation at 24-dB OSNR in Figure 4.11 (b), even with a higher OSNR here, the boundaries of the rings become much harder to distinguish. However, at 36-dB OSNR, the CM-DML scheme can still achieve a BER as low as 0.006, while the IM scheme only has a BER of 0.018.

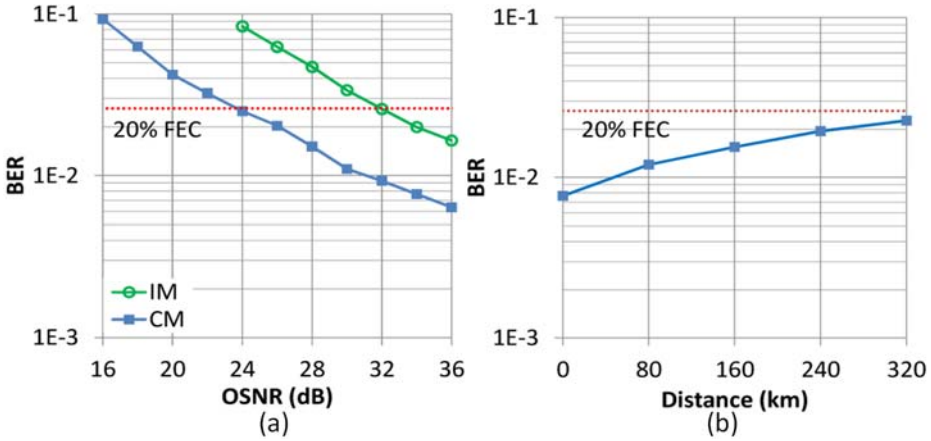

Figure 4.14. 60-Gb/s dual-polarization PAM-8 system performance. (a) OSNR sensitivity (B2B); (b) BER versus transmission distance. IM: Intensity modulation; CM: complex modulation.

Figure 4.14 shows the system performance of the dual-polarization PAM-8 CM-DML system reaching a data rate of 60 Gb/s. In Figure 4.14 (a), the OSNR sensitivity gap between the CM scheme and the IM scheme at 20% FEC is about 8 dB, which is decreased by around 1 dB compared to that of PAM-4 (see Figure 4.12 (a)), coincided with the simulation results shown in Figure 4.5. The required OSNR sensitivity for PAM-8 at 20% FEC rises to 24 dB, which is probably caused by the following reasons: (1) for the PAM-8 IM scheme, a BER floor exists

due to the DML modulation performance limitation, and the imperfection of the coherent receiver giving rise to distortions in the optical intensity signal after digital square operation; (2) the DML chirp parameters are not optimal for PAM-8 as discussed in section 4.2.5; (3) the inaccuracy of the DML frequency chirp model (see Eq. (4-1)) is enlarged by PAM-8 compared with that of PAM-4; (4) both the imperfections in the LO frequency offset compensation algorithm, and the phase noises of LO and the transmitter DML cause much severer inaccuracy in the differential phase ($\Delta\varphi$) reconstruction procedure, when the number of theoretical levels of $\Delta\varphi$ increases exponentially, i.e., from 16 levels for PAM-4 to 64 levels for PAM-8. Figure 4.14 (b) shows the capability of the dual-polarization PAM-8 CM-DML system to keep the BER below 20% FEC threshold after 320-km SSMF transmission, revealing its potential for short-reach and some medium-reach optical communication applications.

4.3.4. The 100-Gb/s Dual-polarization CM-DML System

So far, we have demonstrated a 40-Gb/s dual-polarization PAM-4 signal over 1200-km SSMF and a 60-Gb/s dual-polarization PAM-8 signal over 320-km SSMF both using the CM-DML scheme. The potential of a typical CM-DML system to deliver an even higher data rate, namely 100 Gb/s and beyond, was also revealed. In this section, by employing a pair of DMLs with 3-dB bandwidths of 16 GHz, we experimentally demonstrate single wavelength 100-Gb/s PAM-4 using polarization multiplexing over a transmission distance of 1600 km.

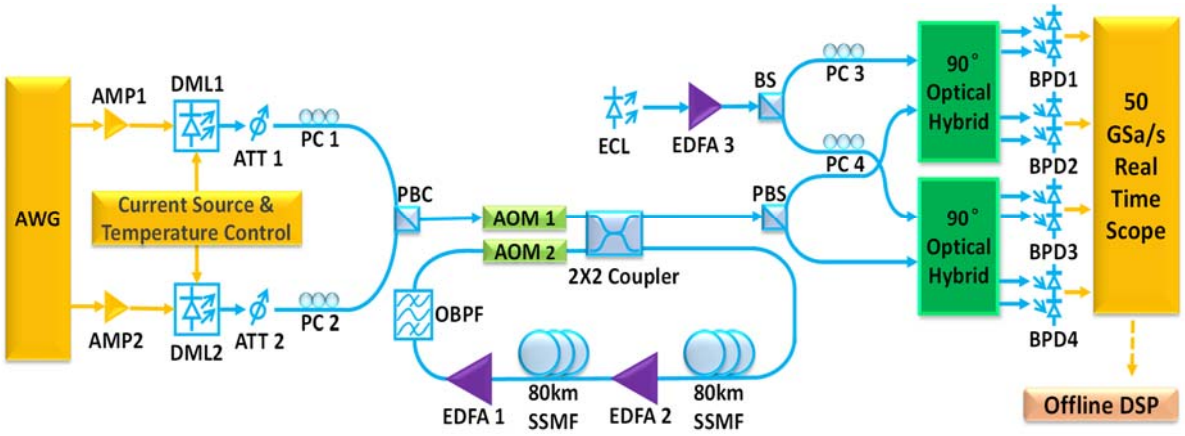

Figure 4.15. 100-Gb/s dual-polarization CM-DML experiment setup. AWG: Arbitrary waveform generator; AMP: RF amplifier; DML: directly modulated laser; ATT: optical attenuator; BS: 50:50 beam splitter; PC: polarization controller; PBC: polarization beam combiner; AOM: acoustic optical modulator; OBPF: optical bandpass filter; EDFA: erbium-doped fibre amplifier; ECL: external cavity laser; PBS: polarization beam splitter; BPD: balanced photodetector.

Figure 4.15 shows the setup of the 100-Gb/s CM-DML system which is generally similar to Figure 4.10. Two independent PRBS bit streams are generated and bit-mapped into the PAM-4 format. The AWG is run at a fixed sampling rate of 92 GSa/s, where each of the baseband 25-GBaud PAM-4 signals is thus Nyquist-pulse shaped by a raised cosine filter with a roll-off factor of 0.01. Amplified by a pair of phase-matched 19-dB RF amplifiers, the two output signals from the AWG are loaded onto the two independent DMLs both working around 1549.4

nm and biased at 70 mA. The temperature of the two laser chips is stabilized at 24°C to keep the frequency offset between these two transmitter lasers within 0.02 nm. After power adjustment by the attenuators, the optical power of each branch is set to be around 2 dBm. Before combined by the polarization beam combiner, the two branches are adjusted to be orthogonal in polarization states with each of the polarizations aligned to one of the PBC axes. The combined signal is then launched into a recirculating loop consisting of two spans of 80-km SSMF and two EDFAs to compensate the total loop loss of 34 dB. The noise figure of each EDFA is 6 dB. At the receiver, an ECL with a linewidth of 10 kHz is used as the LO which is further fed into the standard dual-polarization coherent receiver and mixed with the received signal. After optical to electrical conversion through the four 43-GHz BPDs, the output signals are sampled by a four-channel real-time oscilloscope run at 80 GSa/s with a 33-GHz 3-dB bandwidth for each channel.

The offline DSP procedures are listed in Table 4.5.

Table 4.5. Offline DSP procedures for the 100-Gb/s dual-polarization CM-DML system.

Step 1	Chromatic dispersion compensation.
Step 2	Polarization demultiplexing by a 40-tap 2×2 adaptive MIMO equalizer based on MMA.
Step 3	LO frequency offset compensation.
Step 4	Differential phase reconstruction.
Step 5	Probabilistic transition estimation.
Step 6	Maximum likelihood sequence estimation and symbol decision.

For comparison, the intensity-only decision is made immediately after step 2. In step 3, linear fitting is still chosen as the frequency offset compensation algorithm due to the complex parameter tuning procedure for digital PLL. For the symbol decision algorithm, the MAP-DP is applied in which the prior probability distributions are estimated based on training symbols.

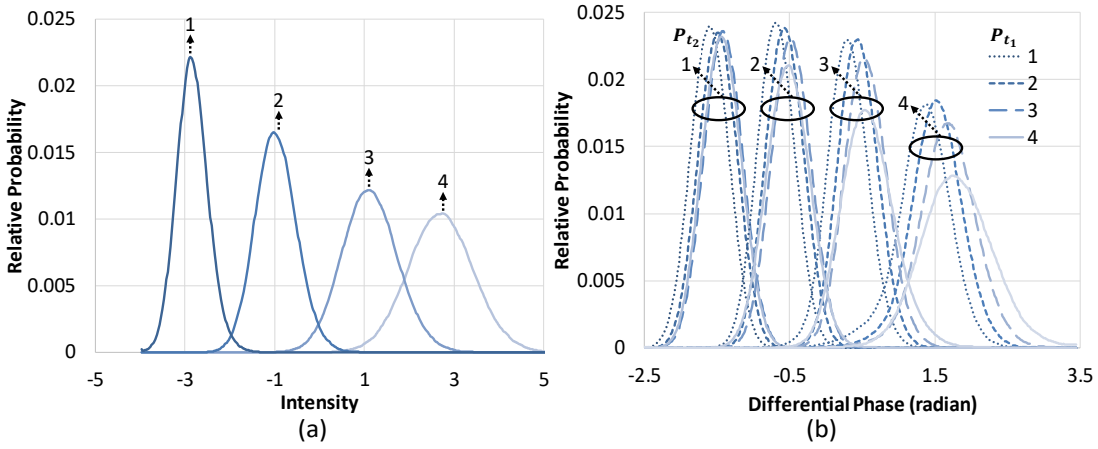

Figure 4.16. Probability Distributions of the measured PAM-4 (X polarization). (a) Intensity; (b) differential phase at OSNR of 24 dB.

Figure 4.16 (a) shows the intensity probability distributions $Pr(\tilde{P}_{t2}|P_{t2})$, the four power levels of which are all in Gaussian shapes. Because the optical signal is modulated by the equally spaced PAM-4 format and the noise is added onto the complex optical field, the higher the intensity level in PAM format, the larger noise is suffered by squaring the optical field to obtain the intensity. Figure 4.16 (b) illustrates the sixteen probability distributions of differential phase $Pr(\widetilde{\Delta\varphi}|P_{t1},P_{t2})$. Each curve cluster represents the statistics of the current state P_{t_2} and within each cluster, the four curves stand for four previous states P_{t_1}, respectively. In Eq. (4-15), we can further assume that $Pr(P_{t1},P_{t2})$ is a fixed probability distribution, because the generation of PRBS bit streams is based on the same algorithm except for different seeds. The probability distributions of the received power and differential phase can be considered as the same for the training symbol sequence and the meaningful data. Therefore, with the two sets of measured distributions shown in Figure 4.16, the MAP-DP algorithm is ready to be carried out.

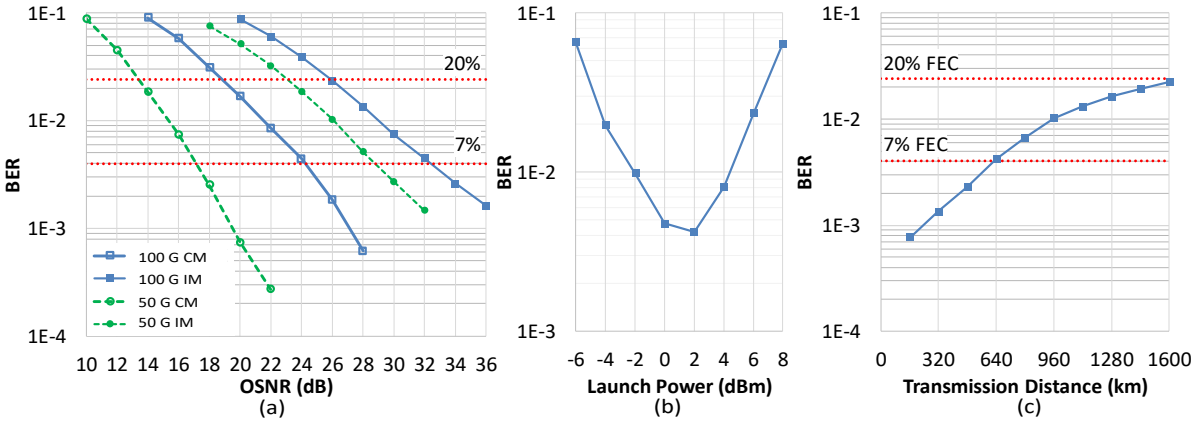

Figure 4.17. 100-Gb/s dual-polarization PAM-4 CM-DML system performance. (a) Back-to-back OSNR sensitivity; (b) BER versus fibre launch power after 640-km SSMF; (c) BER versus fibre transmission distance. 7%/20% FEC threshold: $3.8\times10^{-3}/2.5\times10^{-2}$*; CM: complex modulation; IM: Intensity modulation.*

Figure 4.17 (a) shows the B2B OSNR sensitivity where the 100-Gb/s CM-DML system requires 24-dB OSNR at 7% FEC threshold and 19-dB OSNR at 20% FEC threshold. For high baud rate signal, the adiabatic chirp induced differential phase ($\Delta\varphi$) would decrease (see Eq. (4-2)), which gives rise to a shrunk dynamic range of $\Delta\varphi$. As shown in Figure 4.16 (b), the two extrema of the differential phase have less than 3.5-radian gap (only the peak values are considered). Therefore, the increase of baud rate severely degrades the MLSE decoding gain. By decreasing the baud rate to 12.5 GBaud, for the intensity-only decision case, OSNR difference between 50-Gb/s and 100-Gb/s curves is about 3 dB. In contrast, the two CM curves show a 6-dB difference. In other words, the decreasing of adiabatic chirp induces 3-dB OSNR penalty at 25 GBaud. In this experiment, we only use commercially available DMLs whose frequency chirp effects are generally minimized. As discussed in section 4.2.5, by employing customized DMLs with optimal chirp parameters, the 100-Gb/s CM-DML system may achieve better OSNR sensitivity gain compared with the intensity-only decision scheme. In Figure 4.17 (b), the BER

versus launch power curve (after 640-km SSMF transmission) is measured, showing an optimal value of 2 dBm. Figure 4.17 (c) shows the curve of BER versus transmission distance. Without transmission, the 100-Gb/s CM-DML system is error free. The BER reaches 7% FEC threshold after 640-km SSMF transmission. For 20% FEC threshold (2.5×10^{-2}), the reachable distance is 1600 km.

4.4. RECEIVER FILTERING EFFECTS ON CM-DML SYSTEMS

As demonstrated in the above experiments, the DML frequency chirp provides another modulation dimension and gives a substantial system performance improvement. However, the chirp still inevitably broadens the optical spectrum and subsequently requires higher receiver bandwidth. For instance, 16-GHz is used for a 10-GBaud PAM-4 CM-DML system and 33-GHz is applied in the 25-GBaud pulse-shaped PAM-4 system. It is thus desirable to limit the electrical bandwidth requirement for CM-DML systems so as to keep the receiver cost relatively low. In this section, we provide systematic study of the impact of receiver filtering effects on the performance of CM-DML systems using 10G class DMLs and digital coherent receivers. We show that for 1-dB OSNR penalty at 20% FEC threshold, the required electrical bandwidth is 7.5 GHz for 10-Gbaud PAM-4 CM-DML systems.

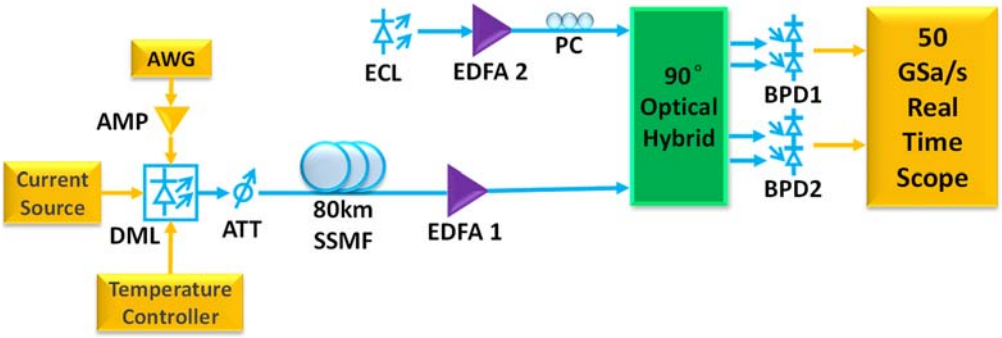

Figure 4.18. Experiment setup for receiver filtering effects on the CM-DML system. AWG: arbitrary waveform generator; AMP: RF amplifier; DML: directly modulated laser; ATT: optical attenuator; PC: polarization controller; EDFA: erbium-doped fibre amplifier; ECL: external cavity laser; BPD: balanced photodetector.

Figure 4.18 shows the experiment setup which is simplified by only using one polarization and removing the recirculating loop. A 2^{15} -1 PRBS is first mapped into baseband PAM-4 RF signal. Then, the PAM-4 signal is generated from an AWG at 10 GSa/s with V_{pp} of 500 mV resulting in a total data rate of 20 Gb/s. After amplification by a 19-dB RF amplifier, the signal is directly modulated onto the 10-GHz DML, which is lasing at a wavelength of around 1550 nm and biased at 70 mA by a constant current source. In order to avoid the drift of laser central frequency and the chirp parameters α and κ, it is essential to keep the temperature of the laser as constant, which is set at 24.9°C in the experiment. At the end of the DML, an optical attenuator is attached to limit the average launch power to 5 dBm. Afterwards, the optical signal is sent into an 80-km SSMF for transmission. At the receiver end, an ECL with 10-kHz

linewidth is used as the LO, which is fed into the coherent receiver at a power of 4 dBm. LO and the signal are mixed in a 90° optical hybrid followed by two pairs of BPDs with 43-GHz electrical bandwidth. The data is collected by a real-time scope running at 50 GSa/s with a 16-GHz electrical bandwidth.

The offline DSP procedures are listed in Table 4.6.

Table 4.6. Offline DSP for investigating the receiver filtering effects on the CM-DML system.

Step 1	Chromatic dispersion compensation.
Step 2	LO frequency offset compensation.
Step 3	Chirp parameter estimation.
Step 4	Digital lowpass filter.
Step 5	Maximum likelihood sequence estimation and symbol decision.

Without the polarization demultiplexing algorithm, the DSP procedures are simplified compared with those in Table 4.4. In step 4, to emulate the impact of varying electrical filter bandwidth, we apply a digital filter to the received complex signals. 4th-order Butterworth lowpass digital filters with 3-dB bandwidth varying from 5 to 15 GHz are employed.

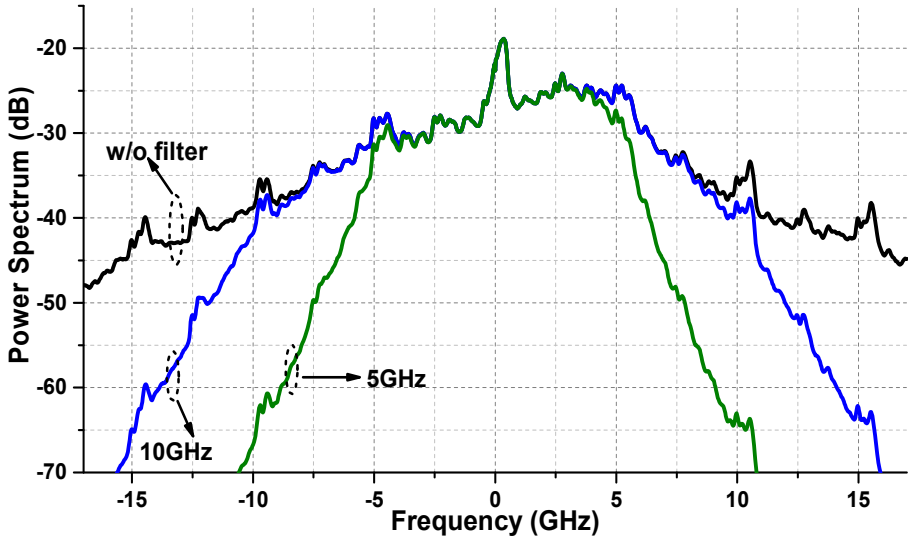

Figure 4.19. RF spectra of the received signals before and after digital filters. (80-km SSMF transmission with an OSNR of 30 dB)

Figure 4.19 compares the RF spectra of the received signals with the ones after filtering. For 10-GHz and 5-GHz filters, the signals are almost unaffected below the frequency of 8 GHz and 3.7 GHz, but are largely reduced above 10 GHz and 5 GHz, respectively. Therefore, the signal power is mainly conserved in the passband of the filter, containing as much as original data information that is concentrated at low frequency end of the spectrum. It is approximated that adding digital filters in this way is equivalent to using a low-cost, narrow bandwidth receiver that has similar frequency response.

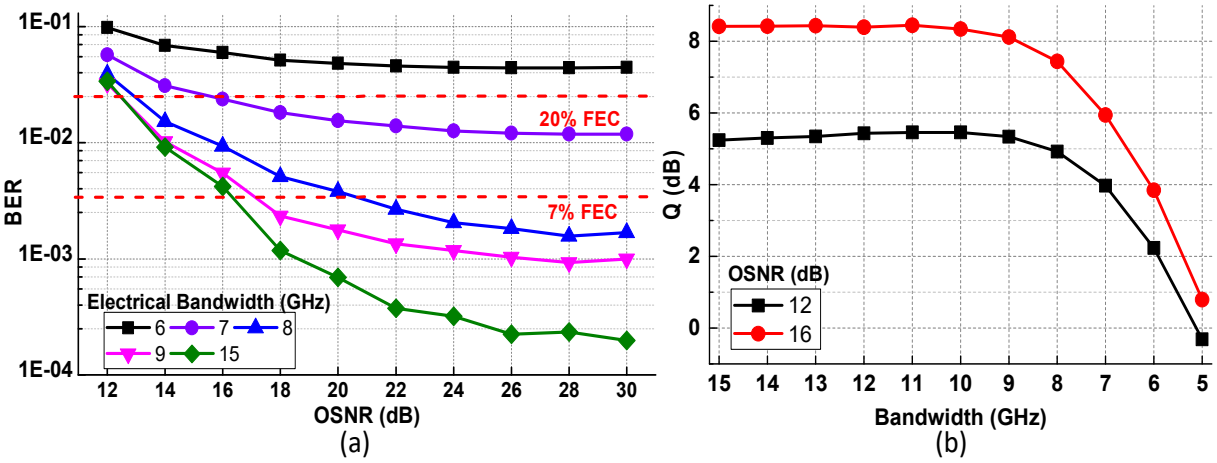

Figure 4.20. System performance for 10-Gbaud PAM-4 signal after 80-km SSMF transmission. (a) BER against OSNR; (b) Q against filter bandwidth. 7%/20% FEC threshold: $3.8\times10^{-3}/2.5\times10^{-2}$.

The BER performance dependence on receiver bandwidth is shown in Figure 4.20. We observe that OSNR sensitivity for 7% FEC is 16.2, 16.8, 20 dB when filter bandwidth is 15, 9, 8 GHz, respectively. The strong FEC of 20% overhead improves the filtering tolerance. The OSNR sensitivity for 20% FEC is 12.4, 12.4, and 12.9 dB when the filter bandwidth is 15, 9, 8 GHz, respectively. It can be estimated from Figure 4.20 (a), to limit the OSNR penalty within 1 dB, the filter bandwidth should be maintained within 8.5 and 7.5 GHz for 7% and 20% FEC, respectively. Figure 4.20 (b) shows the system Q factor as a function of the filter bandwidth at a fixed OSNR of 12 or 16 dB. It shows that 1-dB Q penalty bandwidth is 8.5 GHz and 7.5 GHz for OSNR of 16 dB and 12 dB, respectively, which is very similar to the result with OSNR penalty criterion. Below those required bandwidths, the Q penalties increase dramatically, which is due to the fact that narrow filtering has effectively removed the spectral component from the signals (see Figure 4.19). This system penalty can be understood from the principle of Viterbi algorithm in Eq. (4-11) where, due to the filter, signal distortions of both intensity and differential phase contribute to the variation of the cost function value. According to Eq. (4-2), the intensity distortion determines the estimation accuracy of the differential phase.

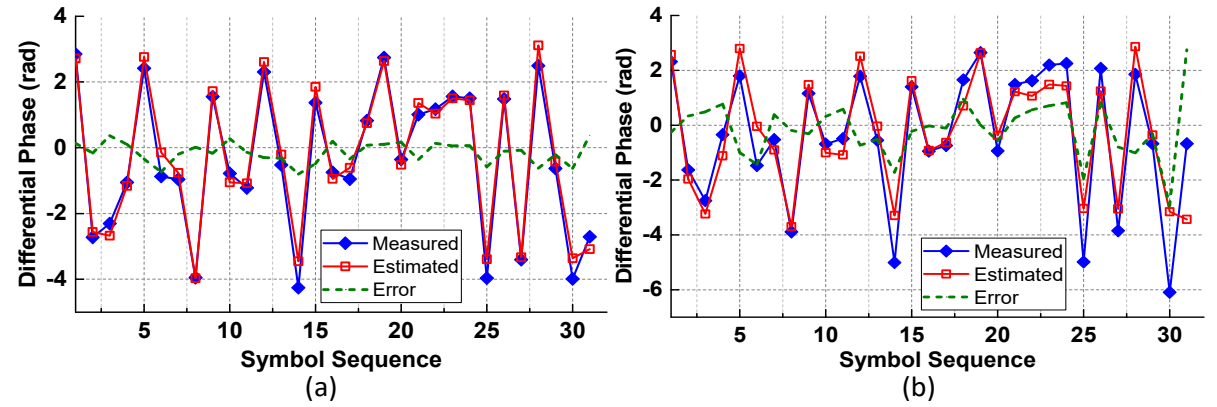

Figure 4.21. Measured and expected differential phase for 10-Gbaud PAM-4 signals. (80-km transmission at OSNR of 30 dB) (a) Without filter; (b) with an 8-GHz filter.

As shown in Figure 4.21 (a) and (b), when the bandwidth is large and negligible optical spectral component was cut off by the electrical filter, the measured differential phase agrees very well with the theoretical prediction in Eq. (4-2), with the errors bounded by 0.5 rad. However, when the filter bandwidth reduces below 8 GHz, we observe significant discrepancy between the measured and theoretically estimated differential phases, which will generate substantial distortions to the cost function.

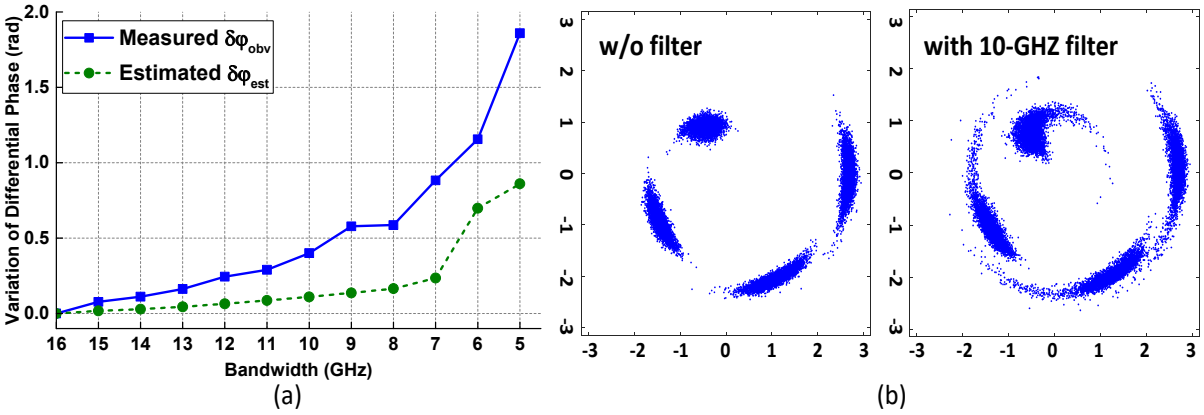

Figure 4.22. Receiver filtering effects on differential phase and reconstructed constellation of the CM-DML system. (a) Variation of the differential phase as a function of the filtering bandwidth; (b) reconstructed constellations (10-Gbaud PAM-4 signals over 80-km SSMF at OSNR of 30 dB).

Figure 4.22 (a) gives the average differential phase deviations from the original unfiltered data against the filter bandwidth. It can be seen that the measured differential phase is more vulnerable to filter bandwidth narrowing than the estimated one with a gap reaching as large as 1 rad with a 5-GHz filter. Around 7 to 8 GHz, a sharp increase of the differential phase can be observed implying an abrupt deviation that gives rise to the performance degradation near 7.5 GHz in Figure 4.20. This verifies the difference between the two differential phases contribute to the majority part of the cost function. The effects of both intensity and differential phase variations are combined in Eq. (4-4), where $\Delta\varphi$ denotes the measured differential phase and the rest part in the equation represents the estimated differential phase calculated by the intensity of the symbols. Using Eq. (4-4), the reconstructed constellation is intuitively shown in Figure 4.22 (b), where a more than 1-rad phase expansion can be observed after applying the 10-GHz filter.

Since filter cuts the high frequency components which correspond to the PAM-4 modulation levels of 1, and 4. We compute the symbol error ratio (SER) for the 4 levels with varying bandwidth. It can be seen from Figure 4.23 that above 8 GHz, the SER remains low, however, when the bandwidth narrows below 8 GHz, the SER increases dramatically, especially the one for level 4 which has the highest frequency. Level 1 is supposed to be associated with large errors as it is also at the high frequency. However, it also has small magnitude, and thus contributes less distortion in the cost function, and therefore does not incur as many errors as level 4. Despite the fact that significant chirp occurs in DML, the receiver bandwidth

requirement is about 7.5-8.5 GHz for 10-Gbaud CM-DML systems. This does not pose too much burden to electrical bandwidth requirement compared to conventional direct detection scheme where electrical bandwidth is about 7 GHz for 10-Gbaud systems. The robustness against filtering is attributed to the MLSE algorithm which can tolerate much distortion in the channel.

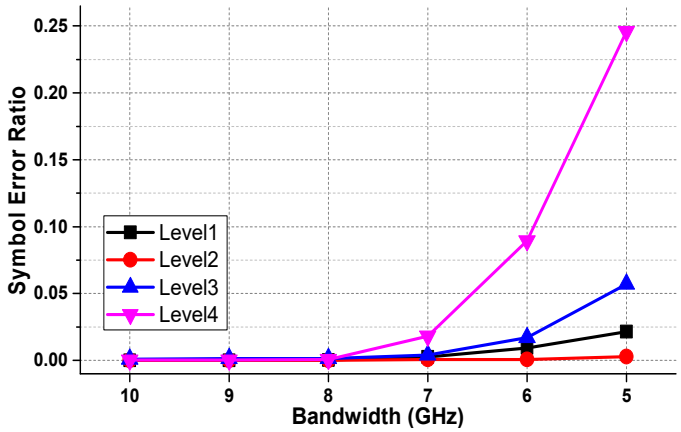

Figure 4.23. Symbol error ratio of different PAM levels versus receiver bandwidth. (10-Gbaud PAM-4 signal after 80-km transmission)

4.5. **CONCLUSIONS**

In this chapter, we experimentally showed that the CM-DML scheme can provide an attractive low-cost transceiver solution to support a wide range of short-to-medium reach optical transmission applications from data-center interconnects to MAN, where the required data rate can be as high as 100 Gb/s and even beyond. We also studied the receiver filtering effect of the CM-DML system. The experimental results implied that CM-DML systems can be implemented using cost-effective receiver subsystems without excessive increase of receiver bandwidth, greatly reducing the total system cost. Moreover, considering DMLs are two to three orders cheaper than the complex-modulation transmitters that are based on optical external modulators, the CM-DML systems have great potential to replace the commercialized dual-polarization QPSK products in medium-reach optical applications.

Chapter 5
Conclusions and Future Work

5.1. SUMMARY ON THIS THESIS

This thesis has extensively investigated a novel DML-based modulation scheme, namely, the complex-modulated DMLs, which provides a potential solution to short-to-medium reach optical communication systems with relatively low overall cost. As an intrinsic phenomenon associated with any semiconductor laser, the laser frequency chirp is traditionally considered as a detrimental factor to the overall performance of DML-based optical transmission systems and it is thus desirable to limit the chirp effect within a relatively low level. In this thesis, we took the advantage of the DML frequency chirp, and proposed the modulation scheme known as CM-DML. The dual-polarization digital coherent detection was employed as the receiver, where DSP algorithms were designed mainly for channel impairment compensation, polarization demultiplexing, and symbol decision. CD was the dominant transmission impairment in the scope of this thesis and was digitally compensated based on a frequency-domain algorithm. Since a multi-level format (i.e. PAM-M) was selected for modulation of the transmitter DML, we applied multi-modulus algorithm for polarization demultiplexing at the receiver. Furthermore, the symbol decision algorithms were specially designed to achieve the optimal system performance. Utilizing the general principle of dynamic programming as a foundation, two algorithms have been proposed, based on laser chirp parameter estimation and transition probability estimation, respectively. Equipped with the above DSP algorithms, we then carried out system-level simulations and lab experiments that verify the capability of the CM-DML system to support a data rate as high as 100 Gb/s over 1600-km standard signal-mode fibre. Finally, the receiver filtering effect on CM-DML systems was investigated, showing the feasibility of applying a relatively low-bandwidth receiver, which leads to low overall system cost.

In chapter 2, the basic concepts of commonly used subsystems in typical short-to-medium reach optical communication systems have been studied. For the transmitter, the principles of DMLs, optical intensity and I/Q modulators and the generation of advanced modulation formats for short-reach optical links were first introduced. For the receiver, we briefly introduced the simplest direct detection approach with a single photodetector, followed by the details of the coherent detection principle. We provided thorough investigations from coherent detection

based on single photodetectors to polarization and phase-diverse coherent receiver with BPDs. Then, some of the dominant linear and nonlinear transmission impairments inside an SSMF were discussed. In the last part of chapter 2, we provided a review of typical DSP procedures in the full-blown dual-polarization digital coherent receiver, including front-end correction, CD compensation, adaptive MIMO equalization for polarization demultiplexing, and carrier frequency and phase estimation. We introduced both time-domain and frequency-domain CD compensation algorithms. The classical CMA, MMA and DD-LMS algorithms for adaptive MIMO equalization were examined, where the singularity issue was addressed.

In chapter 3, basic characteristics of a typical DML were analysed theoretically with simulations. We first derived the classical laser rate equation from the physical mechanisms inside the active region of a typical semiconductor laser. The origin of laser frequency chirp was also introduced with its analytical expression given. Using the Langevin force approach, the laser noise was modelled in detail, which included the relative intensity noise and laser phase noise. A simulation model was then subsequently built using typical semiconductor laser parameters. Both the steady-state properties and modulation dynamics of the established DML rate-equation model were further investigated. Finally, we introduced the thermal FM of DML, where corresponding experiments were carried out to characterize such effect of a 10-GHz DML. With the observation of a 7.5-ns time constant, we further theoretically investigated the impact of such a fast time constant on the DML-based transmission systems.

In chapter 4, we provided details of the principles of the CM-DML system with a thorough simulation-based analysis and experimental demonstrations. The simulation results revealed that the CM-DML scheme is capable to support high-order PAM format. In addition, by optimizing chirp parameters, CM-DML can achieve an SNR sensitivity penalty within 5 dB compared with the traditional complex modulation formats such as 4-QAM and 8-PSK under the same simulation configuration. Using a 10-GHz DML, we experimentally demonstrated that for the back-to-back case, the CM-DML scheme has an approximate 9-dB and 8-dB ONSR sensitivity advantage over the IM-DD scheme at 20% FEC threshold for PAM-4 and PAM-8, respectively. Furthermore, we increased the data rate to 100 Gb/s utilizing polarization multiplexed PAM-4 single on a pair of 16-GHz DMLs and reported the maximum reachable distance of 1600 km at 20% FEC threshold. Finally, we experimentally showed the receiver bandwidth impact on the CM-DML system with an observation of only about 7.5–8.5 GHz receiver bandwidth requirement for 10-Gbaud PAM-4 CM-DML systems.

5.2. DISCUSSIONS AND FUTURE WORK

5.2.1. Overview on Future Challenges

For the next-generation short-reach optical communication, the main challenge will always be achieving a better transmission performance over a longer distance with higher data rates and lower costs. In addition, newly introduced technologies should also satisfy the co-existence or

back-compatibility requirement so that the upgrade of existing communication networks is best to only involve minor changes.

The first challenge is to increase the link data rate to 100 Gb/s and beyond. In order to meet the back-compatibility requirement, it is not surprising to notice that the standardized solutions to 40-Gb/s links and 100-Gb/s links are both based on the WDM technology, which maximally exploits the already deployed systems. However, with more and more available spectral bands being occupied by the existing and upcoming technologies, WDM solution alone cannot sustain the ever-growing capacity demand unless the co-existence requirement is loosened. It is thus desirable to increase the link capacity per wavelength. Much progress has already been made in recent research. Today the available solutions to 100 Gb/s and beyond per wavelength normally utilizes rather complex approaches, such as making use of high spectral efficiency modulation formats (i.e. DMT) and PDM. With IEEE's discussion on the standardization of 400GbE, it is expected that the link capacity is about to reach a new level. This pushes both the academia and industry of optical communication to search for feasible solutions that cater for such an exponentially growing capacity demand in the whole telecommunication networks.

The second challenge is to extend the reach of optical access links. In the IM-DD scheme, the extension of transmission distance not only exerts much pressure on the link power budget, but also tremendously increases the challenge in system performance such as combating the accumulated CD, which cannot be compensated in the direct detection approach in an easy manner. For instance, in a 100-Gb/s DMT system, severe CD-induced power fading is observed only after 4-km SSMF transmission [7]. With coherent receivers employed, both problems can be solved. As pointed out in [22], the power budget of the link can be increased from around 30 dB to around 50 dB by boosting the received power through the LO. As discussed in this thesis, CD-induced impairments can also be compensated through DSP algorithms, which is already mature in coherent long-haul transmission systems.

The third challenge is to keep the system cost and complexity relatively low for short-reach optical links. Despite the benefits we can have from employing digital coherent detection, the disadvantage is quite apparent, that is, the increase of cost and complexity. Although nowadays the achievable transmission data rate in an optical link has already been in the range of hundreds of Tb/s and even several Pb/s [95,96], these records are usually obtained through complex techniques like WDM, PDM and SDM. For optical access links, due to the cost-sensitive nature, it is unrealistic to employ such approaches which usually require complex devices and intensive DSPs. Even the use of digital coherent receivers will cause an unacceptable increase of cost. Therefore, the searching for low-cost solutions is a long-term task.

The three above-mentioned concerns from different aspects form the major trade-offs in the field of short-reach optical communication. In a nutshell, developing novel optical transmission technologies that are suitable for short-reach links with cost-effective transceivers and simple enough DSPs become the most challenging issue. Although various solutions have been extensively explored with thorough discussions on their pros and cons, in recent years, a

disruptive technology is emerging with potentials to solve these problems. The SiP technology has advanced in leaps and bounds, shedding light on a totally new method to achieve high system performance with cost-efficient devices. Silicon-based external modulators can be massively produced by the mature silicon manufacturing technologies, which will lead to rather low cost, but the bottleneck today still lies in the performance enhancement of SiP devices. Nevertheless, with more research work being carried out in the development of SiP technology, we may look forward to the coming of a new era in the field of short-reach optical communication in the near future.

5.2.2. CM-DML System with Self-coherent Receiver

In this thesis, our proposed CM-DML scheme makes the use of a digital coherent receiver, increasing both the system complexity and cost. Furthermore, the frequency offset between transmitter and receiver laser may introduce extra penalties to our proposed scheme. Although by detuning the lowpass filter in the digital domain we can discuss such penalties, it is always preferred to avoid this frequency offset. Noticing that only the information in the differential phase between two consecutive symbols is exploited for symbol decision, knowing the absolute phase of the signal through a full-blown digital coherent receiver is not necessary. A self-coherent receiver can thus be employed to reduce the receiver complexity and also avoid the extra local oscillator.

The self-coherent receiver is usually applied to the demodulation of M-ary differential phase-shift keying (M-DPSK) format, which is in essence a variation of direct detection. The advantage of the self-coherent detection over coherent detection is that there is no need to use the LO. Not only the receiver complexity and power consumption are reduced, but signal impairments and DSP algorithms related to the LO can be also avoided. Its basic principle is explained as follows.

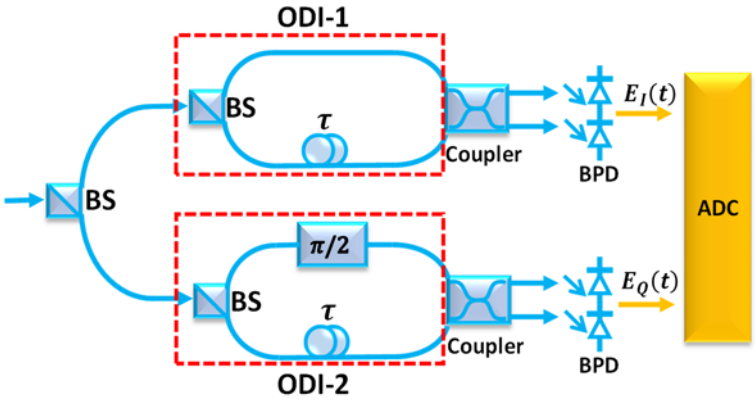

Figure 5.1. Basic structure of a self-coherent receiver. ODI: Optical delay interferometer; BPD: balanced photodetector; ADC: analog-to-digital converter.

The received signal $r(t)$ is first split into two branches and fed into the two ODIs. Then, in ODI-1, the signal is delayed by one symbol in one arm and beats with its original version in the

following coupler. After detection by the BPD, the electrical signal is finally sampled by the ADC. The lower arm of the receiver differs from the upper one that a 90° phase shift of the original signal is added inside ODI-2 and can thus extract the quadrature part of the input signal $r(t)$. The process can be described mathematically as

$$E_I(t) + jE_Q(t) = r(t) \cdot r^*(t-\tau) \cdot e^{j\theta} \tag{5-1}$$

where θ is the initial phase of the input optical field. Suppose $r(t)$ has the following form $r(t) = \sqrt{P_i} \cdot e^{j\varphi_i}$, $r(t-\tau) = \sqrt{P_j} \cdot e^{j\varphi_j}$, where P_i (φ_i) and P_j (φ_j) are the powers (phases) of the original symbol and the delayed one, respectively. Thus, the detected in-phase and quadrature components can be expressed by

$$\begin{aligned} E_I(t) &= \sqrt{P_i P_j}\cos\left(\varphi_i - \varphi_j + \theta\right) \\ E_Q(t) &= \sqrt{P_i P_j}\sin\left(\varphi_i - \varphi_j + \theta\right) \end{aligned} \tag{5-2}$$

where $\Delta\varphi = \varphi_i - \varphi_j$ is the differential phase of the two consecutive symbols.

In the case of the CM-DML system, in theory, the simplest way is using only one branch of the above receiver. According to Eq. (4-1), by characterization of the laser chirp parameters and output power levels in advance, it is possible to design the baseband PAM signal to get different values of $\Delta\varphi$ for each possible combination of the two consecutive symbols. Thus, employing only one branch of the self-coherent receiver, the symbols can be correctly decided. Another more feasible way is to use the full-blown self-coherent receiver. If the maximum differential phase between two consecutive symbols is designed to be within 2π, then from Eq. (5-2), we can calculate $\Delta\varphi$. The power of each symbol can be extracted from an extra direct detection branch. In this way, the aforementioned DP-aided symbol decision process can be employed. Furthermore, with both the power and differential phase information of the received signal, we can reconstruct the signal field by setting the initial phase to zero. Electronic CD compensation can thus be performed to mitigate the CD-induce impairments [97].

By utilizing the self-coherent receiver, we can further reduce the receiver cost and power consumption.

5.2.3. Fibre Nonlinearity Mitigation in Short-reach Transmission Systems

As mentioned in chapter 2, it is well-known that fibre nonlinearity is one of the fundamental limitations on increasing the data rate and extending the transmission distance for optical fibre communication systems [98]. During the past two decades, huge research efforts have been conducted for the mitigation of fibre nonlinearity [99-105], where both digital [99-104] and optical [105] methods have been excessively studied. For DSP-based mitigation approaches, basic principles of the commonly used techniques can be mainly categorized as: the full-field digital back-propagation [101], the digital phase conjugation [102] and the inverse Volterra series transfer function [103]. In a recent report [104], a novel DSP algorithm making use of support vector machine regression was proposed which outperformed the digital back-

propagation approach with an even higher computational efficiency. For optical fibre nonlinearity mitigation methods, in the past decade, the optical phase conjugation technique laid the foundation. However, due to various practical restrictions of these proposed schemes, such as the requirement of high-speed hardware or high computational complexity, none of them have been realized as a feasible solution for product development. A recent report [106] used phase-conjugated twin waves in PDM optical coherent systems, where the conjugate signal was transmitted on one polarization, and the appropriate CD pre-compensation led to the occurrence of symmetric nonlinear distortions on two polarizations for the received signals. This twin-wave technique has shown good performance for fibre nonlinearity compensation in either single-channel or multi-channel transmission with relatively low computational complexity. However, by sacrificing one polarization, this method halves the system spectral efficiency. Another recent research work concentrated on the employment of nonlinear Fourier transform (NFT) [107] to describe fibre nonlinearity. However, up to now, this approach is still in its infancy with little accomplished on the development of effective NFT-based fibre nonlinearity mitigation techniques. Therefore, it is not surprising to notice that in most current commercially available high-speed transceiver products, the receiver DSPs only compensate for linear channel impairments. The practical fibre nonlinearity compensation scheme is still an open question and will remain a hot research topic in the near future.

Bibliography

[1] P. J. Winzer and R.-J. Essiambre, "Advanced modulation formats for high-capacity optical transport networks," *Journal of Lightwave Technology,* vol. 24, no. 12, pp. 4711-4728, 2006.

[2] K. Kao and G. Hockham, "Dielectric-fibre surface waveguides for optical frequencies," *IEEE Proceedings J-Optoelectronics,* vol. 133, no. 3, pp. 191-198, 1986.

[3] M. Chagnon, M. Osman, M. Poulin, C. Latrasse, J.-F. Gagné, Y. Painchaud, et al., "Experimental study of 112 Gb/s short reach transmission employing PAM formats and SiP intensity modulator at 1.3 μm," *Optics Express*, vol. 22, no. 17, pp. 21018-21036, 2014.

[4] K. Zhong, X. Zhou, T. Gui, L. Tao, Y. Gao, W. Chen*, et al.*, "Experimental study of PAM-4, CAP-16, and DMT for 100 Gb/s short reach optical transmission systems," *Optics Express,* vol. 23, no. 2, pp. 1176-1189, 2015.

[5] L. Tao, Y. Wang, Y. Gao, and N. Chi, "High order CAP system using DML for short reach optical communications," *IEEE Photonics Technology Letters,* vol. 26, no. 13, pp. 1348-1351, 2014.

[6] T. Tanaka, M. Nishihara, T. Takahara, W. Yan, L. Li, Z. Tao*, et al.*, "Experimental demonstration of 448-Gbps+ DMT transmission over 30-km SMF," in *Proceedings Optical Fiber Communication Conference* (San Francisco, California, United States, 2014), p. M2I.5.

[7] C. Xie, P. Dong, S. Randel, D. Pilori, P. J. Winzer, S. Spiga, et al., "Single-VCSEL 100-Gb/s short-reach system using discrete multi-tone modulation and direct detection," in *Proceedings Optical Fiber Communication Conference* (Los Ageles, California, United States, 2015), p. Tu2H. 2.

[8] M. Muller, W. Hofmann, A. Nadtochiy, A. Mutig, G. Bohm, M. Ortsiefer*, et al.*, "1.55 μm high-speed VCSELs enabling error-free fiber-transmission up to 25 Gbit/s," in *Proceedings IEEE International Semiconductor Laser Conference* (Kyoto, Japan, 2010), pp. 156-157.

[9] F. Karinou, C. Prodaniuc, N. Stojanovic, M. Ortsiefer, A. Daly, R. Hohenleitner*, et al.*, "Directly PAM-4 modulated 1530-nm VCSEL enabling 56 Gb/s data-center interconnects," *IEEE Photonics Technology Letters, IEEE,* vol. 27, no. 17, pp. 1872-1875, 2015.

[10] R. Rodes, M. Mueller, B. Li, J. Estaran, J. B. Jensen, T. Gruendl*, et al.*, "High-speed 1550 nm VCSEL data transmission link employing 25 GBd 4-PAM modulation and hard decision forward error correction," *Journal of Lightwave Technology,* vol. 31, no. 4, pp. 689-695, 2013.

[11] C. Xie, P. Dong, P. Winzer, C. Gréus, M. Ortsiefer, C. Neumeyr*, et al.*, "960-km SSMF transmission of 105.7-Gb/s PDM 3-PAM using directly modulated VCSELs and coherent detection," *Optics Express,* vol. 21, no. 9, pp. 11585-11589, 2013.

[12] C. Xie, S. Spiga, P. Dong, P. J. Winzer, A. Gnauck, C. Gréus*, et al.*, "Generation and transmission of 100-Gb/s PDM 4-PAM using directly modulated VCSELs and coherent

detection," in *Proceedings Optical Fiber Communication Conference* (San Francisco, California, United States, 2014), p. Th3K. 2.

[13] K. Prince, M. Ma, T. B. Gibbon, C. Neumeyr, E. Rönneberg, M. Ortsiefer*, et al.*, "Free-running 1550 nm VCSEL for 10.7 Gb/s transmission in 99.7 km PON," *Journal of Optical Communications and Networking,* vol. 3, no. 5, pp. 399-403, 2011.

[14] D. Parekh, B. Zhang, X. Zhao, Y. Yue, W. Hofmann, M. C. Amann*, et al.*, "90-km single-mode fiber transmission of 10-Gb/s multimode VCSELs under optical injection locking," in *Proceedings Optical Fiber Communication Conference* (San Diego, California, United States, 2009), p. OTuK7.

[15] T. B. Gibbon, K. Prince, C. Neumeyr, M. Ortsiefer, and I. Tafur Monroy, "10 Gb/s 1550 nm VCSEL transmission over 23.6 km SMF with no dispersion compensation and no injection locking for WDM PONs," in *Proceedings Optical Fiber Communication Conference* (San Diego, California, United States, 2010), p. JThA30.

[16] D. Che, Q. Hu, F. Yuan, Q. Yang, and W. Shieh, "Enabling complex modulation of directly modulated signals using laser frequency chirp," *IEEE Photonics Technology Letters,* vol. 27, no. 22, pp. 2407-2410, 2015.

[17] Q. Hu, D. Che, Y. Wang, F. Yuan, Q. Yang, and W. Shieh, "Complex modulation and detection with directly modulated lasers," *Optics Express,* vol. 23, no. 25, pp. 32809-32819, 2015.

[18] D. Plant, "Silicon photonic enabled 400G/1T short reach optical interconnects for data center applications," in *Proceedings Signal Processing in Photonic Communications* (Boston, Massachusetts, United States, 2015), p. SpS1C.1.

[19] R. Rodes Lopez, J. M. Estaran Tolosa, B. Li, M. Muller, J. B. Jensen, T. Gründl*, et al.*, "100 Gb/s single VCSEL data transmission link," in *Proceedings Optical Fiber Communication Conference* (Los Angeles, California, United States, 2012), p. PDP5D.10.

[20] H. Dalir and F. Koyama, "29 GHz directly modulated 980 nm vertical-cavity surface emitting lasers with bow-tie shape transverse coupled cavity," *Applied Physics Letters,* vol. 103, no. 9, p. 091109, 2013.

[21] F. Karinou, R. Rodes, K. Prince, I. Roudas, and I. T. Monroy, "IM/DD vs. 4-PAM using a 1550-nm VCSEL over short-range SMF/MMF links for optical interconnects," in *Proceedings Optical Fiber Communication Conference* (Anaheim, California, United States, 2013), p. OW4A.2.

[22] N. Yoshimoto, J.-i. Kani, S.-Y. Kim, N. Iiyama, and J. Terada, "DSP-based optical access approaches for enhancing NG-PON2 systems," *IEEE Communication Magazine*, vol. 51, no. 3, pp. 58-64, 2013.

[23] E. L. Wooten, K. M. Kissa, A. Yi-Yan, E. J. Murphy, D. A. Lafaw, P. F. Hallemeier*, et al.*, "A review of lithium niobate modulators for fiber-optic communications systems," *IEEE Journal of Selected Topics in Quantum Electronics,* vol. 6, no. 1, pp. 69-82, 2000.

[24] F. Koyama and K. Iga, "Frequency chirping in external modulators," *Journal of Lightwave Technology,* vol. 6, no. 1, pp. 87-93, 1988.

[25] K. Kawano, T. Kitoh, H. Jumoni, T. Nozawa and M. Yanagibashi, "New traveling-wave electrode Mach-Zehnder optical modulator with 20GHz bandwidth and 4.7V driving voltage at 1.52μm wavelength", *Electronics Letters*, vol. 25, no. 20, pp. 1382-1383, 1989.

[26] R. Becker, "Broad-band guided-wave electrooptic modulators," *IEEE Journal of Quantum Electronics,* vol. 20, no. 7, pp. 723-727, 1984.

[27] C. A. Brackett, "Dense wavelength division multiplexing networks: principles and applications," *IEEE Journal on Selected Areas in Communications,* vol. 8, no. 6, pp. 948-964, 1990.

[28] P. Watts, R. Waegemans, M. Glick, P. Bayvel, and R. Killey, "An FPGA-based optical transmitter design using real-time DSP for advanced signal formats and electronic predistortion," *Journal of Lightwave Technology,* vol. 25, no. 10, pp. 3089-3099, 2007.

[29] Q. Hu, D. Che, Y. Wang, and W. Shieh, "Advanced modulation formats for high-performance short-reach optical interconnects," *Optics Express,* vol. 23, no. 3, pp. 3245-3259, 2015.

[30] J. Zhou, C. Yu, and H. Kim, "1.5-μm, 2 1.4-Gbps 4-PAM VCSEL link for optical access applications," in *Proceedings Optical Fiber Communication Conference* (Los Angeles, California, United States, 2015) , p. Th2A.54.

[31] J. Lee, N. Kaneda, T. Pfau, A. Konczykowska, F. Jorge, J.-Y. Dupuy*, et al.*, "Serial 103.125-Gb/s transmission over 1 km SSMF for low-cost, short-reach optical interconnects," in Proceedings *Optical Fiber Communication Conference* (San Francisco, California, United States, 2014), p. Th5A.5.

[32] W. Shieh, H. Bao, and Y. Tang, "Coherent optical OFDM: theory and design," *Optics Express,* vol. 16, no. 2, pp. 841-859, 2008.

[33] L. A. Neto, M. Gay, L. Bramerie, C. Peucheret, Y. Frignac, J.-C. Simon*, et al.*, "Beyond 25 Gbit/s directly modulated, directly detected OFDM using channel flattening by a Fabry-Perot filter," in *Proceedings Optical Fiber Communication Conference* (Los Angeles, California, United States, 2015), p. M3J. 5.

[34] J. B. Anderson, *Digital Transmission Engineering*, John Wiley and Sons Inc., 2004.

[35] T. Okoshi and K. Kikuchi*, Coherent Optical Fiber Communications*. Kluwer Academic, 1988.

[36] P. Richards, "Bolometers for infrared and millimeter waves," *Journal of Applied Physics*, vol. 76, no. 1, pp. 1-24, 1994.

[37] G. Agrawal, *Nonlinear Fiber Optics 4th ed*., Academic Press, 2001.

[38] H. J. Dutton, *Understanding Optical Communications*, Prentice Hall, 1998.

[39] A. Kumar and A. K. Ghatak, *Polarization of Light with Applications in Optical Fibers*, SPIE Press, 2011.

[40] L. N. Binh, *Optical Fiber Communication Systems with Matlab and Simulink Models*, CRC Press, 2014.

[41] S. J. Savory, "Digital coherent optical receivers: algorithms and subsystems," *IEEE Journal of Selected Topics in Quantum Electronics,* vol. 16, no. 5, pp. 1164-1179, 2010.

[42] F. Ouellette, "Dispersion cancellation using linearly chirped Bragg grating filters in optical waveguides," *Optics Letters,* vol. 12, no. 10, pp. 847-849, 1987.

[43] S. Watanabe, T. Naito, and T. Chikama, "Compensation of chromatic dispersion in a single-mode fiber by optical phase conjugation," *IEEE Photonics Technology Letters,* vol. 5, no. 1, pp. 92-95, 1993.

[44] A. H. Gnauck, C. R. Giles, L. J. Cimini, J. Stone, L. W. Stulz, S. K. Korotky*, et al.*, "8-Gb/s-130 km transmission experiment using Er-doped fiber preamplifier and optical dispersion equalization," *IEEE Photonics Technology Letters,* vol. 3, no. 12, pp. 1147-1149, 1991.

[45] T. Koch and R. Alferness, "Dispersion compensation by active predistorted signal synthesis," *Journal of Lightwave Technology,* vol. 3, no. 4, pp. 800-805, 1985.

[46] T. Saito, N. Henmi, S. Fujita, M. Yamaguchi, and M. Shikada, "Prechirp technique for dispersion compensation for a high-speed long-span transmission," *IEEE Photonics Technology Letters,* vol. 3, no. 1, pp. 74-76, 1991.

[47] M. G. Taylor, "Coherent detection method using DSP for demodulation of signal and subsequent equalization of propagation impairments," *IEEE Photonics Technology Letters,* vol. 16, no. 2, pp. 674-676, 2004.

[48] S. J. Savory, G. Gavioli, R. I. Killey, and P. Bayvel, "Electronic compensation of chromatic dispersion using a digital coherent receiver," *Optics Express,* vol. 15, no. 5, pp. 2120-2126, 2007.

[49] G. Goldfarb and G. Li, "Chromatic dispersion compensation using digital IIR filtering with coherent detection," *IEEE Photonics Technology Letters,* vol. 19, no. 13, pp. 969-971, 2007.

[50] M. Kuschnerov, F. N. Hauske, K. Piyawanno, B. Spinnler, M. S. Alfiad, A. Napoli*, et al.*, "DSP for coherent single-carrier receivers," *Journal of Lightwave Technology,* vol. 27, no. 16, pp. 3614-3622, 2009.

[51] C. C. Do, A. V. Tran, C. Zhu, S. Chen, T. Anderson, D. Hewitt*, et al.*, "Data-aided chromatic dispersion estimation for polarization multiplexed optical systems," *IEEE Photonics Journal,* vol. 4, no. 5, pp. 2037-2049, 2012.

[52] R. A. Soriano, F. N. Hauske, N. G. Gonzalez, Z. Zhang, Y. Ye, and I. T. Monroy, "Chromatic dispersion estimation in digital coherent receivers," *Journal of Lightwave Technology,* vol. 29, no. 11, pp. 1627-1637, 2011.

[53] Q. Sui, A. P. T. Lau, and C. Lu, "Fast and robust blind chromatic dispersion estimation using auto-correlation of signal power waveform for digital coherent systems," *Journal of Lightwave Technology,* vol. 31, no. 2, pp. 306-312, 2013.

[54] D. Godard, "Self-recovering equalization and carrier tracking in two-dimensional data communication systems," *IEEE Transactions on Communications,* vol. 28, no. 11, pp. 1867-1875, 1980.

[55] S. J. Savory, "Digital filters for coherent optical receivers," *Optics Express,* vol. 16, no. 2, pp. 804-817, 2008.

[56] T. Okoshi and K. Kikuchi, *Coherent Optical Fiber Communications*, Springer Science & Business Media, 1988.

[57] S. Camatel, V. Ferrero, R. Gaudino, and P. Poggiolini, "Optical phase-locked loop for coherent detection optical receiver," *Electronics Letters,* vol. 40, no. 6, p. 1, 2004.

[58] M. G. Taylor, "Phase estimation methods for optical coherent detection using digital signal processing," *Journal of Lightwave Technology,* vol. 27, no. 7, pp. 901-914, 2009.

[59] T. Kobayashi, A. Sano, H. Masuda, K. Ishihara, E. Yoshida, Y. Miyamoto*, et al.*, "160-Gb/s polarization-multiplexed 16-QAM long-haul transmission over 3,123 km using digital coherent receiver with digital PLL based frequency offset compensator," in *Proceedings Optical Fiber Communication Conference* (San Diego, California, United States, 2010) , p. OTuD1.

[60] P. Winzer, A. Gnauck, C. Doerr, M. Magarini, and L. Buhl, "Spectrally efficient long-haul optical networking using 112-Gb/s polarization-multiplexed 16-QAM," *Journal of Lightwave Technology,* vol. 28, no. 4, pp. 547-556, 2010.

[61] I. Fatadin, D. Ives, and S. J. Savory, "Compensation of frequency offset for differentially encoded 16-and 64-QAM in the presence of laser phase noise," *IEEE Photonics Technology Letters,* vol. 22, no. 3, pp. 176-178, 2010.

[62] I. Fatadin and S. Savory, "Compensation of frequency offset for 16-QAM optical coherent systems using QPSK partitioning," *IEEE Photonics Technology Letters,* vol. 23, no. 17, p. 1246, 2011.

[63] M. Taylor, "Accurate digital phase estimation process for coherent detection using a parallel digital processor," in *Proceedings European Conference on Optical Communication* (Glasgow, United Kingdom, 2005), pp. 263-264.

[64] A. Leven, N. Kaneda, U.-V. Koc, and Y.-K. Chen, "Frequency estimation in intradyne reception," *IEEE Photonics Technology Letters,* vol. 6, no. 19, pp. 366-368, 2007.

[65] D. Marcuse, "Classical derivation of the laser rate equation," *IEEE Journal of Quantum Electronics,* vol. 19, no. 8, pp. 1228-1231, 1983.

[66] R. Tucker, "High-speed modulation of semiconductor lasers," *IEEE Transactions on Electron Devices,* vol. 32, no. 12, pp. 2572-2584, 1985.

[67] M. Asada, and Y. Suematsu, "Density-matrix theory of semiconductor lasers with relaxation broadening model-gain and gain-suppression in semiconductor lasers," *IEEE Journal of Quantum Electronics*, vol. 21, no. 5, pp. 434-442, 1985.

[68] A. J. Lowery, "New dynamic semiconductor laser model based on the transmission-line modelling method," *IEEE Proceedings J-Optoelectronics*, vol. 134, no. 5, pp. 281-289, 1987.

[69] B. S. Kim, Y. Chung, and J. S. Lee, "An efficient split-step time-domain dynamic modeling of DFB/DBR laser diodes," *IEEE Journal of Quantum Electronics,* vol. 36, no. 7, pp. 787-794, 2000.

[70] M. Davis and R. O'Dowd, "A transfer matrix method based large-signal dynamic model for multielectrode DFB lasers," *IEEE Journal of Quantum Electronics,* vol. 30, no. 11, pp. 2458-2466, 1994.

[71] E. Avrutin, J. Arnold, and J. Marsh, "Analysis of dynamics of monolithic passively mode-locked laser diodes under external periodic excitation," *IEE Proceedings-Optoelectronics,* vol. 143, no. 1, pp. 81-88, 1996.

[72] C. Gardiner, R. Plumb, P. Williams, and T. Reid, "Three-section sampled-grating DBR lasers: modelling and measurements," *IEE Proceedings-Optoelectronics,* vol. 143, no. 1, pp. 24-30, 1996.

[73] A. L. Schawlow, and C. H. Townes, "Infrared and optical masers," *Physical Review*, vol. 112, no. 6, p. 1940, 1958.

[74] V. Nikolaev, I. Dmitriev, L. Fateeva, Y. A. Teplova, K. Baskova, B. Dzhelepov, Z. Komissarova, A. Karamyan, G. Dorofeev, and D. Klochkov, "Experimental investigation of electron capture by multiply charged ions," *Sov. Phys. JETP,* vol. 13, 1961.

[75] M. G. Bernard, and G. Duraffourg, "Laser conditions in semiconductors," *Physica Status Solidi (b),* vol. 1, no. 7, pp. 699-703, 1961.

[76] W. Dumke, "Interband transitions and maser action," *Physical Review,* vol. 127, no. 5, p. 1559, 1962.

[77] T. Suhara, *Semiconductor Laser Fundamentals*, CRC Press, 2004.

[78] J. C. Cartledge, and G. Burley, "The effect of laser chirping on lightwave system performance," *Journal of Lightwave Technology*, vol. 7, no. 3, pp. 568-573, 1989.

[79] M. Ahmed, M. Yamada, and M. Saito, "Numerical modeling of intensity and phase noise in semiconductor lasers," *IEEE Journal of Quantum Electronics*, vol. 37, no. 12, pp. 1600-1610, 2001.

[80] S. Javro, and S. Kang, "Transforming Tucker's linearized laser rate equations to a form that has a single solution regime," *Journal of Lightwave Technology,* vol. 13, no. 9, pp. 1899-1904, 1995.

[81] J. C. Cartledge, and R. Srinivasan, "Extraction of DFB laser rate equation parameters for system simulation purposes," *Journal of Lightwave Technology,* vol. 15, no. 5, pp. 852-860, 1997.

[82] A. Villafranca, J. Lasobras, and I. Garcés, "Precise characterization of the frequency chirp in directly modulated DFB lasers," in *Proceedings Spanish Conference on Electron Devices* (Madrid, Spanish, 2007), pp. 173-176.

[83] P. Corrc, O. Girad, and I. F. De Faria Jr, "On the thermal contribution to the FM response of DFB lasers: theory and experiment," *IEEE Journal of Quantum Electronics,* vol. 30, no. 11, pp. 2485-2490, 1994.

[84] H. Shalom, A. Zadok, M. Tur, P. J. Legg, W. Cornwell, and I. Andonovic, "On the various time constants of wavelength changes of a DFB laser under direct modulation," *IEEE Journal of Quantum Electronics,* vol. 34, no. 10, pp. 1816-1822, 1998.

[85] T. Niemi, M. Uusimaa, and H. Ludvigsen, "Limitations of phase-shift method in measuring dense group delay ripple of fiber Bragg gratings," *IEEE Photonics Technology Letters,* vol. 13, no. 12, pp. 1334-1336, 2001.

[86] M. Froggatt, E. Moore, and M. Wolfe, "Interferometric measurement of dispersion in optical components," in *Proceedings Optical Fiber Communication Conference* (Anaheim, California, United States, 2002), pp. 252-253.

[87] X. Yi, Z. Li, Y. Bao, and K. Qiu, "Characterization of passive optical components by DSP-based optical channel estimation," *IEEE Photonics Technology Letters,* vol. 24, no. 6, pp. 443-445, 2012.

[88] J. C. Cartledge and A. S. Karar, "100 Gb/s intensity modulation and direct detection," *Journal of Lightwave Technology,* vol. 32, no. 16, pp. 2809-2814, 2014.

[89] K. Szczerba, P. Westbergh, M. Karlsson, P. A. Andrekson, and A. Larsson, "70 Gbps 4-PAM and 56 Gbps 8-PAM using an 850 nm VCSEL," *Journal of Lightwave Technology,* vol. 33, no. 7, pp. 1395-1401, 2015.

[90] T. L. Koch and J. E. Bowers, "Nature of wavelength chirping in directly modulated semiconductor lasers," *Electronics Letters,* vol. 20, no. 25-2, pp. 1038-1040, 1984.

[91] Q. Hu, D. Che, Y. Wang, A. Li, J. Fang, and W. Shieh, "Beyond amplitude-only detection for digital coherent system using directly modulated laser," *Optics Letters,* vol. 40, no. 12, pp. 2762-2765, 2015.

[92] R. Bellman, *Dynamic Programming*, Princeton University Press, 1957.

[93] K. Sato, S. Kuwahara, and Y. Miyamoto, "Chirp characteristics of 40-Gb/s directly modulated distributed-feedback laser diodes," *Journal of Lightwave Technology,* vol. 23, no. 11, p. 3790, 2005.

[94] S. Matsuo, T. Kakitsuka, T. Segawa, R. Sato, Y. Shibata, R. Takahashi*, et al.*, "4 × 25 Gb/s frequency-modulated DBR laser array for 100-GbE 40-km reach application," *IEEE Photonics Technology Letters,* vol. 20, no. 17, pp. 1494-1496, 2008.

[95] M. Luo, Q. Mo, X. Li, R. Hu, Y. Qiu, C. Li*, et al.*, "Transmission of 200 Tb/s (375× 3× 178.125 Gb/s) PDM-DFTS-OFDM-32QAM super channel over 1 km FMF," *Frontiers of Optoelectronics,* vol. 8, no. 4, pp. 394-401, 2015.

[96] D. Soma, K. Igarashi, Y. Wakayama, K. Takeshima, Y. Kawaguchi, N. Yoshikane*, et al.*, "2.05 Peta-bit/s super-nyquist-WDM SDM transmission using 9.8-km 6-mode 19-core fiber in full C

band," in *Proceedings European Conference on Optical Communication* (Valencia, Spain, 2015), pp. 1-3.

[97] X. Liu and X. Wei, "Electronic dispersion compensation based on optical field reconstruction with orthogonal differential direct-detection and digital signal processing," in Proceedings *Optical Fiber Communication Conference* (Anaheim, California, United States, 2007), p. OTuA6.

[98] P. P. Mitra and J. B. Stark, "Nonlinear limits to the information capacity of optical fibre communications," *Nature,* vol. 411, no. 6841, pp. 1027-1030, 2001.

[99] A. J. Lowery, "Fiber nonlinearity pre-and post-compensation for long-haul optical links using OFDM," *Optics Express,* vol. 15, no. 20, pp. 12965-12970, 2007.

[100] D. S. Millar, S. Makovejs, C. Behrens, S. Hellerbrand, R. I. Killey, P. Bayvel*, et al.*, "Mitigation of fiber nonlinearity using a digital coherent receiver," *IEEE Journal of Selected Topics in Quantum Electronics,* vol. 16, no. 5, pp. 1217-1226, 2010.

[101] E. Ip, "Nonlinear compensation using backpropagation for polarization-multiplexed transmission," *Journal of Lightwave Technology,* vol. 28, no. 6, pp. 939-951, 2010.

[102] X. Chen, X. Liu, S. Chandrasekhar, B. Zhu, and R. Tkach, "Experimental demonstration of fiber nonlinearity mitigation using digital phase conjugation," in *Proceedings Optical Fiber Communication Conference* (Los Angeles, California, United States, 2012), p. OTh3C. 1.

[103] F. P. Guiomar, J. D. Reis, A. L. Teixeira, and A. N. Pinto, "Mitigation of intra-channel nonlinearities using a frequency-domain Volterra series equalizer," *Optics express,* vol. 20, no. 2, pp. 1360-1369, 2012.

[104] E. Giacoumidis, S. Mhatli, T. Nguyen, S. T. Le, I. Aldaya, M. E. McCarthy*, et al.*, "Comparison of DSP-based nonlinear equalizers for intra-channel nonlinearity compensation in coherent optical OFDM," *Optics letters,* vol. 41, no. 11, pp. 2509-2512, 2016.

[105] L. B. Du, M. M. Morshed, and A. J. Lowery, "Fiber nonlinearity compensation for OFDM super-channels using optical phase conjugation," *Optics Express,* vol. 20, no. 18, pp. 19921-19927, 2012.

[106] X. Liu, A. Chraplyvy, P. Winzer, R. Tkach, and S. Chandrasekhar, "Phase-conjugated twin waves for communication beyond the Kerr nonlinearity limit," *Nature Photonics,* vol. 7, no. 7, pp. 560-568, 2013.

[107] S. Wahls, "Fiber-Optic communication using fast nonlinear Fourier transforms," in *Proceedings Optical Fiber Communication Conference* (Anaheim, California, United States, 2016), p. W3A. 1.

Appendix A: Acronyms

10G-EPON	10-Gb/s Ethernet Passive Optical Network
400-GbE	400-Gb/s Ethernet
ADC	Analog-to-Digital Converter
AMP	Amplifier
AOM	Acoustic Optical Modulator
AON	Active Optical Networks
APD	Avalanche Photodiode
APON	ATM Passive Optical Networks
ASE	Amplified Spontaneous Emission
ATM	Asynchronous Transfer Mode
ATT	Attenuator
AWG	Arbitrary Waveform Generator
AWGN	Additive White Gaussian Noise
B2B	Back-to-Back
BER	Bit Error Rate
BPD	Balanced Photodetector
BPON	Broadband Passive Optical Networks
BS	Beam Splitter
CAP	Carrierless Amplitude and Phase Modulation
CATV	Community Antenna Television
CD	Chromatic Dispersion
CM	Complex Modulation
CMA	Constant Modulus Algorithm

CM-DML	Complex-Modulated Directly Modulated Laser
CMMA	Cascaded Multi-Modulus Algorithm
COHD	Coherent Detection
CP	Cyclic Prefix
CW	Continuous Wave
DAC	Digital-to-Analog Converter
DBR	Distributed Bragg Reflector
DD	Direct Detection
DD-LMS	Decision-Directed Least Mean Square
DDMZM	Dual-Drive Mach-Zehnder Modulator
DD-PLL	Decision-Directed Phase-Locked Loop
DFB	Distributed Feedback
DGD	Differential Group Delay
DML	Directed Modulated Laser
DMT	Discrete Multitone
DP	Dynamic Programming
DPSK	Differential Phase-Shift Keying
DSP	Digital Signal Processing
DWDM	Dense Wavelength-Division Multiplexing
EAM	Electro-Absorption Modulator
ECL	External Cavity Laser
EDFA	Erbium-Doped Fiber Amplifier
EML	Externally Modulated Laser
FEC	Forward Error Correction
FFT	Fast Fourier Transform
FIR	Finite-Impulse Response
FM	Frequency Modulation

FM-to-AM	Frequency Modulation to Amplitude Modulation
FN	Frequency Noise
I/Q	In-Phase and Quadrature
ICI	Inter-Channel Interference
IEEE	Institute of Electrical and Electronics Engineers
IFFT	Inverse Fast Fourier Transform
IIR	Infinite-Impulse Response
IM	Intensity Modulation
IM-DD	Intensity Modulation Direct Detection
ISI	Inter-Symbol Interference
ITU	International Telecommunication Union
LCA	Levin-Campello Algorithm
LMS	Least Mean Square
LO	Local Oscillator
MAN	Metropolitan Area Networks
MAP	Maximum a Posteriori
MAP-DP	Maximum a Posteriori Dynamic Programming
MIMO	Multiple Input Multiple Output
MLSE	Maximum Likelihood Sequence Estimation
MMA	Multi-Modulus Algorithm
MQW-DFB	Multiple Quantum Well Distributed Feedback
MZI	Mach-Zehnder Interferometer
MZM	Mach-Zehnder Modulator
NEP	Noise Equivalent Power
NFT	Nonlinear Fourier Transform

NG-PON2	Next-Generation Passive Optical Networks 2
NLSE	Nonlinear Schrödinger Equation
NRZ	Non-Return to Zero
OEO	Optical Electrical Optical
OBPF	Optical Bandpass Filter
ODE	Ordinary Differential Equation
OFDM	Orthogonal Frequency-Division Multiplexing
OLT	Optical Line Terminal
ONU	Optical Network Unit
OOK	On-Off Keying
OSNR	Optical Signal-to-Noise Ratio
PAM	Pulse Amplitude Modulation
PBC	Polarization Beam Combiner
PBS	Polarization Beam Splitter
PC	Polarization Controller
PD	Photodetector
PDL	Polarization Dependent Loss
PDM	Polarization-Division Multiplexing
PE-DP	Parameter Estimation Based Dynamic Programming
PI	Proportional Integral
PLL	Phase-Locked Loop
PMD	Polarization Mode Dispersion
PMF	Polarization Maintaining Fiber
PON	Passive Optical Networks
PRBS	Pseudorandom Binary Sequence
PSK	Phase-Shift Keying
PSP	Principle State of Polarization

QAM	Quadrature Amplitude Modulation
QPSK	Quadrature Phase-Shift Keying
RF	Radio Frequency
RIN	Relative Intensity Noise
ROSA	Receiver Optical Sub-Assembly
SDM	Space-Division Multiplexing
SiP	Silicon Photonics
SNR	Signal-to-Noise Ratio
SOA	Semiconductor Optical Amplifier
SPM	Self-Phase Modulation
SSMF	Standard Single-Mode Fibre
TCC-VCSEL	Transverse-Coupled-Cavity Vertical-Cavity Surface-Emitting Laser
TDM-PON	Time-Division Multiplexing Passive Optical Networks
TEC	Thermoelectric Cooler
TIA	Transimpedance Amplifier
VCO	Voltage-Controlled Oscillator
VCSEL	Vertical-Cavity Surface-Emitting Laser
WDM	Wavelength-Division Multiplexing
XPM	Cross-Phase Modulation